INVESTIGATION OF INSTABILITIES AFFECTING DETONATIONS: IMPROVING THE RESOLUTION USING BLOCK-STRUCTURED ADAPTIVE MESH REFINEMENT

by

PRASHAANTH RAVINDRAN

Presented to the Faculty of the Graduate School of
The University of Texas at Arlington in Partial Fulfillment
of the Requirements
for the Degree of

DOCTOR OF PHILOSOPHY

THE UNIVERSITY OF TEXAS AT ARLINGTON

May 2012

To my wife Harini and my parents, for without them I'm nothing.

But the real glory of science is that we can find a way of thinking such that the law is evident. - Richard P. Feynman

ACKNOWLEDGEMENTS

I would like to sincerely thank Dr. Luca Massa for being an excellent mentor and guided me day and night through the dense field of detonation modeling. I could not have accomplished even half of this work without his encouragement, advise and support. I consider myself very fortunate to be his first doctoral student and I wish him many more doctoral students.

I would like to acknowledge the dissertation committee members Dr. Frank Lu, Dr. Wilson, Dr. Subbarao and Dr. Agonafer for their assistance and guidance. Specifically, I am deeply grateful to Dr. Subbarao and Dr. Wilson for their patience and tolerance towards my arduous path to completing this doctoral degree.

I am grateful to many former and current students at the Aerodynamics Research Center, specifically Albert Ortiz, Richard Mitchell, Adam Pierce and Eric Braun, for the good times and making this path to the degree very interesting. On a sad note, I miss my good friend and mentor, Rodney Duke, whose untimely passing has left a void. I owe a lot to Rod for his perspective and his dicta on personal safety and awareness in the workplace.

Lastly, and the most important of the people here, I thank my best friend and wife Harini Gopal for believing and standing strong by me. Without her, I would've faltered and withered. I am in deep gratitude to my mom and dad, for their love and support were enough on most days.

May 7, 2012

ABSTRACT

INVESTIGATION OF INSTABILITIES AFFECTING DETONATIONS: IMPROVING THE RESOLUTION USING BLOCK-STRUCTURED ADAPTIVE MESH REFINEMENT

PRASHAANTH RAVINDRAN, Ph.D.

The University of Texas at Arlington, 2012

Supervising Professor: Luca Massa

The unstable nature of detonation waves is a result of the critical relationship between the hydrodynamic shock and the chemical reactions sustaining the shock. A perturbative analysis of the critical point is quite challenging due to the multiple spatio–temporal scales involved along with the non–linear nature of the shock–reaction mechanism. The author's research attempts to provide detailed resolution of the instabilities at the shock front. Another key aspect of the present research is to develop an understanding of the causality between the non–linear dynamics of the front and the eventual breakdown of the sub–structures. An accurate numerical simulation of detonation waves requires a very efficient solution of the Euler equations in conservation form with detailed, non–equilibrium chemistry. The difference in the flow and reaction length scales results in very stiff source terms, requiring the problem to be solved with adaptive mesh refinement. For this purpose, Berger–Colella's block–structured adaptive mesh refinement (AMR) strategy has been developed and applied to time–explicit finite volume methods. The block–structured technique uses a hierar-

chy of parent–child sub–grids, integrated recursively over time. One novel approach to partition the problem within a large supercomputer was the use of modified Peano–Hilbert space filling curves. The AMR framework was merged with CLAWPACK, a package providing finite volume numerical methods tailored for wave–propagation problems. The stiffness problem is bypassed by using a 1^{st} order Godunov or a 2^{nd} order Strang splitting technique, where the flow variables and source terms are integrated independently. A linearly explicit fourth-order Runge-Kutta integrator is used for the flow, and an ODE solver was used to overcome the numerical stiffness. Second–order spatial resolution is obtained by using a second–order Roe–HLL scheme with the inclusion of numerical viscosity to stabilize the solution near the discontinuity. The scheme is made monotonic by coupling the van Albada limiter with the higher order MUSCL–Hancock extrapolation to the primitive variables of the Euler equations. Simulations using simplified single–step and detailed chemical kinetics have been provided. In detonations with simplified chemistry, the one–dimensional longitudinal instabilities have been simulated, and a mechanism forcing the collapse of the period–doubling modes was identified. The transverse instabilities were simulated for a 2D detonation, and the corresponding transverse wave was shown to be unstable with a periodic normal mode. Also, a Floquet analysis was carried out with the three–dimensional inviscid Euler equations for a longitudinally stable case. Using domain decomposition to identify the global eigenfunctions corresponding to the two least stable eigenvalues, it was found that the bifurcation of limit cycles in three dimensions follows a period doubling process similar to that proven to occur in one dimension and it is because of transverse instabilities. For detonations with detailed chemistry, the one dimensional simulations for two cases were presented and validated with experimental results. The 2D simulation shows the re–initiation of

the triple point leading to the formation of cellular structure of the detonation wave. Some of the important features in the front were identified and explained.

TABLE OF CONTENTS

LIST OF ILLUSTRATIONS

LIST OF TABLES

CHAPTER 1

INTRODUCTION

This research work is a numerical study of the detonation front, geared towards understanding the spatio–temporal instability of the front resulting in periodic oscillation of the shock front and the associated fluctuations in the reaction zone. The interaction between the hydrodynamic flow and the chemical kinetics is complex in nature and there have been concerted efforts in trying to explain the phenomena. Planar wave theory, used in the turn of the 20^{th} century to explain detonations, while accurately determining detonation velocity, has been insufficient to explain even the modest detonation experiments. Experiments and numerical simulations over the last few decades have shown that detonation waves exhibit non–stationary, multi–dimensional structures and the shock front has a symbiotic relationship with the reaction zone. Even with all the modern advances in imaging and spectral methods to capture detonations, significant difficulties arise when analyzing the reaction zone. Numerical simulations have provided a valuable insight and more detail of the flow–field. However, detailed resolution of the reaction zone has been a problematic topic in the past due to the limitations of grid density affecting computational expenditure. The reaction zone plays a vital role in the development of instabilities and therefore needs to be addressed in proper context.

1.1 Detonation Wave Structure

A detonation is characterized by a shock wave coupled to a region of intense chemical reactions. The shock, acting like a piston in an engine, adiabatically com-

presses the combustible mixture, raising the temperature above the point of ignition. At the occurrence of ignition, there is a delay known as "induction time" for the reactants to react rapidly to attain chemical equilibrium. Since the chemical reaction is exothermic, the energy release aids in propagation of the wave. The shock and the reaction zone travel at identical wave speed, known the Chapman–Jouguet (CJ) velocity. The CJ velocity is the limiting velocity of a self sustaining detonation which was independently calculated by Chapman [4] and Jouguet [5]. At this point, the shock–reaction front would be in perfect equilibrium. However, this equilibrium is very sensitive to transverse and longitudinal disturbances (unstable modes) which can destroy the planar structure. These modes can lead to non–stationary shock waves propagating to the detonation front, involving spatio–temporal periodic oscillations of the shock–reaction front. This sets up a complex flow pattern known as a "triple point", where the detonation front is intersected by a transverse shock. Due to the curving of the lead shock, a system of vortices are created which travel into reaction zone, thus disturbing the chemical reaction rates, leading to further imbalance in shock structure. It becomes necessary to understand the nature of triple point formation and the instabilities associated with the formations, for various safety studies such as hydrogen fuel cells and technical applications such as detonation engines.

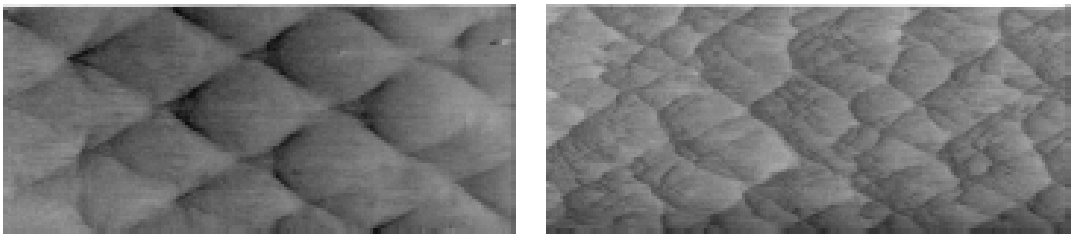

Figure 1.1. Shadowgraph images showing the difference of regular cell structure due to weakly unstable detonation waves (diluted with Argon) to that of the irregular cell structures due to strongly unstable detonation waves [1].

Experiments with diluent hydrogen–oxygen have exhibited an organized or "regular" structure when compared to undiluted mixtures which show a vastly "irregular" structure, on soot foils [1]. Detonations with regular and irregular structures have significantly different macroscopic behaviors with differing activation energies and critical diameters. Since regular structures are observed only in highly diluted mixtures, which are impractical in technical applications and unrealistic in practical safety problems like explosion hazards, it becomes necessary to study the behavior of detonations close to the limits of instability and beyond.

The instability of the front and the appearance of transverse waves for a weakly unstable detonation is shown in Figure 1.2. The shock–front undergoes cyclic spatio–temporal oscillations during the wave propagation. One can also visualize some wave–like structures moving perpendicular to the overall direction of the detonation wave and periodically collide with the lead shock setting up regions of intense temperature and pressure. These waves are known as "transverse waves" and their presence is vital for detonation propagation. After a collision, the shock decays smoothly till the next transverse wave collision. The point of collision of the transverse and longitudinal wave is called a "triple point". Hence, the wavefront has a coupled transverse-longitudinal instability, involving periodic cycles of oscillations and one such complete cycle is known as a "cell cycle". The cellular pattern is the history of triple point tracks in the propagating front and the width of the cells is the measure of spacing of the transverse waves, commonly referred to as the detonation cell width λ.

1.2 Historical Perspective

The instability of the detonation wave front and resulting cellular structure has been documented extensively, and some of the most important studies are discussed here. The earliest theory on detonations was provided by Zeldovich [6]. Strehlow

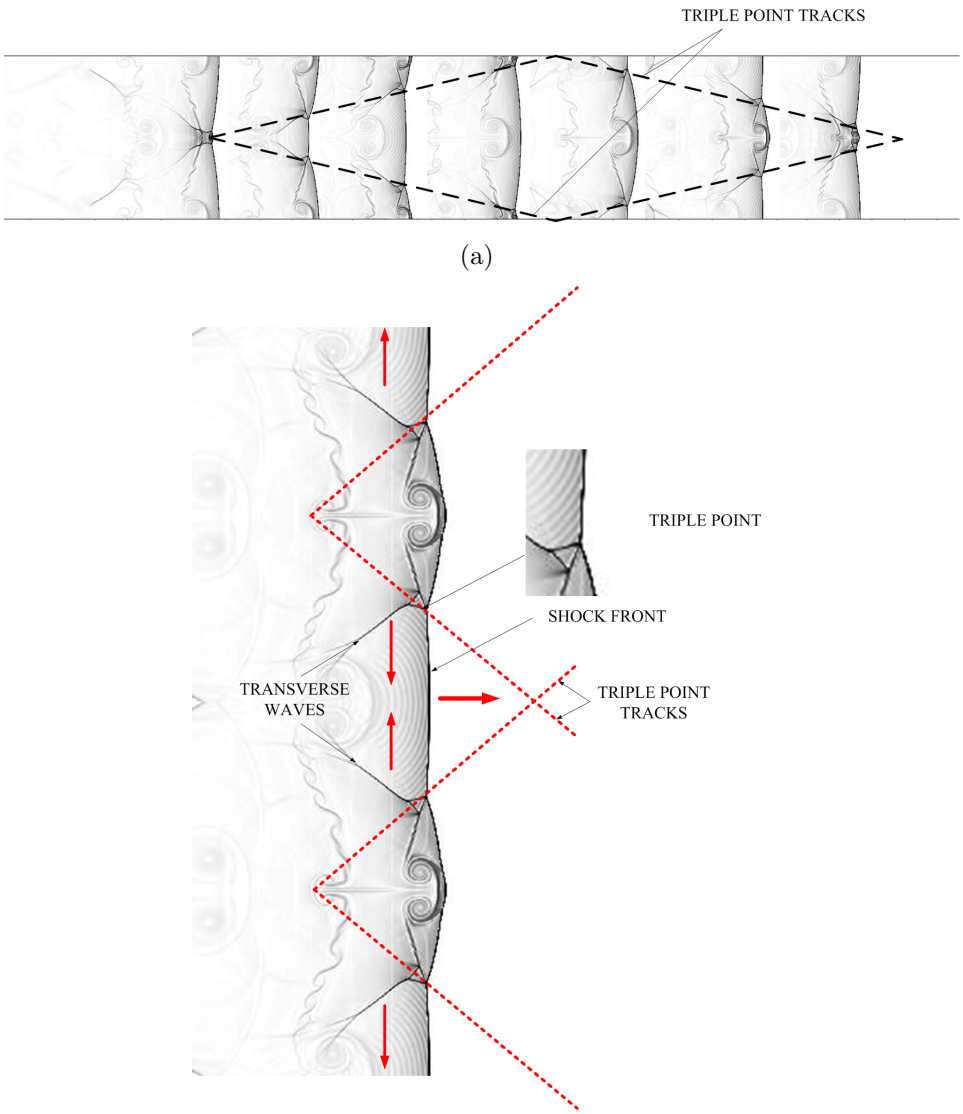

Figure 1.2. Top:2D simulation of a weakly unstable detonation wave illustrating a complete cell cycle. Bottom: Triple point tracks shown as dashed lines form the cellular pattern when the wave propagates.

investigated in detail the transverse wave structure in weakly–unstable detonations supported by dilute hydrogen–oxygen and acetylene–oxygen mixtures; he qualitatively measured the wave spacing over a large range of pressures and temperatures [7]. These studies showed that the dominant factors in determining detonation cell–

size were the reaction zone length, initial pressure, diluent fraction and stoichiometry. Erpenbeck investigated the linear stability of steady detonation waves and obtained numerical results for the stability boundary limits for a single-step Arrhenius reaction rate model [8]. Barthel developed an alternate approximate analysis that demonstrated the trapping of acoustic waves in the reaction zone, and showed that the wavefront was convoluted [9]. Also, the spacing factor was computed to be roughly twice the observed transverse spacing of dilute hydrogen–oxygen detonations. However, the early theoretical approaches ignored the coupling between the transverse waves, the main shock and the reaction zone. Shepherd concentrated on improving the chemical kinetics part of the problem but ignored the multidimensional nature of the observed cellular structure [10]. A more detailed chemical kinetics approach was taken by Bauwens et al., who modeled detonations with a pressure dependent four–step chain–branching reaction model [11].

The distance between the leading shock front and measurable reaction is known as the "induction length L_{ig}". This induction zone behind the shock plays a vital role in the stability of the front and it was attempted to solve this as a linear stability eigenvalue problem [12]. The detonation was unstable under all conditions when the induction zone was very sensitive to the shock temperature. The nonlinear development of instability was studied in detail using numerical and asymptotic methods by Bourlioux et al. [13]. It was discovered that the transition to instability involved an eigenmode crossing the imaginary axis, indicating the presence of a Hopf bifurcation. This investigation also documented for the first time a multi–dimensional numerical computation in the regime of transition to instability [14]. Short conducted a normal mode analysis to study the linear stability of one– and two– dimensional detonation wave characterized by a single–step Arrhenius chemical reaction [15]. He made the following observations: for one–dimensional disturbances, a low–frequency oscillatory

mode bifurcates into a slowly evolving non–oscillatory mode for lower activation energies and a faster one for higher activation energies. Also, for large activation energies, the stability spectrum consists of a large number on unstable one–dimensional modes possessing a maximum growth rate at very high frequencies. Numerical simulations in two– and three– dimensions showed that the increase in activation energy resulted in more irregular structures characterized by stronger triple points, large variations of local shock velocity inside the detonation cell and higher frequency in the creation and destruction of triple points, independent of boundary conditions [16, 17, 18]. Massa et al. shed more light on the triple point shear layers observed for higher activation energies and showed that an enhanced mixing between the reacted and unreacted systems was supported by a Kelvin–Helmholtz instability [19]. One important observation by their study was that large scale vortical structures occurring downstream of the induction distance did not affect the reaction for low activation energy mixtures but is not so conclusive for high activation energies.

Majda had proved the existence and stability of multi–dimensional detonations using the assumption of uniform stability [20], a principle which was applied successfully to detonations by Zumbrun et al [21]. Their work provided a stability index which is satisfied for weak and strong detonations of Majda model. Zumbrun also conducted a rigorous characterization of the transition from stability to time–periodic "galloping" instability for traveling waves. He concluded that a relative Poincaré–Hopf bifurcation arises in ODE with translational symmetry [22]. This was extended to detonations, bifurcation conditions were determined and the first complete nonlinear stability result for strong detonations was provided for one–dimensional detonations [23]. Using this technique, a bifurcation diagram illustrating the transition pattern from a simple harmonic limit–cycle to a more complex oscillation, can be constructed from the computational results [24]. The period doubling events predicted earlier

were confirmed using shock fitting coupled with higher order WENO for single step chemical kinetics [25]. However, due to the computational expense of uniform meshes, multi–dimensional simulations have not been carried out. Hence, the effort was undertaken to visualize the period–doubling events leading to chaos in multi–dimensional simulations so that a complete picture can be developed to the underlying causes of these instabilities.

1.3 Motivation And Approach

At high effective activation energies, a detonation supports a large set of instability modes characterized by highly dispersive waves with a broad range of phase velocities. Consider, for example, the dispersion diagram for a $Q = E = 50$ (Q and E are the heat release and energy parameters) structure shown in Fig. 1.3. The diagram shows that the detonation does not have a preferential instability mode, but a broad band spectrum of modes with similar peak growth rates (i.e., $Re(\alpha)$ in Fig. 1.3). As a result, a high activation energy detonation sustains multi–scale and dispersive phenomena that produce a broad range of sub–structures very difficult to capture with computational fluid dynamic methods operating on static computational meshes. Adaptive mesh refinement (AMR) can play a vital role in the quest to understand and resolve the sub–structures in a detonation wave. Higher resolutions than those generally used in numerical studies are required. Resolutions of less than 20 points in the characteristic induction length (L_{ig}) of the detonation gives very poor predictions of the shock configuration and chemical reaction [26]. The use of AMR can drastically reduce computation time while maintaining the accuracy. With the help of AMR, it is possible to investigate the evolution of the longitudinal instability and explore the non–linear features far from the stability limit. Since the path of the

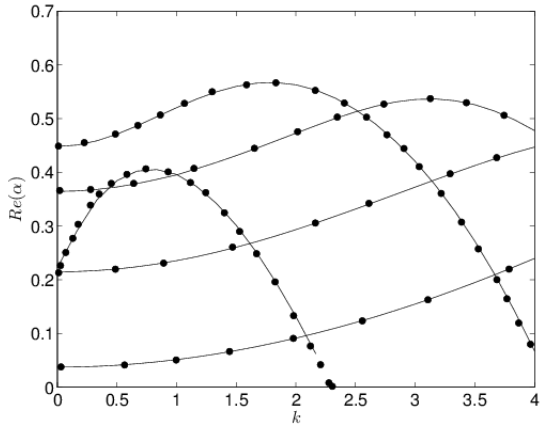

Figure 1.3. Detonation dispersion diagram at high activation energy. Legend: Solid line (present research), symbols [2]. Growth rate versus frequency for $\gamma = 1.2$ (constant), $Q = E = 50$, and $f = 1.2$. Normal modes for $k \leq 4$ are plotted.

instability pattern to chaos is uncertain, general interpretation of a large amount of data by conducting numerical simulations is highly preferable to experimental studies.

Accurate modeling of the (turbulent) fluctuations supported by detonations is of interest to a number of engineering applications, which include, for example, the computational analysis of detonation engines. A successful modeling effort must consider the nature of the breakdown of the sub–structures supported by the thermo-acoustic instability, and how this process is related to the detonation parameters. Based on observations and extensive research on the topic, detonations have now been classified into two categories: weakly unstable detonations in mixtures with low activation energy and heat release, and highly unstable detonations in mixtures with high activation energy and heat release. In weakly unstable detonation, "keystone" structures were observed experimentally [27, 1] and it was discovered that shear layers form the boundary of keystones, separating fast–reacting gas passing through the Mach stem portion of the front and the slow–reacting gas passing through transverse waves. Because of the existence of shear layers, the transverse waves were found to

be insignificant in affecting combustion, hence do not play a role in the propagation of weakly stable fronts. For the strong unstable detonations however, substantial oscillations have been observed in the reaction zone behind the shock, resulting in Kelvin–Helmholtz instabilities resembling a turbulent combustion mechanism. It becomes necessary to understand the role of the small–scale structures which can affect the propagation of highly unstable detonations.

1.4 Dissertation Outline

A solution framework for the reactive Euler equations in mixtures of thermally perfect gases with both single step and detailed chemical reaction kinetics, using spatio–temporal adaptive mesh refinement is outlined in this thesis. In Chapter 2, a brief theory behind detonation waves is provided. A stationary one–dimensional Zeldovich-Neumann-Döring model is solved with Euler equations [6, 28]. The exact solution of the simplest model with a single step irreversible chemical kinetics was derived and then extended to detailed reaction mechanism [29]. In Chapter 3, the mathematical and numerical modeling of detonations are outlined. The governing equations are the Euler equations with reaction terms written in a conservation law form. The numerical methods employed to solve the governing equations are also discussed. The application of a suitable shock–capturing method on the Euler equations is a very important topic and is discussed in detail in this chapter. The technique employed was a hybrid second–order Roe-Harten-Lax-Van Leer with Einfeldt modification and entropy correction [30]. The entropy correction was used to add artificial viscosity to moderate the nonphysical oscillations appearing at jump conditions [31]. To ensure higher order accuracy, the MUSCL variable extrapolation was used.

In Chapter 4, the Berger–Collela block–structured AMR is derived and explained in detail [32]. The parallel implementation is discussed with a strategy to

reduce communication overhead. The load balancing is performed using a novel Peano–Hilbert space filling curve [33]. Some benchmark test cases are also provided to illustrate the efficiency of the algorithm. In Chapter 5, the simulations are carried out with simplified single–step chemistry. The period–doubling phenomena is replicated in 1–D and the additional simulations are also carried out to fill the gaps in the path to chaos. An unprecedented $320 Pts/L_{ig}$ have been used for 1–D simulations. Some of the previously unobserved features are discovered and The 2–D simulations are also provided in the bifurcation regime with $160 Pts/L_{ig}$. The 2D simulations are performed with longitudinally unstable overdrive parameters and activation energies. Also, a longitudinally stable case to illustrate the transversely unstable phenomenon was simulated. A 3D Floquet analysis was also performed on time–periodic flow. In Chapter 6, simulations with detailed chemistry for hydrogen–oxygen mixtures are provided. Like before, 1–D and 2–D simulations are carried out. The cellular structure was observed by tracking the triple points as the detonation wave propagates. Chapter 7 concludes the document with the summary of research with observations and the original contribution, and chapter 8 outlines some recommendations for future work.

CHAPTER 2

THEORY OF DETONATIONS

This chapter gives a review of detonation theory and the mathematical model pertinent to this research. Scientific studies of the detonation phenomena date back from the end of the 19^{th} century and a huge trove of literature has developed over this period. In lieu of a detailed reference list, books by Grushcka and Wecken [34], Fickett and Davis [29], Dremin [35] and a comprehensive review by Lee [36] provide a more exhaustive treatment on the topic of detonations.

An explosive gas or gaseous mixture is one which is characterized by a rapid energy release due to high exothermicity. Detonations and deflagrations are essentially combustion waves propagated by the release of energy of an explosive mixture. Not all fuel and oxidizer mixtures support a burning zone or a combustion wave, only those mixtures that are within well defined flammability limits. Detonation waves are a class of combustion waves where a shock wave is sustained by the energy of the chemical reaction in the highly compressed explosive media existing in the wave. The difference between detonations and deflagrations is their wave speed: detonations are supersonic waves and deflagrations are subsonic waves, both sustained by chemical reactions. Also, not all explosions are detonations: explosions differ by not requiring this coupling of chemical reaction with the shock front.

Studies of gaseous detonations have shown no single sequence of events due to what is now referred to the complex cellular structure of a detonation wave. After successful initiation of a detonation wave, transverse waves have been experimentally observed to impact the walls of the test–section, displaying a distinct "fish scale"

pattern [37]. Studies on transverse waves have been limited due to the difficulty in accurately quantifying them, but are nonetheless important because the regularity of the cellular structures depends on the transverse waves.

The far-field solution of steady detonations waves does not require any knowledge of the structure of the induction region, but can be determined based on conservation laws (control volume approach). Section 2.1 details the concepts proposed by Chapman [4] and Jouguet [5] to determine the detonation velocity and developed the solution from the integrated conservation equations by assuming the wave to be steady, planar and one–dimensional. The CJ theory also establishes the flow behind the shockfront to be sonic. The classical one–dimensional theory of detonation known as the Zeldovich–Neumann–Döring (ZND) theory extends the CJ theory. According to ZND theory, a detonation wave is constructed as a planar shock followed by a reaction zone initiated with an induction delay as discussed in Sec. 2.2. A case of a single irreversible reaction with two perfect gases using dynamic parameters s uch as activation energy, heat release and overdrive is described in Sec. 2.3. This solution is then extended to a detailed kinetics model consisting of more than two reversible reactions in Sec. 2.4. In Sec. 2.5, the oscillatory behavior of unsteady detonation waves is presented, which leads to the phenomenon of initiation of waves transverse to the mean propagation direction.

2.1 Chapman–Jouguet Simple Theory

The Chapman–Jouguet (CJ) theory posits that a detonation wave is steady, planar and one–dimensional. The approach to calculating the detonation velocity for such assumptions necessitates the understanding of the symbols used for velocities

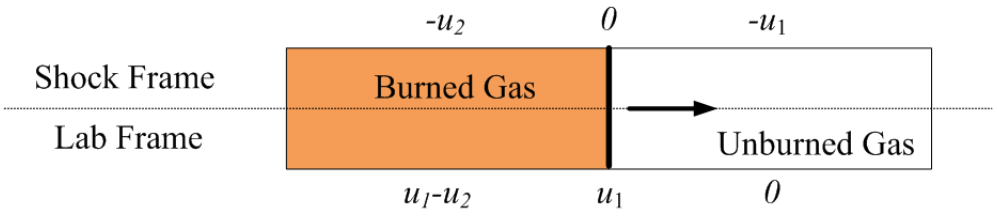

Figure 2.1. Illustration of detonation velocities in shock and lab frame.

in their appropriate reference frames, as illustrated in Figure 2.1. The integrated governing equations and the equations of state written in control volume form are:

$$\begin{aligned} &\rho_1 u_1 = \rho_2 u_2 \\ &P_1 + \rho_1 u_1^2 = P_2 + \rho_2 u_2^2 \\ &h_1 + \frac{1}{2}u_1^2 = h_2 + \frac{1}{2}u_2^2 \\ &h_1 = \tfrac{\gamma}{\gamma-1}\tfrac{P_1}{\rho_1} \quad ; \quad h_2 = \tfrac{\gamma}{\gamma-1}\tfrac{P_2}{\rho_2} \end{aligned} \tag{2.1}$$

In this type of representation, all the combustion events are collapsed into one discontinuity. There are five equations and six unknowns (u_1, u_2, h_1, h_2, P_2, ρ_2), and an eigenvalue cannot be be obtained. To determine all the unknowns, it is necessary to know the rate of reaction (the internal structure of the flow) to calculate the detonation velocity.

2.1.1 Hugoniot Line and the CJ point

It is best to develop certain relationships for convenience sake. First the expression for velocities:

$$u_2 = \left(\frac{\rho_1}{\rho_2}\right) u_1 \tag{2.2}$$

Substituting Eq. 2.2 in the momentum equation and dividing by ρ_1^2, the equation for *Rayleigh line* is obtained, shown as

$$u_1^2 = \frac{1}{\rho_1^2}\left(\frac{P_2 - P_1}{\left(\frac{1}{\rho_1} - \frac{1}{\rho_2}\right)}\right) \tag{2.3}$$

Note that the equation of state is not invoked in the derivation of the Rayleigh line. This is due to the fact that $(\rho_1 u_1)^2$ is always positive. Equation 2.3 can also be extended to velocity u_2 using Eq. 2.2.

The energy equation is rewritten using the above velocity derivations as follows:

$$h_2 - h_1 = \frac{1}{2}\left(u_1^2 - u_2^2\right) = \left(\frac{1}{\rho_1} + \frac{1}{\rho_2}\right)(P_2 - P_1) \tag{2.4}$$

Equation 2.4 is known as the *Hugoniot Curve* and can also be written in terms of the ratio of specific heats γ as

$$\frac{\gamma}{\gamma - 1}\left(\frac{P_2}{\rho_2} - \frac{P_1}{\rho_1}\right) - \frac{1}{2}\left(\frac{1}{\rho_1} + \frac{1}{\rho_2}\right)(P_2 - P_1) = h_2 - h_1 = q \tag{2.5}$$

where q is the rate of heat release from the exothermic reaction. When $q = 0$, the Hugoniot equation holds valid for a shock wave.

Figure 2.2 shows the plot of the Hugoniot curve for an arbitrary q. The curve is essentially a plot of all the possible values of $(1/\rho_2, P_2)$ for a given $(1/\rho_1, P_1)$, shown as A in the figure and a given q. The regions of possible solutions are constructed by drawing the tangents passing through A. Since the curve is a hyperbola, there are two tangents intersecting the curve, diving the Hugoniot curve into five regions, specified as Roman numerals $(I - V)$. Region V does not represent real solutions due to negative angle of the slope through those points and can be ignored. Regions III and IV give solutions for deflagration waves based on the angle of the slope and the

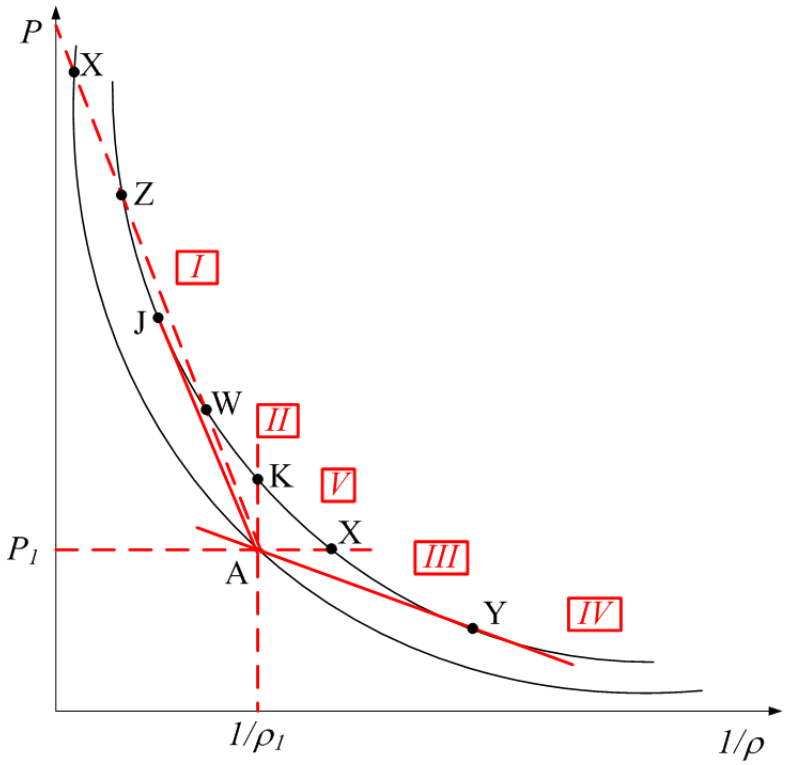

Figure 2.2. Hugoniot curve illustrating the detonation and deflagration regions.

resulting velocities. Regions I and II result in solutions for detonation waves and high velocities. This can be determined by

$$\frac{\Delta u}{u_1} = \frac{u_2 - u_1}{u_1} = \frac{(1/\rho_1) - (1/\rho_2)}{(1/\rho_1)} = 1 - \frac{(1/\rho_2)}{(1/\rho_1)} \tag{2.6}$$

In regions I and II, the detonation branch of the Hugoniot curve, $(1/\rho_2) < (1/\rho_1)$ and the right hand side of Eq. 2.6 is positive. Physically, this occurs because of the hot products following the shock wave. Regions III and IV are known as the deflagration branch, $(1/\rho_2) > (1/\rho_1)$, where the RHS of Eq. 2.6 is negative, implying that the hot gases move away from the wave.

Of particular interest on the Hugoniot curve is point J, also known as the CJ point. Chapman [4] postulated that the slope of the adiabat is exactly the slope through J,

$$\left[\frac{(P_2 - P_1)}{\left(\frac{1}{\rho_1}\right) - \left(\frac{1}{\rho_2}\right)}\right]_J = -\left\{\left[\frac{\partial P_2}{\partial\left(\frac{1}{\rho_2}\right)}\right]_s\right\}_J \tag{2.7}$$

For a detailed proof of Eq. 2.7, the reader can refer to Chapman's seminal work on detonations. Chapman's equation is very useful in developing another important condition at point J, the velocity of sound in the burned gas., which is written as:

$$c_2^2 = -\frac{1}{\rho_2^2}\left\{\frac{\partial P_2}{\partial\left(\frac{1}{\rho_2}\right)}\right\}_s \tag{2.8}$$

Using Eq. 2.8 in 2.7, it can be derived as:

$$\begin{aligned} \left[c_2^2\right]_J &= \frac{1}{\rho_2^2}\left\{\frac{(P_2 - P_1)}{\left(\frac{1}{\rho_1}\right) - \left(\frac{1}{\rho_2}\right)}\right\}_s = \left[u_2^2\right]_J \\ \left[u_2\right]_J &= \left[c_2\right]_J \Rightarrow \left[M_2\right]_J = 1 \end{aligned} \tag{2.9}$$

leading to Chapman's most important conclusion, that the velocity of burned gases gases at point J is the same as the speed of sound in the burned gases. Recalling that the velocity of burned gas is given by $\Delta u = u_1 - u_2$, at point J it is now

$$\begin{aligned} u_1 &= \Delta u + c_2 \\ u_1 &= \left(\frac{1}{\rho_1}\right)\sqrt{\left\{-\left[\frac{\partial P_2}{\partial\left(1/\rho_2\right)}\right]\right\}} \end{aligned} \tag{2.10}$$

This implies that at the point J, the detonation velocity is equal to the speed of sound in the gases behind the detonation plus the velocity of the gases at the same location. With the condition $u_2 = c_2$ at J, the detonation branches of the Hugoniot curve are now described in the following manner:

- Region I: $P_2 > P_J$, Strong detonation

- Region II: $P_2 < P_J$, Weak detonation

At points above J, the pressures and temperatures are greater than the pressure and temperature at the CJ point, $u_2 < u_{2,J}$ and $c_2 > c_{2,J}$. Thus, $M_2 < 1$ at points above J. This is an important observation since it was found that the simulations fail if M reaches the sonic velocity. The same approach can be extended to the weak detonations branch, where $M_2 > M_{2,J}$ resulting in supersonic flow behind the detonation wave.

Chapman stated in Region I, only velocities corresponding to point J are valid [4]. Jouguet further explained that, for points above point J, the speed of sound in the burned gases is greater than the detonation velocity [5]. For non-driven conditions, if a rarefaction wave starts behind a detonation wave, it should catch up to the detonation wave, dropping the pressure and reducing the velocities to those at point J. Thus points above J are unstable. At point J, since $M_2 = 1$, the rarefactions will not overtake it, making point J the condition for "self sustained" detonation. For their contributions in this topic, point J became known as the Chapman–Jouguet (CJ) point. The major problem with extending the CJ analysis to realistic gas mixtures is the assumptions of a structureless steady detonation.

Therefore, the limitations of the CJ theory are in its simplified assumptions. In Region II, the weak detonation branch may be attained by a) without shock transition by means of supersonic combustion or, b) in the so-called *pathological case*, where the region of intermediate states reaches beyond the Hugoniot curve. The second possibility merits a discussion as it leads to the extension of the CJ simple theory, discussed subsequently in this chapter. John von Neumann raised some objections over the CJ theory, in what is know called *von Neumann pathological case*, where he proved that it was possible to attain equilibrium with $M_2 > 1$ [38]. Moreover, due to the unsteady nature of detonations, it has been demonstrated experimentally and

numerically longitudinal and transversal instabilities play a crucial role. Longitudinal oscillations have in fact proven to establish a discrepancy between CJ detonation velocity and experimental observations, though at the time the deviation was not explained [7]. It has now been confirmed that only the CJ point is stable and the rest of the points on Regions I and II are unstable and will violate the CJ theory [34].

2.2 Zeldovich–Neumann–Döring Theory

Zeldovich [6], von Neumann [28] and Döring [39] independently derived the theory for the structure of the detonation wave. The ZND theory states that the detonation wave consists of a planar shock moving at the detonation velocity with a high temperature–pressure gas behind the shock. After a small amount of time period, known as "induction period", the chemical reaction is initiated and thermal energy is generated. With the progress in reaction, there is a rise in temperature and a fall in density and pressure, until CJ values are reached at which point the reaction attains equilibrium. A rarefaction wave then develops, the slope of which depends on the distance to the detonation wave. The CJ theory did not require the knowledge of the chemical rate kinetics and structure, and that assumption was satisfactory due to zero restrictions being placed on the distance between the shock and the reaction zone. But to understand the structure of the wave, the chemical kinetics must be accounted for because the reaction mechanism gives the spatial and temporal separation of the front and the C-J plane. The reaction rate for typical hydrocarbon oxidation reactions proceed at an extremely high rate following the Arrhenius law and has a relatively large overall activation energy.

Figure 2.3 shows a graphical representation of the ZND theory, by illustrating the variation of important physical parameters as a function of the propagating distance. Plane X is the shock front, plane X' is the plane immediately after the shock

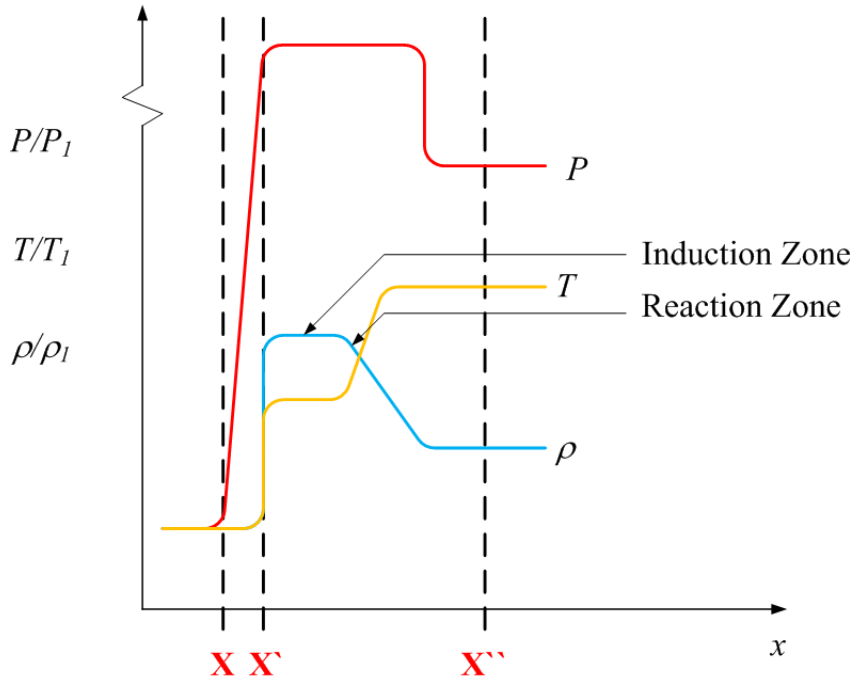

Figure 2.3. Parametric variation of physical quantities per ZND theory.

and plane X'' is the CJ plane. The conditions identifying the CJ plane have been derived in the previous section, while plane X‘ can be typified using the Rankine-Hugoniot jump conditions.

Table 2.1. Calculated values of physical parameters for hydrogen–oxygen detonations

Parameter	X	X'	X''
M	5.29	0.40	1.00
u(m/s)	2920	524	1589
P (atm)	1	33	19
T (K)	298	1773	3680
ρ/ρ_1	1.00	5.57	1.84

Table 2.1 shows typical physical values for hydrogen oxygen detonations. It can be inferred that as the gas passes from the shock front to the CJ state, the pressure

drops by approximately a factor of 2, the temperature rises by approximately a factor of 2, and the density by a factor of 3. The Hugoniot curve can be modified slightly to reflect this change and is shown in Figure 2.4.

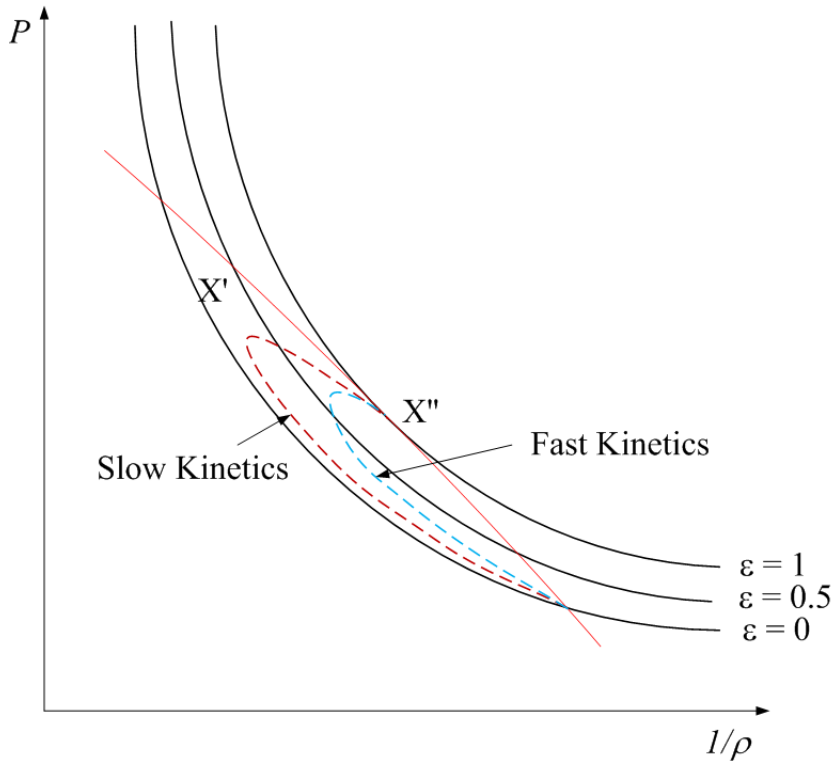

Figure 2.4. Chemical kinetics paths in the Hugoniot curve for ZND theory.

There are two possible paths, using slow kinetics or fast kinetics, by which a mass element passing through the wave from $\varepsilon = 0$ to $\varepsilon = 1$ satisfying the conservation equations and at the same time change the physical properties continuously along the distance of travel. The element may enter the wave in the state corresponding to its initial point and move directly to the CJ point, using slow kinetics, which requires reaction to occur at each point in this path. However, the pressure change across this path is very low at each point, hence the temperature cannot be raised high enough at

each discrete point to initiate fast reaction. However, on the path of faster kinetics, a jump is made from X' to X'', the conditions for reaction are met. It is noted that to jump from X' to X'', the pressure does not follow the points on the Hugoniot curve.

The ZND theory considers the structure of the wave to be one–dimensional and are adequate for determining the physical quantities of γ, P_2, T_2 and ρ_2. But as remarked in the last section, the multi–dimensional nature of detonation waves leads to the invalidation of the basic assumptions of the ZND. Finite rate chemistry is necessary to explain multidimensional detonations because the length scale of the instability is the induction distance. Since simplified chemistry is sufficiently accurate to explain the cellular structure, it will be discussed first in the next section.

2.3 Detonations With Simplified Kinetics

Based on the previous sections, it is possible to solve a one–dimensional detonation problem using a simplified reaction mechanism. Assuming the reaction mechanism to consist of one irreversible, exothermic reaction $A \rightarrow B$ with an exothermic energy release $h_A^0 - h_B^0 = \Delta h^0 = q_0 > 0$, the Arrhenius forward reaction rate is given as

$$[k\,(T)]_f = k \exp\left(-E_a/\tilde{R}T\right) \tag{2.11}$$

where E_a is the specific total energy of species A and $\tilde{R}$ is the universal gas constant. The mass production rates are now given as

$$W_A\dot{\omega}_A = -W_B\dot{\omega}_B = -k\rho_A \exp\left(-E_A/\tilde{R}T\right) \tag{2.12}$$

where W is the molecular weight and $\dot{\omega}_A$ is the chemical production rate of species. With the perfect gas assumption of $\gamma = \gamma_A = \gamma_B$, and Y_B the mass fraction of products B, the hydrodynamic pressure can be evaluated as:

$$P = (\gamma - 1)\left(\rho e - \rho\left(1 - Y_B\right) h_A^0 - \rho Y_B h_B^0\right). \tag{2.13}$$

Since the reaction is irreversible, h_B^0 can be assumed to be zero, and $q_0 = \Delta h^0$, thus, Eq. 2.13 transforms into

$$P = (\gamma - 1)\left(\rho e - \rho\left(1 - Y_B\right) q_0\right) \tag{2.14}$$

Equation 2.14 is the equation of state for the simplified reaction model. Together with the the integrated governing equations in Sec. 2.1 and the new equation of state 2.14, the system of governing equations is augmented by the species mass balances as given below:

$$\begin{aligned}
&\rho_0 u_0 = \rho_1 u_1 \\
&P_0 + \rho_0 u_1^2 = P_1 + \rho_1 u_1^2 \\
&h_0 + \frac{1}{2} u_0^2 = h_1 + \frac{1}{2} u_1^2 \\
&P = (\gamma - 1)\left(\rho e - \rho\left(1 - Y_B\right) q_0\right) \\
&\rho_0 u_0 Y_B = \rho_1 u_1 Y_B + k\rho\left(1 - Y_B\right) \exp\left(\frac{-E_A}{W_A \tilde{R} T}\right).
\end{aligned} \tag{2.15}$$

The burned and unburned states have been renamed as 1 and 0 respectively. The parameter $\left(\frac{-E_A}{W_A}\right)$ is referred as the "activation energy" and denoted by E_0^*.

2.3.1 Paramteric Normalization

The integrated equations in Eq. 2.15 can be made invariant of the preshock acoustic temperature using normalization so that all the parameters are dimensionless.

The normalization factors used here have been chosen based on the factors used by Bourlioux and Majda [13, 14]. The normalized parameters are given below:

$$\begin{aligned} P &= \tfrac{p}{p_0}, \quad V = \tfrac{v}{v_0} = \tfrac{\rho_0}{\rho}, \quad U = \tfrac{u}{\sqrt{p_0 v_0}}, \quad D = \tfrac{d}{\sqrt{p_0 v_0}} \\ \bar{E} &= \tfrac{E}{p_0 v_0}, \quad Q_0 = \tfrac{q_0}{p_0 v_0} \quad E_0^* = \tfrac{E_A^*}{p_0 v_0} \quad \bar{K} = \tfrac{k}{\sqrt{p_0 v_0}} \end{aligned} \tag{2.16}$$

The reaction rate equation can be normalized to

$$\bar{K} r\left(Y_B\right) = \bar{K} \frac{1 - Y_B}{DV} \exp\left(-\frac{E_0^*}{PV}\right) \tag{2.17}$$

The length can be normalized based on the half–reaction length which is defined as the distance between the detonation front and the point where half of the reaction progress is equal to 1/2, i.e., $L_{1/2} = \int_0^{1/2} \frac{dY_B}{rY_B}$. The length scale is normalized as:

$$X = \frac{x}{\left(\frac{L_{1/2}}{\bar{K}}\right)} \tag{2.18}$$

The speed of sound is normalized to $C_0 = \sqrt{\gamma}$ and detonation velocity is $D = DU + U$. The Rayleigh lines and the Hugoniot curve can now be non–dimensionalized as

$$\begin{aligned} &\frac{P-1}{1-V} = D^2 \\ &\left(P + \mu^2\right)\left(V - \mu^2\right) = 1 - \mu^4 + 2\mu^2 Y_B Q_0 \end{aligned} \tag{2.19}$$

where $\mu = \frac{\gamma-1}{\gamma+1}$ for brevity.

At the CJ point, the pressure and density calculations can be normalized to

$$P_{CJ} = \tfrac{D_{CJ}^2+1}{\gamma+1}, \quad V_{CJ} = \tfrac{\gamma\left(D_{CJ}^2+1\right)}{(\gamma+1)D_{CJ}^2} \tag{2.20}$$

Hence, D_{CJ}^2 can be found by substituting the normalized pressure and density parameters into the Hugoniot equation, resulting in a quadratic equation:

$$D_{CJ}^2 - \left\{\sqrt{4\gamma + 2\left(\gamma^2 - 1\right) Q_0}\right\} D_{CJ} + \gamma = 0 \tag{2.21}$$

Note that the mass fraction term has dropped out of the detonation velocity calculation. This is due to the chemical reaction attaining equilibrium at the CJ point, and for a single step irreversible reaction this implies that $Y_B = 1$. Equation 2.21 has two roots, one with a solution in the detonation branch of the Hugoniot curve and the other in the deflagration branch of the Hugoniot curve. Hence, the detonation velocity is given as

$$D_{CJ} = \sqrt{\frac{(\gamma^2 - 1)\, Q_0}{2} + \gamma} + \sqrt{\frac{(\gamma^2 - 1)\, Q_0}{2}} \tag{2.22}$$

Since $M_{CJ} = 1$, the velocity of burned gases is the same as the speed of sound in burned gases, given by

$$U_{CJ} = C_{CJ} = \sqrt{\gamma P_{CJ} V_{CJ}} \tag{2.23}$$

One more important parameter, called "overdrive parameter" is introduced here. It is essentially the relationship of the actual detonation velocity to the velocity at the CJ point and is given as:

$$f = \left(\frac{D}{D_{CJ}} \right)^2 \tag{2.24}$$

2.4 Detonations With Detailed Kinetics

In this section, the methodology for detonations using single–step kinetics is extended to detailed chemistry involving multiple species and reversible reactions. The only change from the single–step modeling is the chemical rate equation given as

$$\frac{\partial}{\partial x} (\rho_i u Y_i) = W_i \dot{\omega}_i \left(\rho_i \frac{Y_i}{W_i}, \cdots, \rho_k \frac{Y_k}{W_k} \right), \quad i = 1, \cdots K \tag{2.25}$$

where i is the species index and K is the total number of species in the chemical reaction.

The difference between the simplified model and the detailed chemistry models is that the RHS of Eq. 2.25 requires the computation of density and temperature at every step. Also, the calculation of the density, pressure and velocity is different from the single–step model and requires the full system of stationary transport equations to be solved simultaneously [40]. To solve the source terms, a semi–implicit fourth–order Runge–Kutta method based on Rosenbrock–Wanner family of methods developed by Kaps [41] has been employed. A root finding algorithm using a combination of bisection and secant method, developed by Sandia National Laboratories, has been coupled to the Runge Kutta solver [42]. Due to the difference in chemical and hydrodynamic time–scales, the resulting ODE equations are stiff in nature, thus requiring the use of an ODE solver. For this purpose, a backward differentiating solver is used.

Similar to the simplified chemistry model, the CJ state values need to be calculated. NASA-CEA code has been used to calculate the CJ parameters as input for the detailed chemistry model [43].

Detonations involving detailed chemistry have a very distinctive induction zone, given as the length–scale l_{ig}. The induction length is used as the length scale for the simulations involving detailed chemistry. It is calculated as the product of induction time, which is the time taken from ignition to measurable chemical reaction, and the von Neumann velocity.

2.5 Detonation Front Structure

Our knowledge of the detonation front structure has been gleaned from an immense experimental effort and few numerical simulations. The key feature of the structure are the transverse waves. These secondary shocks are joined to the shock front in a conventional three–shock configuration, in what is known as “triple point”,

where the Mach stem and the incident shock form the leading shock and the transverse wave is the reflected shock. The transverse waves are not steady waves, but continuously decaying, and periodically collide with other transverse waves moving the opposite direction. Understanding of the transverse instability phenomenon requires the study of the structure composed by the shock front and the transverse waves, their coupling with the acoustic modes and their behavior in transient conditions. These topics are discussed in the next two sections.

2.5.1 Cellular Structure

Confined detonations typically have a cell size one or two orders of magnitude greater than the induction length. Strehlow and his coworkers have conducted much of the work on the topic of detonations as evidenced by his voluminous literature [7, 44, 45, 46, 47]. In general, it has been observed that regular structure is favored by low initial pressure and high dilution with inert gases. In particular, Strehlow found that fuel–lean mixtures were more regular than fuel–rich mixtures [46]. In Chapter 1, the imprint of the triple–point was illustrated to show the cellular structure.

There is a class of detonation waves where the primary instability is longitudinal, known as 'galloping detonations'. The earliest experimental study with galloping detonations was reported by Saint–Cloud et al. [48] where a deflagration-to-detonation mechanism resulted in an extreme longitudinal oscillation which propagated the wave much faster than regular detonations waves. The role of acoustic waves in one–dimensional longitudinal oscillatory instabilities, increasing the wave speed to a gallop was reported by Clavin [49]. Massa et al. [50] provided some insight into thermo–acoustic effects due to the coupling of non–equilibrium heat release and pressure perturbation. Thermo–acoustic effects have been reported in other similar phenomena, like supersonic–jet instability. The high temperature non–equilibrium

thermo–chemistry of carbon–oxygen mixtures affect the instability of supersonic jets by dampening out some acoustic and vortical modes to the extent that only a finite number of them persists and only below a certain limit frequency [51]. An analogous effect is found to occur in feedback waves with negative phase speed.

2.5.2 Transverse Wave

Strehlow and his co–workers conducted systematic experiments to understand the multi–dimensional nature of detonations in rectangular channels and one of the topics on great interest for them was transverse waves [7, 46, 47]. Gordeev discovered that transverse waves appear when a strong perturbation is applied to an existing front and concluded that the perturbation upsets the balance of the shock causing it to split into two and setting of transverse waves [52].

Transverse waves in established detonations are not steady structures but transient decaying phenomena. The average propagation velocity of transverse waves is only slightly above the speed of sound in the final equilibrium state. Bourlioux and Majda, using linear stability analysis of the growth rate of transverse oscillations, showed that the cell width Z corresponds to the most unstable wavelength in the transverse direction [14]. But one of the important concerns regarding transverse waves is whether they can undergo the period–doubling phenomenon similar to longitudinal waves and if so, whether the bifurcation of transverse waves have any effect on the wave structure and propagation. A Floquet analysis of the multidimensional transverse instability for simple chemical kinetics is provided in the results section.

CHAPTER 3

MODELING OF DETONATIONS

3.1 Mathematical Formulation

The equations used to model reactive flow are the time–dependent reactive Euler equations of conservation mass, momentum, energy and reaction, give in tensor notation as:

$$\begin{aligned}
&\frac{\partial \rho}{\partial t} + \nabla \cdot (\rho \mathbf{v}) = 0 \\
&\frac{\partial \rho \mathbf{v}}{\partial t} + \nabla \cdot (\rho \mathbf{v}\mathbf{v}) + \nabla \cdot \mathbf{P} = 0 \\
&\frac{\partial E}{\partial t} + \nabla \cdot (E\mathbf{v}) + \nabla \cdot (\mathbf{v} \cdot \mathbf{P}) = 0 \\
&\tfrac{\partial Y_i}{\partial t} + \nabla \cdot (Y_i \mathbf{v}) = \tfrac{W_i \dot{\omega}_i}{\rho}, \quad i = 1, \cdots, K
\end{aligned} \tag{3.1}$$

The first term in all the equations represents the rate of change of the flow solution and the second term describes the convective fluid dynamic effects. The pressure tensor $\mathbf{P}$, total density ρ and energy E used here are defined by:

$$\begin{aligned}
&\mathbf{P} = P(\rho, T)\,\mathbf{I} \\
&\rho = \sum_{i=1}^{K} \rho_i \\
&E = \frac{1}{2}\rho \mathbf{v} \cdot \mathbf{v} + \sum_{i=1}^{K} \rho_i h_i - P
\end{aligned} \tag{3.2}$$

The expression for the thermal equation of state is given by:

$$P = \sum_{i=1}^{K} P_i = \sum_{i=1}^{K} \rho_i R_i T \tag{3.3}$$

The chemical production rates are derived from a reaction mechanism consisting of N_r reactions per unit volume is given by

$$\dot{\omega}_i\left(C_1,\cdots,C_K,T\right)=\sum_{j=1}^{N_r}\left(\nu_{j,i}^r-\nu_{j,i}^f\right)\left[k_j^f\prod_{l=1}^{K}C_l^{\nu_{j,i}^f}-k_j^r\prod_{l=1}^{K}C_l^{\nu_{j,i}^r}\right],\quad i=1,\cdots,K \tag{3.4}$$

with k_j^f and k_j^r denoting the Arrhenius forward and reverse reactions rate of each chemical reaction, give as

$$\begin{aligned} k_j^f\left(T\right)&=A_j^f T^{\beta_j^f}\exp\left(-E_j^f/\tilde{R}T\right)\\ k_j^b\left(T\right)&=A_j^b T^{\beta_j^b}\exp\left(-E_j^b/\tilde{R}T\right)\end{aligned} \tag{3.5}$$

The evaluation of Eq. 3.4 and 3.5 is accomplished by using *CHEMKIN-III* [53] and Westbrook hydrogen–oxygen–argon reaction mechanism [54].

The speed of sound is calculated as

$$c=\left[\gamma\left(\sum_{i=1}^{K}Y_iR_iT\right)\right]^{1/2} \tag{3.6}$$

A specific solution of the reactive flow equations is determined by the initial conditions, the set of reacting species and their fluid dynamic, thermophysical and thermochemical properties, and the boundary conditions that describe the geometry of the system. Boundary and initial conditions select out the solution that applies to the particular problem under study from many families of possible solutions. The physical and numerical implications of the particular boundary conditions influence the numerical techniques used.

There are 4 possible boundary conditions: inflow, outflow, symmetry plane and wall. For inviscid Euler equations, the symmetry and wall condition behave the same and are considered to be reflective. Along the symmetry or wall plane, the component of velocity vector normal to the boundary is zero i.e.

$$\mathbf{v}\cdot\mathbf{n}=0 \tag{3.7}$$

For inlet, the Dirichlet conditions are applied and for outlet, the Neumann conditions are employed [55].

3.2 Numerical Formulation

In this section, the standard approach in constructing high resolution Finite Volume (FV) upwind schemes are described. The hybrid Riemann solver of Roe and Harten–Lax–van Leer (HLL) are derived. The hybrid scheme is useful due to the propensity of Roe scheme to introduce non–physical energy densities, upon which the HLL scheme was devised [56]. For higher order approximation, the Monotone Upstream–centered Schemes for Conservation Laws (MUSCL) reconstruction approach is employed. Due to the propensity of upwind schemes to introduce oscillations in the presence of a discontinuity, a Harten–Hyman entropy fix is added to the Roe scheme in the flux approximation process [57]. The numerical integration of the stiff reaction terms is undertaken with an operator splitting approach.

3.2.1 General Formulation for FV Conservation Laws

The finite volume method is based on subdividing the spatial domain into intervals, also called "grid cells" and tracking the flux q over each of the volumes. In each time–step, the flux values are updated using approximations through the endpoints of the intervals. The value Q_i^n will approximate the average value at time t^n as:

$$Q_i^n \approx \frac{1}{\Delta x} \int_{x_{i-1/2}}^{x_{i+1/2}} q\left(x, t_n\right) dx \tag{3.8}$$

where $\Delta x = x_{i+1/2} - x_{i-1/2}$ is the length of the cell. For sake of simplicity, the assumption is uniform Cartesian meshes. If q is a smooth function, then Eq. 3.8

agrees with a value of q at the midpoint of the interval to $O(\Delta x^2)$.The integral form of the conservation law is given by:

$$\frac{d}{dt}\int q(x,t)dx = f\left(q\left[x_{i-1/2},t\right]\right) - f\left(q\left[x_{i+1/2},t\right]\right) \tag{3.9}$$

By working with cell averages, it is easier to use the important properties of the conservation. This is particularly important in accurately calculating shock waves, conservation form ensures that the total mass within the computational domain is preserved and varies correctly with the implementation of proper boundary conditions.

Equation 3.9 can be used to develop an explicit time–marching algorithm, given Q_i^n, the cell average at time t_n. Thus an approximation of Q_i^{n+1} can obtained as:

$$Q_i^{n+1} = Q_i^n - \frac{\Delta t}{\Delta x}\left(F_{i+1/2}^n - F_{i-1/2}^n\right) \tag{3.10}$$

where $F_{i\pm1/2}^n$ is the approximation to the average flux along $x = x_{i\pm1/2}$ given by

$$F_{i\pm1/2}^n \approx \frac{1}{\Delta t}\int_{t_n}^{t_{n+1}} f\left(q\left(x_{i-1/2},t\right)\right)dt \tag{3.11}$$

For a hyperbolic problem, $F_{i-1/2}^n$ can be found based on the values Q_{i-1}^n and Q_i^n, the cell averages of either side of the interface. Then Eq. 3.10 becomes

$$Q_i^{n+1} = Q_i^n - \frac{\Delta t}{\Delta x}\left(\Phi\left(Q_i^n, Q_{i+1}^n\right) - \Phi\left(Q_{i-1}^n, Q_i^n\right)\right) \tag{3.12}$$

where $F_{i+1/2}^n = \Phi\left(Q_i^n, Q_{i+1}^n\right)$.

3.2.2 Stability - CFL condition

An essential requirement for the numerical method to be convergent i.e. the numerical solution should converge to the solution of the differential equation accurately

is stability. The CFL condition, named after Courant, Friedrichs and Lewy [58], is a necessary condition that must be satisfied by any FV method to ensure stability and convergence. The CFL condition requires the computational method to mimic the propagation of information as in the physical phenomenon, as determined by the eigenvalues of the flux Jacobian. A sequence of approximate solutions are defined initially and as the grid refines, the solution is checked for convergence. It is noted that the CFL condition is only a necessary condition for stability and not a sufficient condition to guarantee stability.

In order for the CFL condition to be satisfied, for a hyperbolic system of equations generally having a set of m wave speeds $\lambda_1, \cdots, \lambda_m$, the Courant number given by ν is

$$\nu \equiv \max |\lambda_i| \frac{\Delta t}{\Delta x}. \tag{3.13}$$

Since hyperbolic methods typically use explicit methods as derived earlier, the Courant number is always slightly lesser than 1. This is useful to fix the ratio $\Delta t/\Delta x$ as the grid is being refined due to the necessity of increasing resolution at the same rate in both space and time.

3.2.3 Godunov's method

Godunov proposed a numerical method to solve non–linear Euler equations by solving the non–linear Riemann problem at the cell interface [59]. Recalling the Q_i^n represents an approximation of the cell average q,

$$Q_i^n \approx \frac{1}{\Delta x} \int_{x_{i-1/2}}^{x_{i+1/2}} q\left(x, t_n\right) dx \tag{3.14}$$

the piecewise constant representation defined by these cell values can be used as initial data $\tilde{q}^n(x, t_n)$ and solving this over time results in $\tilde{q}^n(x, t_{n+1})$. This is then averaged over each cell to obtain

$$Q_i^{n+1} = \frac{1}{\Delta x} \int_{x_{i-1/2}}^{x_{i+1/2}} \tilde{q}^n(x, t_{n+1})\, dx. \tag{3.15}$$

For a small enough time–step Δt, the exact solution of $\tilde{q}^n(x, t_n)$ is determined by piecing together the Riemann problem solutions from each cell interface.

The cell average is updated through the formula in Eq. 3.10,

$$F_{i-1/2}^n = \Phi\left(Q_{i-1}^n, Q_i^n\right) = f\left(q^{\downarrow}\left(Q_{i-1}^n, Q_i^n\right)\right) \tag{3.16}$$

where $q^{\downarrow}$ refers to the left q_l and right q_r states of the of the Riemann problem.

Implementation of the Godunov's family of methods does not require the full structure of the Riemann solution at each interface, just the value of $q^{\downarrow}$ at each interface. In the case of detonations, the intermediate states where the Hugoniot and integral curves intersect are determined and $Q_{i-1}^{\downarrow}$ will result in one of the states. Since very little information of the Riemann solution, it is easier to approximate the Riemann solution by not compromising on the accuracy.

Reactive flow are essentially wave propagation problems, so Godunov's method in wave propagation formulation is given by

$$Q_i^{n+1} = Q_i^n - \frac{\Delta t}{\Delta x}\left(A^+ \Delta Q_{i-1/2} + A^- \Delta Q_{i+1/2}\right) \tag{3.17}$$

where the cell–averaged fluctuations are defined as

$$\begin{aligned} A^- \Delta Q_{i+1/2} &= f\left(Q_{i-1/2}^{\downarrow}\right) - f\left(Q_{i-1}\right) \\ A^+ \Delta Q_{i-1/2} &= f\left(Q_i\right) - f\left(Q_{i-1/2}^{\downarrow}\right) \end{aligned} \tag{3.18}$$

3.2.3.1 Convergence for Godunov's method

If a sequence of numerical approximations converges to a function q as the grid is refined, then the limit function of q is a weak solution of the conservation law. This equality can be reassuring when a discontinuity is computed on a fine grid, the solution is accurate as it is close to some weak solution. This is not true for non–conservative methods. Unfortunately, it is inevitable that a conservative method can converge to entropy violating weak solutions. In Euler's equations, the physical entropy provides an entropy function, in which case the limiting solution provided by Godunov's method usually provides physically accurate solutions, in the eventuality of non–physical solutions, there is a need to perform an entropy fix as explained later in this section.

3.2.4 Approximate Riemann Solvers

As mentioned earlier in this document, to solve the Riemann problem using Godunov's method, the entire structure of the Riemann problem is not required to be known. The only terms which need to be determined are the $q^{\downarrow}(q_l, q_r)$ states, along $x/t = 0$. To compute $q^{\downarrow}$ however, the full wave structure and wave speeds in order to determine where $q^{\downarrow}$ lies in state space. Since $q^{\downarrow}$ lies in the intersection of the Hugoniot and integral curves, it is in the intermediate states of shocks and rarefactions in the process of connecting q_l and q_r.

A wide variety of approximate Riemann solvers have been proposed to counter the computational expense of an exact Riemann solver, without compromising accuracy when used on Godunov schemes [60, 61, 57]. The speedup of the Riemann solver has a major impact on the efficiency Godunov–type methods, since the Riemann problem is solved at every cell interface. With the increase in grid interfaces,

the computational expense of Godunov methods exponentially increase, however the expense can be justified for these methods due to their nature of producing the best results for discontinuous problems with fewer grid points.

An approximate Riemann solution for a given data Q_{i-1} and Q_i that approximates the true similarity solution to the Riemann problem, consists of a set of M_w waves $W^p_{i-1/2}$ propagating at speeds given by $s^p_{i-1/2}$ given as

$$Q_i - Q_{i-1} = \sum_{p=1}^{M_w} W^p_{i-1/2} \tag{3.19}$$

Using this function, the Godunov's method can be generalized by using the waves and speeds from the approximate Riemann's solution as

$$\begin{aligned} A^- \Delta Q_{i-1/2} &= \sum_{p=1}^{M_w} \left(s^p_{i-1/2}\right)^- W^p_{i-1/2} \\ A^+ \Delta Q_{i-1/2} &= \sum_{p=1}^{M_w} \left(s^p_{i-1/2}\right)^+ W^p_{i-1/2} \end{aligned} \tag{3.20}$$

Using the above relationships, Eq. 3.17 can be updated. This approximation holds true only if the Rankine–Hugoniot conditions is satisfied across each wave. This approximation also stands the chance of losing its conservative property if special care is not taken in defining the approximate solution.

3.2.4.1 Roe Linearization

The defining of an approximate Riemann solution can be undertaken by substituting the non–linear problem by a linearized equation defined locally at each cell interface, as follows:

$$\hat{q}_t + \hat{A}_{i-1/2}\hat{q}_x = 0. \tag{3.21}$$

The matrix $\hat{A}_{i-1/2}$ is selected to be an approximation to $f(q)$ valid in the neighborhood of $Q_{i-1/2}$ and Q_i. The matrix should also be diagonal so that Eq. 3.21 is hyperbolic, and should also possess a capability to connect $Q_{i-1/2}$ and Q_i by a single wave W^p, where that wave is also an eigenvector. If this property can hold, then the approximate Riemann solution will also consist of this single wave and hence will agree to the exact solution. Because of this property, the $\hat{A}_{i-1/2}$ can now be defined in terms of wave speed as

$$f(Q_i) - f(Q_{i-1}) = s(Q_i - Q_{i-1}) = \hat{A}_{i-1/2}(Q_i - Q_{i-1}). \tag{3.22}$$

This is a very useful condition to impose on the matrix, as it will ensure conservation provided the following equation is satisfied,

$$A^- \Delta Q_{i-1/2} + A^+ \Delta Q_{i-1/2} = f(Q_i) - f(Q_{i-1}). \tag{3.23}$$

Roe discovered a way to find the state matrix for Euler equations, by integrating through intermediate functions to obtain $A^- \Delta Q_{i-1/2}$ [62]. By Roe's linearization, the state matrix is found by

$$\begin{aligned} \hat{C}_{i-1/2} &= f(Q_i) - f(Q_{i-1}) \\ \hat{B}_{i-1/2} &= Q_i - Q_{i-1} \\ \hat{A}_{i-1/2} &= \frac{\hat{C}_{i-1/2}}{\hat{B}_{i-1/2}}. \end{aligned} \tag{3.24}$$

Harten et al. showed that an integration scheme of this kind can always be used to define the matrix $\hat{A}$ provided the system has a convex entropy function. For Euler equations with ideal polytropic gas equation of state, Roe proposed the parameter vector $z = \rho^{1/2} q$, leading to the following Roe linearized parameters for velocities, total specific enthalpies and speed of sound:

$$\hat{u} = \frac{\sqrt{\rho_{i-1}}u_{i-1} + \sqrt{\rho_i}u_i}{\sqrt{\rho_{i-1}} + \sqrt{\rho_i}}$$
$$\hat{H} = \frac{\sqrt{\rho_{i-1}}H_{i-1} + \sqrt{\rho_i}H_i}{\sqrt{\rho_{i-1}} + \sqrt{\rho_i}} = \frac{\left(\frac{E_{i-1}+p_{i-1}}{\sqrt{\rho_{i-1}}}\right) + \left(\frac{E_i+p_i}{\sqrt{\rho_i}}\right)}{\sqrt{\rho_{i-1}} + \sqrt{\rho_i}} \tag{3.25}$$
$$\hat{c} = \sqrt{(\gamma-1)\left(\hat{H} - \frac{1}{2}\hat{u}^2\right)}.$$

Toro lists all the possible Roe linearized parameters for a variety of gasdynamics problems which have been used in this research work [57].

3.2.4.2 Harten–Hyman Entropy Fix

The use of Roe's linearization forces only discontinuities on the approximate Riemann solution, without rarefaction waves. This leads to a violation of entropy. The use of entropy–violating Roe's approximate Riemann solution leads to difficulties only in the case of a transonic rarefaction wave (as in the case of detonations), in which $f'(q_l) < 0 < f'(q_r)$. In this scenario, it becomes necessary to modify the approximate Riemann solver in order to obtain entropy satisfying conditions.

A more general approach was used by Harten and Hyman to solve the Riemann problem at sonic conditions [63]. If there is a transonic k wave in $\lambda_l^k < 0 < \lambda_r^k$ where $\lambda_{l,r}^k$ represents the k^{th} eigenvalue computed in the states $q_{l,r}^k$ given as

$$q_l^k = Q_{i-1} + \sum_{p=1}^{k-1} W^p \tag{3.26}$$

and

$$q_r^k = q_l^k + W^k \tag{3.27}$$

The single wave represented as W^k is substituted by two waves $W_l^k = \beta W^k$ and $W_r^k = (1-\beta)W^k$. To preserve conservation, the approximate Riemann solution looks like

$$\begin{aligned} \lambda_l^k W_l^k + \lambda_r^k W_r^k &= \hat{\lambda}^k W^k \\ \beta &= \frac{\lambda_r^k - \hat{\lambda}^k}{\lambda_r^k - \lambda_l^k} \end{aligned} \tag{3.28}$$

This entropy fix can be interpreted as a piecewise linear approximation to the flux function in the neighborhood of the sonic point, and hence the Roe method with this entropy–fix converges to the entropy satisfying weak solution.

3.2.4.3 HLL Solver

In some situations, linearized Riemann solvers based on Roe average can fail completely, giving rise of non–physical solutions like negative pressures or densities in Euler equations. This is very common for situations involving rapid and strong expansion. Einfeldt et al. proved that for certain Riemann problems, there is no linearization that will preserve positivity requiring the use of other methods to approximate the Riemann solution [56].

A simple approximate Riemann solver can be based on estimating the largest and smallest wave speeds arising in the Riemann solution, and then taking $\hat{Q}\left(x/t\right)$ to consist of only two waves propagating at speeds $s_{i-1/2}^1$ and $s_{i-1/2}^2$. The waves are modified and taken equal to

$$\begin{aligned} W_{i-1/2}^1 &= \hat{Q}_{i-1/2} - Q_{i-1} \\ W_{i-1/2}^2 &= Q_i - \hat{Q}_{i-1/2}. \end{aligned} \tag{3.29}$$

The state of $\hat{Q}_{i-1/2}$ can now be determined by requiring the approximate solution to be conservative, which requires

$$s_{i-1/2}^1 \left(\hat{Q}_{i-1/2} - Q_{i-1}\right) + s_{i-1/2}^2 \left(Q_i - \hat{Q}_{i-1/2}\right) = f\left(Q_i\right) - f\left(Q_{i-1}\right). \tag{3.30}$$

Rearranging to get $\hat{Q}_{i-1/2}$

$$\hat{Q}_{i-1/2} = \frac{f\left(Q_i\right) - f\left(Q_{i-1}\right) + s^1_{i-1/2}\left(Q_{i-1}\right) - s^2_{i-1/2}\left(Q_i\right)}{s^1_{i-1/2} - s^2_{i-1/2}}. \tag{3.31}$$

This is known as the Harten–Lax–van Leer (HLL) solver [64] and extended by Einfeldt [65] for gas dynamics by assigning s^1 and s^2 as

$$\begin{aligned} s^1_{i-1/2} &= \min\left(\min\left(\lambda^p_{i-1}, \hat{\lambda}^p_{i-1/2}\right)\right) \\ s^2_{i-1/2} &= \max\left(\max\left(\lambda^p_{i}, \hat{\lambda}^p_{i-1/2}\right)\right). \end{aligned} \tag{3.32}$$

In particular, the Einfeldt modified HLL (HLLE) method shares the nice property of Roe solver that for data connected by a single shock wave, the approximate solution agrees with the true solution. In general, an entropy fix is not required for this method, since it is positively conservative which is helpful when encountering low densities.

A slight modification to the HLLE solver is used in this research work, wherein a contact discontinuity is captured accurately by introducing a piecewise linear function as an approximate solution, by replacing the constant intermediate state given in Eq. 3.31 with a linear function carrying the same total integral [65]. By this modified approach, the full Riemann structure is no longer modeled only by the two fastest and slowest waves, hence leading to a better resolution of the discontinuity.

3.2.5 Higher Order Resolution and Accuracy

The approximate Riemann solvers derived above can be extended to high–resolution methods using the following modification to Eq.3.21 as follows:

$$Q^{n+1}_i = Q^n_i - \frac{\Delta t}{\Delta x}\left(A^- \Delta Q_{i+1/2} + A^+ \Delta Q_{i-1/2}\right) - \frac{\Delta t}{\Delta x}\left(\tilde{F}_{i+1/2} - \tilde{F}_{i-1/2}\right) \tag{3.33}$$

where $A^{\pm}\Delta Q_{i\mp 1/2}$ are the fluctuations in the approximate Riemann solver and $\tilde{F}_{i\pm 1/2}$ is the high–resolution correction given by

$$\tilde{F}_{i\pm1/2} = \frac{1}{2}\sum_{p=1}^{M_w} \left|s^p_{i\pm1/2}\right| \left(1 - \frac{\Delta t}{\Delta x}\left|s^p_{i\pm1/2}\right|\right) \tilde{W}^p_{i\pm1/2} \tag{3.34}$$

When the Roe solver is used, then $M_w = m$ and when HLL solver is used, then $M_w = 2$.

Second–order methods similar to Eq. 3.33 have a general tendency to give oscillatory approximations to discontinuous solutions. Even when the solution is smooth, oscillation appear due to the dispersive nature of these methods. The addition of crucial *limiters* leads to a significant improvement for solving non–linear problems. Going back to Eq. 3.34, the last term $\tilde{W}^p_{i\pm1/2}$ can be modified by applying some form of limiter which changes the magnitude of the correction used, depending on the behavior of the solution. The limiting process is complicated by the fact that the solution to a hyperbolic system typically consists of a superposition of waves of several different families, some of which may be smooth and others discontinuous at a given point of time. Hence the limiters are applied in such a way that the discontinuity portion of the solution remains non–oscillatory whereas the smooth portion remains accurate. Methods based on this idea are known as "slope–limiter" methods.

The approximate Riemann method is rewritten as

$$Q^{n+1}_i = Q^n_i - \frac{\Delta t}{\Delta x}\left(A^+\Delta Q_{i-1/2} + A^-\Delta Q_{i+1/2}\right) - \frac{1}{2}\left(\sigma^n_i - \sigma^n_{i-1}\right) \tag{3.35}$$

where σ_i is the slope of the i^{th} cell. If the slopes are chosen to be zero, the original Godunov equations is returned. The behavior of the solution near this i_{th} decides the correct equation for σ^n_i. This approach was introduced by van Leer in a series of papers where he developed the technique now known as MUSCL (Monotone Upstream–centered Schemes for Conservation Laws), specifically for non–linear conservation laws [66, 67, 68]. Details on the limiters can be found in other literature and will not be discussed here [57, 55, 69].

3.2.6 Source Terms

For reactive flow, where the exothermic energy released by chemical reactions has a profound effect on the hydrodynamic flow, the reactions occur in much faster time–steps than fluid dynamics and hence the source terms are "stiff" in nature. One standard approach for reactive flows is to use "operator–splitting" methods. This procedure is quite simple to use and is implemented successfully in the CLAWPACK software. Using operator–splitting, it is possible to use the high resolution methods derived earlier on hydrodynamic terms, with standard ODE solvers for the source terms.

The fractional step methods employed for reactive Euler equations are of the form:

$$\begin{aligned} Step1 &: q_t + \bar{u} q_x = 0 \\ Step2 &: q_t = -\beta q = \psi(q) \end{aligned} \tag{3.36}$$

Here, q_t is the term containing the chemical source terms and is defined as:

$$\psi(q) = W_i \dot{\omega}_i (\rho_1, \cdots, \rho_K) \quad i = 1, \cdots, K \tag{3.37}$$

where W_i is the molecular weight of the species and $\dot{\omega}_i$ is the chemical rate of production dependent on species density and global temperature.

Maintaining convention, Eq. 3.36 can be rewritten in operator form as

$$\begin{aligned} A &= -\bar{u} \partial x \\ B &= -\beta \end{aligned} \tag{3.38}$$

But since β is a function of f, there will be a splitting error, given by:

$$q(x, \Delta t) - q''(x, \Delta t) = \frac{1}{2} \Delta t^2 \bar{u} \beta'(x) q(x, 0) + O\left(\Delta t^3\right) \tag{3.39}$$

Since the splitting error propagates at $O(\Delta t^2)$ at each time–step, this method can only be first order accurate, since after $t/\Delta t$ time–steps, the error becomes $O(\Delta t)$.

An improved fractional-step method called Godunov splitting, yields second order accuracy with a slight modification. The idea is to solve the first step in 3.36 over only half a time step $\Delta t/2$, then use the result as data for a full time–step for the second step in Eq. 3.10, and finally take another half–time step on the first step. This approach was put forward by Strang and is known as "Strang splitting " [70] and the details can be obtained from Ref. [70]. Even though Strang splitting is second order in nature, it's similarity to the Godunov splitting suggests that a first order accuracy might be sufficient. This is because the coefficient of $O(\Delta t)$ can be much smaller than the second order discretization terms arising from Strang splitting.

Since the ODE's are stiff, an appropriate ODE solver is necessary. A linearly implicit fourth–order two stage Runge Kutta method is employed for integrating the stiff reaction terms with local sub–cycling with automatic time–step adjustment. The linearly implicit approach is used here to avoid the computationally expensive solution of non–linear equations, using an implicit update using Trapezoidal Rule [69]. The automatic time step reduction is carried out in accordance to meeting CFL criteria. A detailed discussion of the functioning of linearly implicit methods is avoided here and readers are encouraged to refer to the Rosenbrock–Wanner type solvers explained by Wanner [71].

3.3 CLAWPACK

CLAWPACK, which stands for Conservation Laws Package, is a software package designed by Leveque based on finite volume methods in his book [72, 73]. The algorithms can be applied to a wide variety of hyperbolic problems, simply by providing the appropriate Riemann solver, along with initial data and boundary conditions. The package has capability to solve both linear and non–linear problems. All the

numerical methods employed in this research work has been derived from the computational routines included in CLAWPACK.

CHAPTER 4

PARALLEL ADAPTIVE MESH REFINEMENT FRAMEWORK

This chapter describes the features of the block structured adaptive mesh refinement (AMR)framework which was developed by Berger [74]. This has been implemented as a library built upon MPI parallelization and communication abstractions on an optimal load balancing algorithm. An effective spatial and temporal resolution can be attained using refinement levels in combination with factors at each level. The AMR framework was coupled to a numerical solver package called CLAWPACK (Conservation Laws Package) [69] which implements wave propagation methods to solve homogeneous hyperbolic conservation laws equations using finite volume (FV) methods.

This chapter is organized as follows. Section 4.1 reviews various solution adaptive mesh refinement techniques and pertinent literature on the the topic is provided. The rationale behind the use of block–structured AMR in this research is provided in Sec. 4.2. The design of the parallel AMR framework detailing the domain decomposition, partitioning, error estimation, refinement and load balancing strategies are given in Sec. 4.3. The framework is implemented using DAGH (Distributed Adaptive Grid Hierarchies) [75]. Section 4.4 discusses the implementation of numerical solvers using CLAWPACK. Section 4.5 provides two validation cases to test the accuracy and efficiency of the AMR framework to close out the chapter.

4.1 Introduction

The solution of reactive flow problems involves computations across a broad range of spatial and temporal scales. There have been documented cases of adaptive mesh refinement (AMR) reducing computational expense without compromising accuracy [76, 77]. For reactive flows of high complexity, such as detonations, failure of computations to resolve all the pertinent scales can be overcome by using mesh refinement techniques [78]. There are three fundamental strategies that can be employed for dynamic adaptive grid refinement as illustrated in Figure 4.1. The first approach

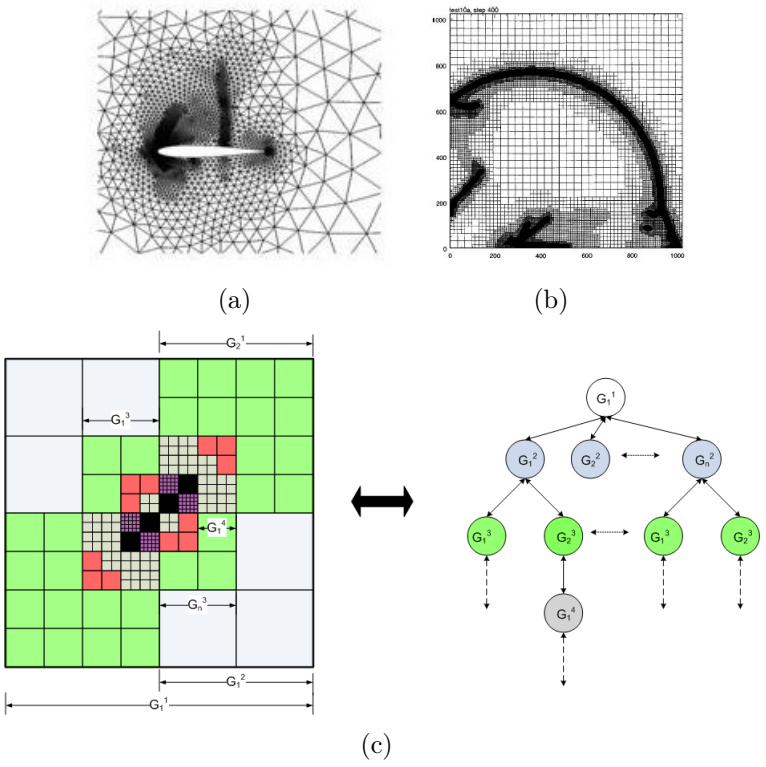

Figure 4.1. The three strategies of mesh refinement: (a) Unstructured method employing a graph–like representation (b) Structured method involving individual cell refinements (c) Hierarchical structured method employing patch–wise mesh refinement.

relies on unstructured meshes and develops a finite element approximation suitable

for complex geometries [79]. Unstructured adaptive methods store the solution using 'graph' or 'tree' representations; these methods are called unstructured because connectivity information must be stored for each unknown 'node' of the graph [80]. However, with the advent of cache–based processors, the performance of unstructured mesh refinement was very poor as a lot of computational time was spent in memory referencing. The second approach was developed by Kokhlov, to refine individual grid cells [81]. This method has the advantage of completely avoiding the requirement of ghost–cells, but requires a large number of memory allocation calls, especially for rapidly evolving simulations. This will add to the overhead in communication and become computationally expensive for complicated problems. The third approach, where grids are refined as blocks or 'patches', was pioneered by Berger, who used a hierarchy of Cartesian grids to cover the computational domain [82]. This technique is known as "block–structured AMR". It consists of a hierarchy of nested mesh levels in which each level consists of many rectangular grids. Each rectangular grid in the hierarchy represents a structured block of many thousands of unknowns [83].

The advantage of patch–wise refinement is due to the overlapping of sub-grids on the base grid depending on the refinement level can have arbitrary shapes. This strategy has proven to be memory efficient; it has inherent parallelism, but requires complex load–balancing schemes. Quirk provided a variant of the Berger method, wherein the error estimation procedure was conducted in parallel and re–gridding was carried out in a serial fashion [84]. It was also successfully attempted to bisect the grid blocks in each coordinate direction, thereby establishing a hierarchy of sub–grids [85]. Hence, this research was carried out using block–structured approach for the reasons of inherent parallelism.

Structured adaptive mesh refinement (SAMR)methods are moderately complex to implement because they rely on dynamic data structures. Regions of the

computational space are dynamically refined in response to run–time estimates of local solution error resulting in highly irregular data dependencies and communication patterns. On parallel platforms, effective managing data distributed across processor memories and orchestrating interprocessor communication and synchronization is vital to avoid unnecessary computational expenditure. In problems like reactive flow, adaptive applications change in response to the dynamics of the problem and little can be known about the structure of the computation at compile–time. Thus, the domain decomposition and load–balancing strategies are triggered at run–time. There have been several packages specifically designed for SAMR. Most are written in C/C++ due to the advantages in data handling, with the ability of linking in FORTRAN with MPI for parallel runs. AMROC [86], PARAMESH [87] and DAGH [75] were object–oriented approaches to solving for compressible, reactive flow problems. The characteristic of DAGH was the use of an error–estimator which compared the solution at two different refinement levels at each grid point. FLASH [88] was a framework developed specifically to study thermonuclear reactions like supernovae with length scales from a few centimeters to kilometers. Currently, the packages which are in active development are SAMRAI [89], Chombho [90] and OVERTURE [91].

4.2 Structured Adaptive Mesh Refinement (SAMR) Algorithms

This section provides a thorough description of SAMR algorithms. The salient features which are adopted in the design of the framework are discussed here. Berger [82] proposed a dynamically adaptive mesh refinement framework using a hierarchy of nested, locally structured finite difference grids. This technique was later extended to hyperbolic conservation laws in three dimensions [74]. The strategy was to recursively embed blocks of finer grids in coarse grids until the solution is obtained

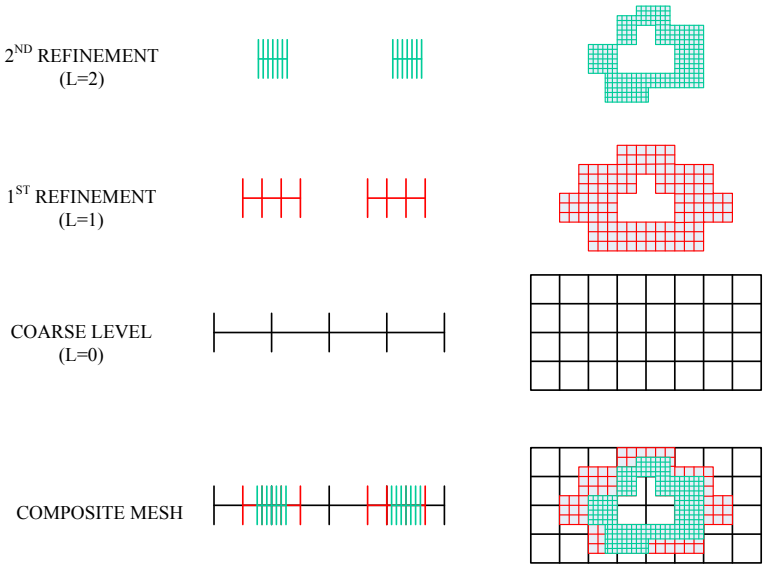

Figure 4.2. 1D and 2D structured mesh hierarchy showing two levels of refinement, with mesh spacing twice of previous coarser level (refinement factor of 2).

with sufficient resolution. All grids at the same level of the hierarchy have the same mesh spacing, with successive levels having a finer spacing. The successive levels are known as refinement levels. The difference in the mesh spacing between two refinement levels is known as a "refinement factor" and is typically 2 or 4. Figure 4.2 illustrates the implementation of the composite mesh as a hierarchy of grids in both 1D and 2D. The grid hierarchy consists of two levels of refinement with a refinement factor of 2.

The scheme can dynamically insert or remove fine grid patches based on the accuracy of the solution, which is calculated by an error estimation procedure, calculated at runtime. These new higher–resolution grids are known as refinement patches, and are used only when the error condition, typically the Courant–Friedrichs–Lewis number, is met. A temporal explicit scheme is stable on all grids in the hierarchy for a given CFL condition. One of the features of SAMR algorithms is the communica-

tion of numerical information among the grids in the same level of the hierarchy and also between the levels of the hierarchy. To facilitate this communication, a "ghost cell" region is padded around the boundary of each grid patch. This ghost cell region locally caches information from adjacent grids and from the next coarser level of the hierarchy. Due to the irregular and unpredictable nature of the refinement, a proper infrastructure is mandatory to handle ghost cell synchronization [92]. It is noted here that the ghost cell synchronization and the communication interface is mandatory for SAMR algorithms, and should not be confused as implementation artifacts. For applications which do not involve complex geometries, SAMR methods offer more advantages compared to unstructured meshes. In SAMR, when a point is flagged for refinement, it is highly likely that neighboring points require refinement. The grid hierarchy may be non–uniform, however the patches themselves are uniform, hence the information need to be stored only for the patches not for individual cells. This makes replication easier across processors in a parallel deployment. Unstructured representations on the other hand require connectivity information for each unknown in the domain resulting high memory overheads.

4.3 Design Of Parallel AMR Framework

A typical AMR framework consists of a grid generator to create fine grid patches, an error estimator to calculate the local truncation error, a hierarchical data structure to store and allocate grid data, an interpolator for updating the solution on newly created grid patches and, finally, a conservation fix-up to ensure flux conservation between coarse and fine grid cells. All of the above mentioned routines can be expressed in a global integration cycle. Keeping in mind that distributed memory clusters do not have adequate memory to store the entire data of large-scale problems, the grid hierarchical data must also be distributed to available nodes. Hence,

the parallelization strategy must take into account the communication overhead and optimally balance the workload.

Figure 4.3 is an overview of the proposed AMR framework. The coarse mesh is initially partitioned and distributed to the available processors. The numerical solver carries out a few iterations to determine the numerical error. After the error estimation is performed and cells are flagged for refinement, an evaluation of the mesh for load imbalance is performed. If there is no load imbalance, then mesh refinement of the flagged cells is performed. Otherwise, a repartitioning procedure is performed and the new partitions are reassigned to the processors in an efficient manner so as to reduce the time for data movement. If this remapping cost is viable, wherein the overhead is low, and computational gain would be achieved, then the data are redistributed. Otherwise, the new partitioning will be discarded. The mesh is then refined and the solution process is restarted.

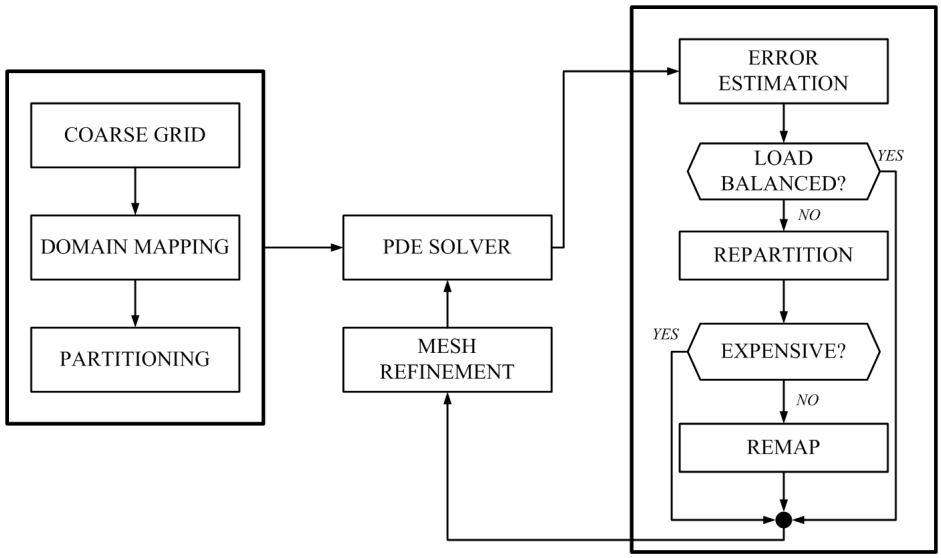

Figure 4.3. Overview of the framework for parallel adaptive computations.

4.3.1 Domain decomposition

Berger proposed the theory behind the domain decomposition technique which can be modified for parallelism [82]. Let the root domain be G_1. Assuming X identical processor nodes in a given distributed parallel computer, the root domain can be decomposed into X regions using load-balanced domain decomposition to yield

$$G_1 = \bigcup_{x=1}^{X} G_1^x, \tag{4.1}$$

where $G_1^x \bigcap G_1^y \neq 0$, $(x \neq y)$. On defining a sequence of levels $l = 1, \ldots, l_{MAX}$, the grid G_1^x can be defined with mesh spacing h_l, with a total number of M_l grids on level l and level $l = 1$ as the coarsest to yield

$$G_1^x = \bigcup_{m=1}^{M_1^x} G_{1,m}^x. \tag{4.2}$$

If there are multiple grids at the first level, proper mesh alignment is ensured by making each grid a subset of the whole space. The important requirement is that higher levels follow the decomposition at the coarsest level by

$$G_l^x = G_l \bigcap G_1^x. \tag{4.3}$$

Equation (4.3) ensures the partitioning of a grid $G_{l,k}$ into multiple grids $G_{l,\kappa}^x$ based on the declared number of processors. Therefore, an appropriate partitioning scheme is required for the creation of a load-balanced decomposition G_1^x.

Since refinement has to occur both in space and time, the mesh refinement ratio has to be defined across all levels in a grid hierarchy for good stability of the numerical scheme under an imposed CFL condition. Berger and Colella [74] defined a simple and effective ratio r given by

$$\frac{\Delta t_l}{\Delta x_l} = \frac{\Delta t_{l-1}}{\Delta x_{l-1}} = \cdots = \frac{\Delta t_1}{\Delta x_1}. \tag{4.4}$$

This strategy implies that more time steps are taken on refined grids than on coarser grids and vastly simplifies the error estimation procedure, thereby increasing the efficiency of the block structured AMR approach. The vector of state on level l, $\mathbf{Q}$, can be defined using a finite set of approximations $\left(x^i_{1,l},\, x^j_{1,l},\, x^k_{1,l}\right)$ as

$$\mathbf{Q}^l = \bigcup_{m=1}^{M_l} \mathbf{Q}\left(G_{l,m},\, x^i_{1,l},\, x^j_{2,l},\, x^k_{3,l}\right). \tag{4.5}$$

Likewise, the numerical fluxes on $G_{l,m}$ can be given as $\mathbf{F}^n$, where n is the number of dimensions such that

$$\mathbf{F}^{1,l} = \bigcup_{m=1}^{M_l} \mathbf{F}^1\left(G_{l,m},\, x^{i+1/2}_{1,l},\, x^j_{2,l},\, x^k_{3,l}\right). \tag{4.6}$$

Equation (4.6) can be extended to three dimensions. The correction terms for the fluxes $\delta\mathbf{F}^n$ are valid only for levels $l > 1$, that is, levels other than the coarse level and are associated to the fluxes of level $l-1$. They are given as

$$\delta\mathbf{F}^{1,l} = \bigcup_{m=1}^{M_l} \delta\mathbf{F}^n\left(\partial G_{i,m},\, x^{i+1/2}_{1,l-1},\, x^j_{2,l-1}, x^k_{1,l-1}\right). \tag{4.7}$$

Equation (4.7) can be extended to three dimensions. If all the values in $\mathbf{Q}$ are set, cell-wise update of flux approximations $F^{n,l}$ can be performed, and when subsequent levels attain the same time, the values in the lower level can be overwritten by the values in the higher level, because higher level values are expected to have higher accuracy. Unfortunately, this leads to a violation of the conservative property of FV cells in the coarse levels. Therefore, a flux correction has to be applied at the coarse levels adjoining a higher level to reclaim lost conservation. Berger and Leveque [32] proposed a conservative fix-up wherein the flux approximation of the coarsest level was replaced by the sum of fine level fluxes of the neighboring cells. The correction is applied as

$$\mathbf{Q}^l_i\left(t + \Delta t_l\right) = \mathbf{Q}^l_i\left(t + \Delta t_l\right) + \frac{\Delta t_l}{\Delta x_{1,l}}\, \delta\mathbf{F}^{1,l+1}_{i-1/2} \tag{4.8}$$

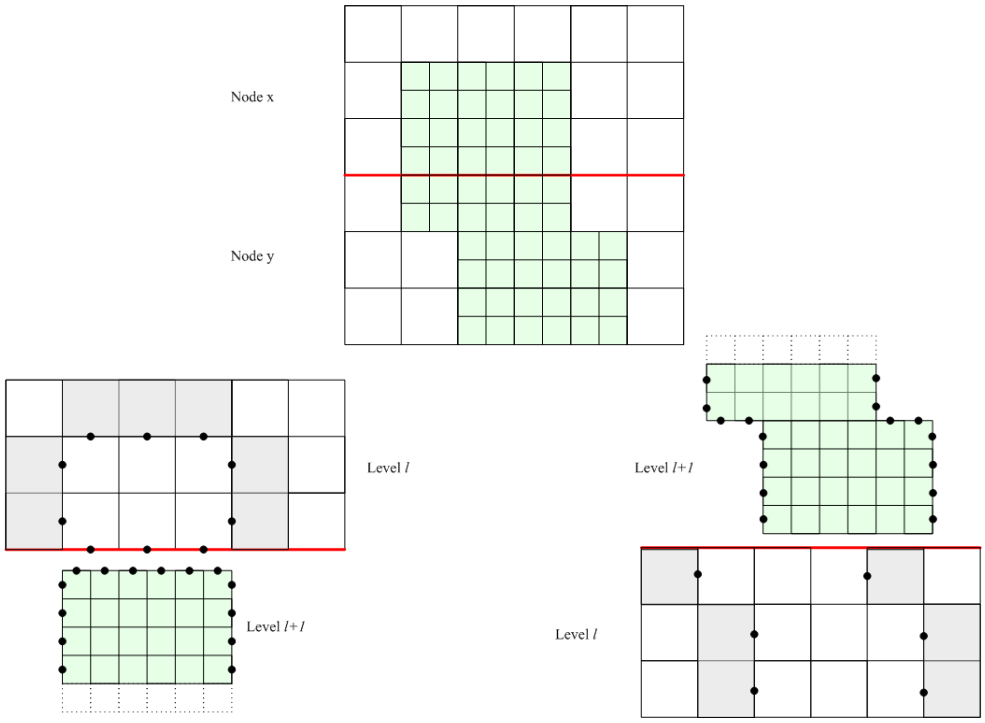

Figure 4.4. Mapping refinement meshes into two processors and performing parallel conservation fix-up.

Figure 4.4 illustrates the mapping and conservation fix-up of a domain. The cells shaded are flagged for correction. The correction term $\delta \mathrm{F}^{1,l+1}_{i-1/2}$ is stored in fine level in node x due to the AMR strategy requiring an interior coarse cell existing on node x having flux in the ghost cells shown in dashed boxes.

4.3.2 Error Estimation

A straightforward estimation of local truncation error can be performed by employing Richardson extrapolation [32]. The fine grid is first taken down to the coarse level and a time-step integration is performed. This result is then compared to the result of integrating the fine grid first and then coarsening. In case of smooth solutions, the truncation error of the scheme would be directly proportional to the difference of the above mentioned results. Here, the global and local truncation error

remains the same [30]. Structures which were missed during the averaging process of grid coarsening will be identified due to this additional measure.

4.3.3 Grid Generation

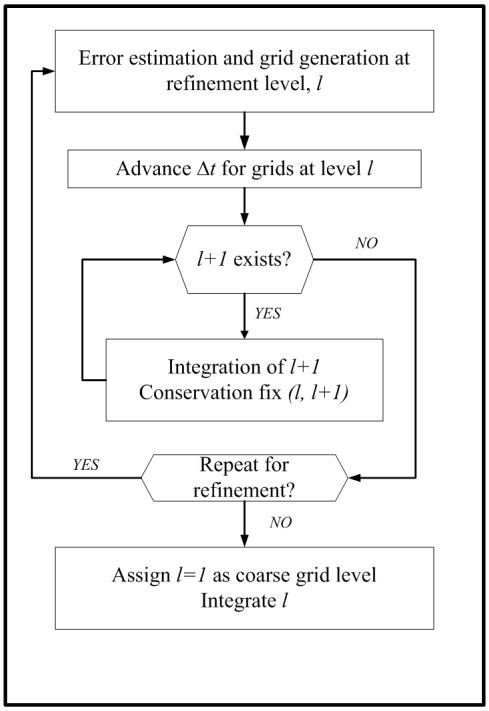

Figure 4.5. Flowchart of the grid integration cycle.

Using Richardson extrapolation as a refinement technique, the cells to be refined can now be flagged. It is necessary to establish a buffer zone during regridding. In order to generate new refined grids, a clustering algorithm is now employed. This algorithm would aid in generating successively smaller grids until the ratio between all the cells in the refined grid and the ones which were flagged for refinement reaches an optimum threshold value. The selection of this threshold value is critical for the algorithmic efficiency. The higher the threshold value, the fewer the unnecessary

points with more grid clusters, which increases data transfer and computational time. The threshold value for the simulation was selected to be 0.9 as this does not increase unflagged points relative to flagged sections. Bell et al. [93] proposed a technique of counting the number of flagged cells along every row and column, their sum being called *signatures*. The clustering algorithm is executed locally on G_l^x, and the result of G_{l+1}^x is passed globally in order to obtain $G_{l+1} = \bigcup_x G_{l+1}^x$. Figure 4.5 illustrates a typical grid integration cycle. The mesh refinement factor is denoted by r, and level l refers to the number of refinements with the coarsest level at 1.

4.3.4 Partitioning

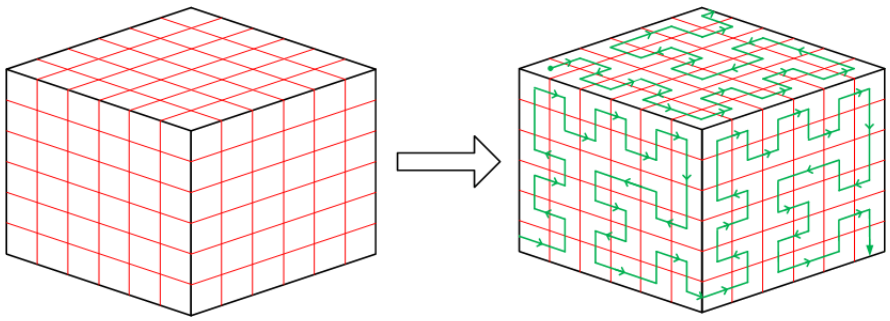

Figure 4.6. Three-dimensional representation of the computational domain and a level 2 Peano–Hilbert mapping on the domain.

Overall efficiency of the algorithm is greatly influenced by the choice of run-time partitioning strategy as it is responsible for creating a load-balanced domain decomposition strategy, with minimal data synchronization. The use of space-filling curves has been instrumental in the success of many mesh refinement strategies [94]. A space-filling curve is described as a continuous, injective and surjective function that can map a line to a multidimensional domain. This mapping can be done via a recursive division of a parent domain to multiple child sub-domains. The final result,

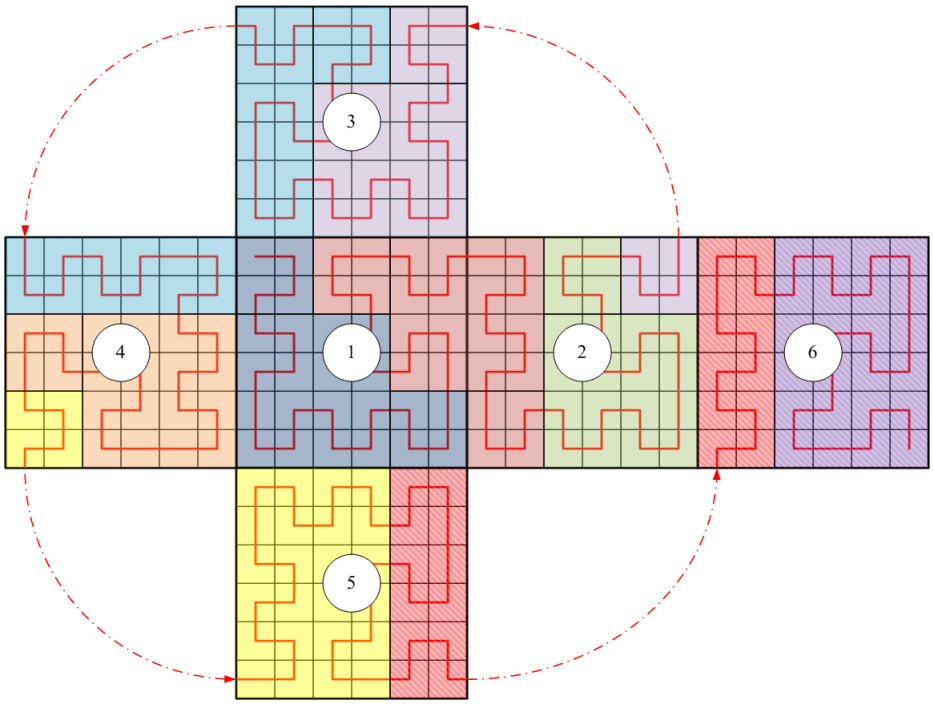

Figure 4.7. A level 2 Peano–Hilbert mapping on a three-dimensional domain on nine processors [3].

shown in Fig. 4.6, is obtained by connecting each sub-domain in a specific pattern. A comprehensive description of various types of space filling curves has been discussed in detail by Sagan [33]. A hybrid space-filling curve combining Hilbert and Peano curves was introduced by Dennis [3], who called it Peano–Hilbert mapping. Consider a three-dimensional domain with the size of $P \times P \times P$ as shown in Fig. 4.6. The Peano–Hilbert mapping then consists of a Hilbert curve for $P = 2^n$ and a Peano curve for $P = 3^m$, as $P = 2^n 3^m$ where n and m are integers referring to the recursive levels of the curves [33]. As shown on the computational domain, the start and end of the space-filling curve must be aligned to the neighboring faces in such a manner that a single, continuous line can meander along the entire domain. This is evident in Fig. 4.7, where the domain is unwrapped for easy comprehension. A detailed

analysis and speedup comparison between traditional partitioning and partitioning using space-filling curves can be found in [3].

The rationale behind using space-filling curves is that an optimal path is traced on the multidimensional space which can then be mapped in a linear fashion. This minimizes the communication overhead and can be easily load balanced. Figure 4.7 also illustrates the relative ease in dividing the domain among nine parallel processors as illustrated by different colors.

4.4 CLAWPACK Integration

Leveque developed a software package called CLAWPACK (Conservation Laws Package) which implemented finite volume numerical methods useful for solving Riemann problems [69]. The algorithms in the package can be applied to a wide range of hyperbolic systems by providing the appropriate Riemann solver along with initial data and boundary conditions. The algorithms have been extensively validated for multi–dimensional wave propagation problems and have a high order of accuracy [95]. For reactive flow problems, Roe second–order scheme with higher-order MUSCL construction and van-Albada limiter with second–order Runge–Kutta time stepping were used. A chapter dedicated to understanding the numerical methods along will be included in the final dissertation.

4.5 Numerical Validation

The numerical results for two–dimensional non–reactive forward facing step and reactive unstable detonation displaying cellular structure are given here. The main objectives of these studies were to determine the accuracy of the methods, scalability of the framework with complex flow phenomena, evaluate the partitioning and

communication overhead and to asses the dynamic load balancing. This dissertation contains a comprehensive list of tests to illustrate the effectiveness of the designed framework to solve a wide range of problems.

4.5.1 Two-Dimensional Forward–Step Problem

The test problem of a Mach 3 inviscid flow past a confined step was simulated for the two-dimensional demonstration of AMR framework. Emery introduced this problem as a test case for comparison of finite difference schemes and Woodward provided a detailed comparison of many methods with this test case [96]. More recently, this problem was solved as a test case using an adaptive mesh refinement code called **FLASH** [88], which is extensively used for astrophysical applications. For purposes of comparison, this test was executed with the same parameters as employed in the **FLASH** simulation.

The test problem is to simulate Mach 3 supersonic flow over a forward facing step. The computational domain is 3 length units long and 1 length unit high. The step is 0.2 length units high and is located 0.6 length units from the left end of the domain. The boundary conditions are as follows: the left end is an inflow, the right end is an outflow (since the flow is supersonic, the outflow conditions have no effect on the flow) and top and bottom are reflecting walls. The inflow is maintained with a constant specific heat ratio of $\gamma = 1.4$, which results in the density as 1.4, pressure as 1.0 and velocity as 3.0. The domain has a coarse mesh of 120×40 with 5 levels of refinement, with refinement factors $r_{1,2,3,4,5} = 2$ corresponding to 3840×1280 fine mesh at the highest level of refinement. The time evolution of the flow is shown in Fig. 4.5.1. The solution can be qualitatively compared to the results in [96, 88]. Using a second-order Roe scheme with MUSCL interpolation, the shock structures are found to be well-defined and there is very little numerical noise due to the corner in the

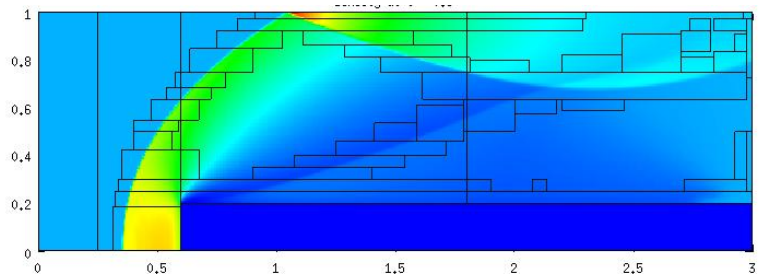

(a)

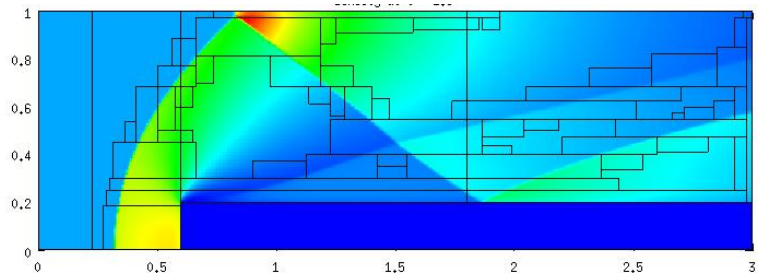

(b)

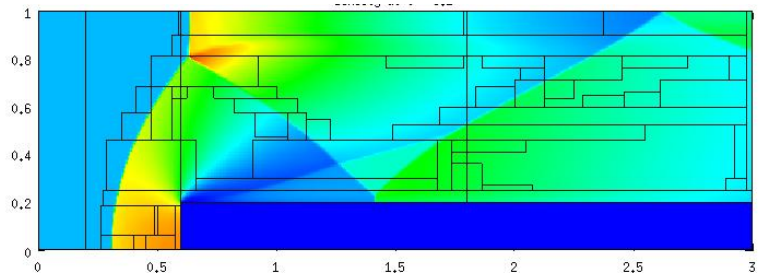

(c)

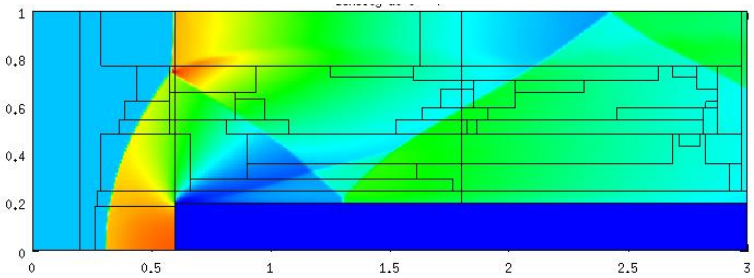

(d)

Figure 4.8. Time evolution of density in pseudo—color for flow over a confined forward–facing step, a) t = 0.8 b) t = 1.6 c) t = 3.2 d) t =4.0. The boxes indicate the zones being refined at the next level.

step. Woodward's results using the MUSCL approach exhibited some numerical noise due to uniform fine grids in regions of minimal flow development, but they do not

Table 4.1. Computational cost breakdown in percentage of total time: two-dimensional Mach 3.0 flow over a confined step–16 processors

Categories	Level 5
Integration	33.34
Grid Operations	18.45
Updates	40.63
Load Balancer	2.99
Data and Memory Management	4.59

appear in the present AMR visualizations even with grid coarsening. Table 4.1 shows a computational cost comparison for 16 processors. The computational cost can be grouped under the following categories: integration time (PDE and source terms), grid operations (grid initialization and boundary value operations), updates (refining grids and conservative correction), load balancing operations and data management (memory overhead, output, read data, checkpoint etc.). Not surprisingly, a majority of computational time was used for cell updates which include flagging operations, grid refinement and correction of conservation because of computationally-intensive 5 levels of refinement. Using 16 processors and adaptive mesh refinement, the total computation time was reduced to 1385.4 seconds compared to a 16 processor-uniform fine mesh computation time of 98346.32 seconds.

CHAPTER 5

DETONATIONS WITH SIMPLIFIED CHEMICAL KINETICS

This chapter is devoted to the understanding of pulsating detonations obtained from simulations using inviscid Euler equations with single–step Arrhenius kinetics derived in Chapters 2, using the numerical techniques explained in 3. Both 1–D and 2–D results are analyzed below. Section 5.1 describes the numerical results for one–dimensional simulations and a brief discussion about bifurcation theory and the period–doubling phenomenon of the longitudinal waves in one–dimensional detonations is provided. Here, we attempt to discover the mechanism forcing the longitudinal oscillations from regular periods to chaotic pulses. Section 5.2 extends the same numerical experiments to two–dimensional simulations to provide detailed visualizations of the detonation front and also captures the transverse wave shock pressures at longitudinally stable and unstable regimes to understand the effect of transverse waves on the shock front. Section 5.4 is a condensed version of the three–dimensional linear limit cycle stability analysis of transverse wave instabilities, for a longitudinally stable set of parameters as discussed by Massa et al.[51].

5.1 One–Dimensional Detonations

In this section, the 1D calculations with simplified kinetics are described. The significant parameters of interest are the reduced activation energy E_0^*, heat release Q_0, the overdrive parameter f and the ratio of specific heats γ. For this study, the parameters $\gamma = 1.2$ and $Q_0 = 50.0$, which are typical for most gaseous combustion mechanisms, are held constant. In the first part of the study, E_0^* is held constant

and the overdrive parameter is varied. In the second part, f is held constant and the activation energy E_0^* is varied.

The domain for this problem should be sufficiently big to account for the disturbances to propagate upstream to the discontinuity. Hwang et al.[97] provided a detailed discussion regarding the minimal computational domain size so that there will not be any influence on the detonation wave due to the boundary conditions. Based on their work, a domain size of 200 was chosen and and and the shock frame was selected as described by Fig. 2.1 in Sec. 2.1. A wave based on the ZND calculation was stabilized at the far right of the domain. Normal inflow and outflow boundary conditions were applied. The von Neumann pressures were plotted over time in a similar fashion as in other approaches in the literature [13, 97].

5.1.1 Varying The Overdrive Parameter f

In this study, the parameters held constant are $Q_0 = 50.00$, $E_0^* = 50.00$ and $\gamma = 1.2$ and the overdrive parameter f is varied from 1.1 to 1.8. It should be noted that the higher the overdrive the more stable the reaction. The computational domain was set to $200L_{1/2}$, with a base grid of 2000×1 and two refinement levels with refinement factors $r_f =$ [42]. This corresponds to a grid resolution of $80Pts/L_{1/2}$.

Figure 5.1 shows the temporal histories of the von Neumann shock pressure for overdrive parameters $f = 1.80 - 1.40$ and Fig. 5.2 for $f = 1.36 - 1.10$. Bourlioux et al.[13] obtained the limit of absolute stability as $f_0^* = 1.73$ in their analysis. In Fig. 5.1, at $f = 1.80$, the solution is longitudinally stable after the initial perturbation. Moving up to the limit of stability, the oscillations gradually increase with rising overdrive and at the limit of stability, it can be observed that the solution has a steady oscillation which does not dampen with time. All solutions beyond this limit of stability are now considered longitudinally unstable.

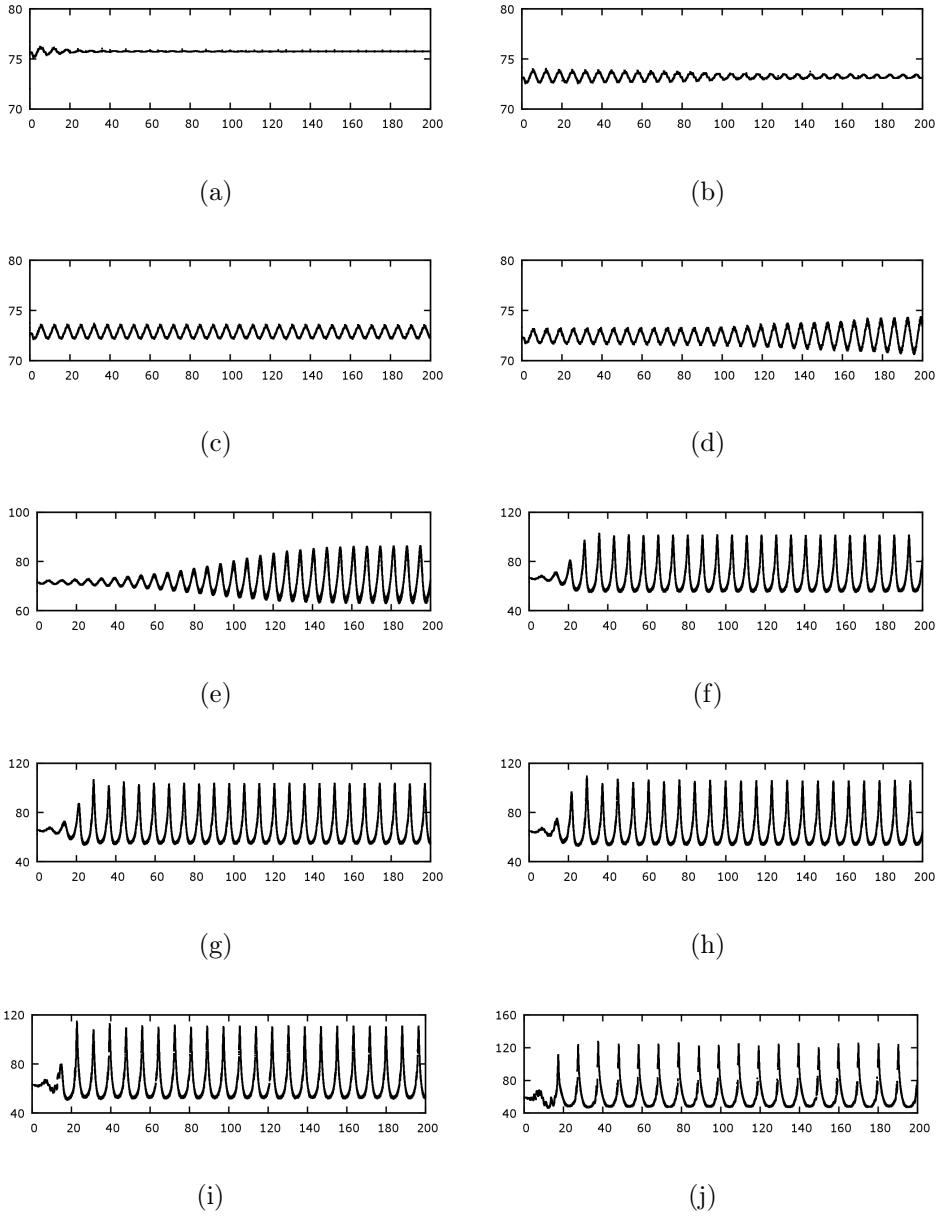

Figure 5.1. Von Neumann shock pressure histories for overdrive parameters $f = 1.80 - 1.40$, $CFL \approx 0.95$; (a) f = 1.8 (b) f = 1.74 (c) f = 1.73 (d) f = 1.72 (e) f = 1.70 (f) f = 1.58 (g) f = 1.56 (h) f = 1.54 (i) f = 1.50 (j) f = 1.40.

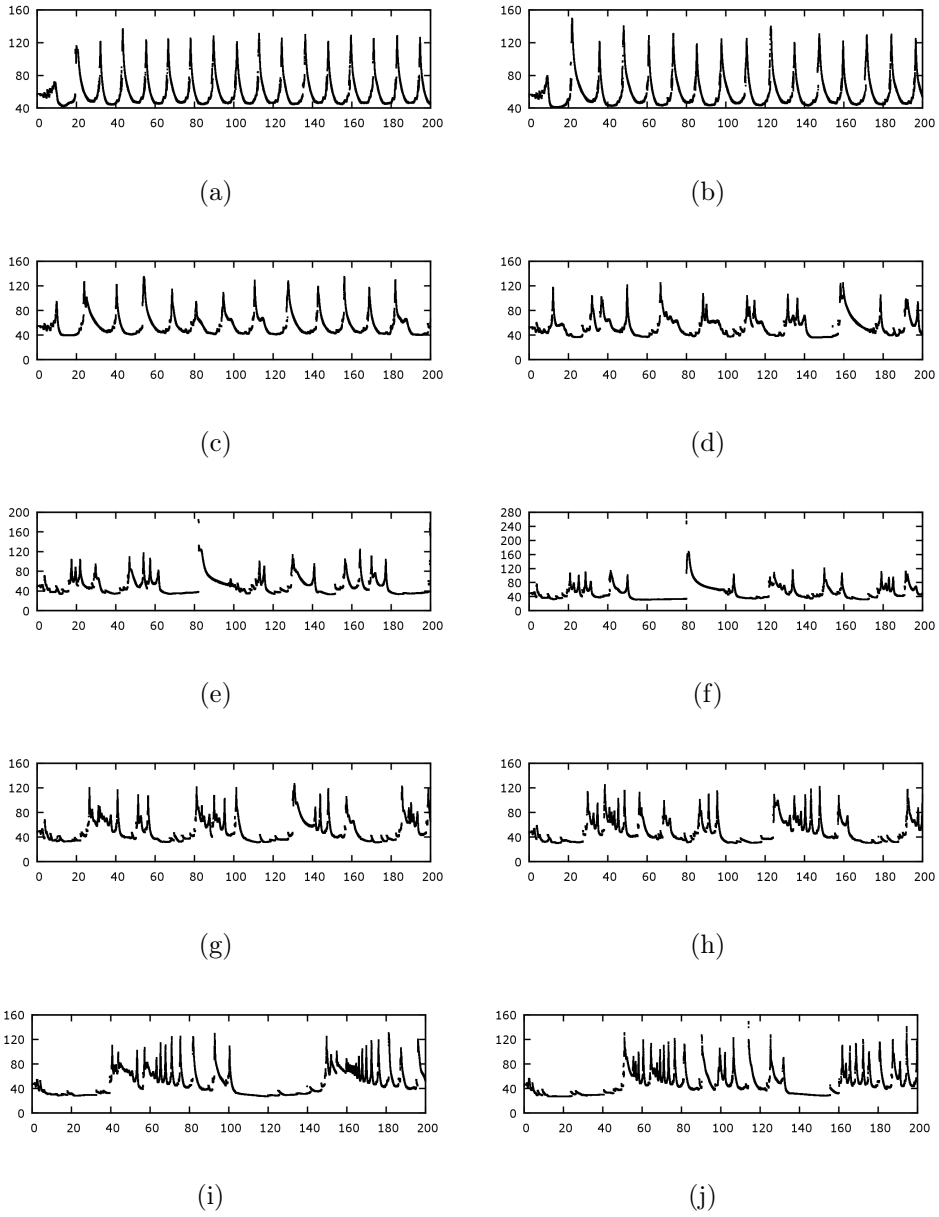

Figure 5.2. Von Neumann shock pressure histories for overdrive parameters $f = 1.36 - 1.10$, $CFL \approx 0.95$; (a) f = 1.36 (b) f = 1.34 (c) f = 1.30 (d) f = 1.25 (e) f = 1.20 (f) f = 1.18 (g) f = 1.16 (h) f = 1.14 (i) f = 1.12 (j) f = 1.10.

The period doubling phenomenon can be observed in Fig. 5.2 at $f = 1.36$ when two distinct peaks are observable. Lowering the overdrive further, shows multiple bifurcations, till the overdrive reaches $f = 1.30$, beyond which the solution is chaotic. Zumbrun characterizes this transition from the stable solution to a time–periodic galloping instability as a Poincaré–Hopf bifurcation [22]. The simulations here qualitatively match Bourlioux's results [13], and the peaks look highly resolved. Moreover, in Bourlioux's and Majda's work, the bifurcation phenomenon was not observable as their grid resolution $20Pts/L_{1/2}$ was insufficient to overcome the discretization errors.

Simulations below the overdrive of $f < 1.30$ are highly unstable and exhibit chaotic behavior. All results below $f = 1.10$ do not converge properly even with high grid resolutions of $640Pts/L_{1/2}$. Since there is not much literature available for longitudinal instabilities with varying overdrives, the author concludes that the second–order numerical scheme must be contributing to convergence failure. It is possible that some higher–order, low–dissipative compact schemes (with spectral-like resolution) can offer better results for the highly unstable regimes.

5.1.2 Varying The Reduced Activation Energy E_0^*

In this study, the reduced activation energy is varied from $E = 24.00 - 30.00$ with $Q_0 = 50.0$, $\gamma = 1.2$ and $f = 1.001$. The overdrive factor was kept slightly over 1 to ensure the ZND solver stays stable and does not calculate $M > 1.0$ in the burned gas. The variation of activation energy has been an active topic of research as a slight variation in activation energy of $E_0^* \approx 0.01$ induces high longitudinal instabilities. Hence for this study, 40 test cases were solved, using activation energies not studied prior to this research.

The computational setup was identical to the previous setup with the exception of the refinement: for this study, 3 refinement levels of $r_f = [442]$ are used to obtain a

grid resolution of $320 Pts/L_{1/2}$. This is an unprecedented level of grid resolution: the finest resolution published till now was $128 Pts/L_{1/2}$ [24]. There is a reasoning behind using a higher resolution and small changes in activation energy; certain phenomena are captured for the first time, which can be instrumental in explaining the transition to chaotic behavior. Figures 5.3 and 5.4 show the temporal histories of the effect of reduced activation energy on the von Neumann shock profile.

For activation energies below $E_0^* < 25.26$, the longitudinal oscillation due to the initial perturbation dampens out with time evolution and the detonation is stable. Sharpe provided much valuable insight into the stability boundary and using linear analysis, predicted the stability boundary to be around $E_0^* = 25.26$ [98], which is in good agreement with the present study, as observable Fig. 5.3 for $E_0^* = 25.26$. Sharpe also presented a set of computational requirements to observe long–term evolution of detonations, wherein the simulation has to run for many seconds before the correct non–linear behavior is observed [98].

By a methodical increase of activation energy from the stability limit, it is observed that the regular oscillatory behavior of the longitudinal instability morphs from a single–mode oscillation to a double–mode oscillation, in a process which is called "period–doubling" [23]. The peaks of the von Neumann pressures are used to "count" the modes. The period–doubling process always occurs in 2^n factors. Visually, from Fig. 5.3 and 5.4, one can acquire the double–modes, $n = 1$ for activation energy $E_0^* = 27.40$, quad–modes $n = 2$ at $E_0^* = 27.82$ and octa–modes $n = 3$ at $E_0^* = 27.92$. As the activation energy increases further to $E_0^* = 28.30$, the normal modes collapse and coalesce to recombine to a very strong three–peak periodic system and the process repeats itself with increasing activation energies, to a point where the pressure histories look very random at $E_0^* = 30.00$.

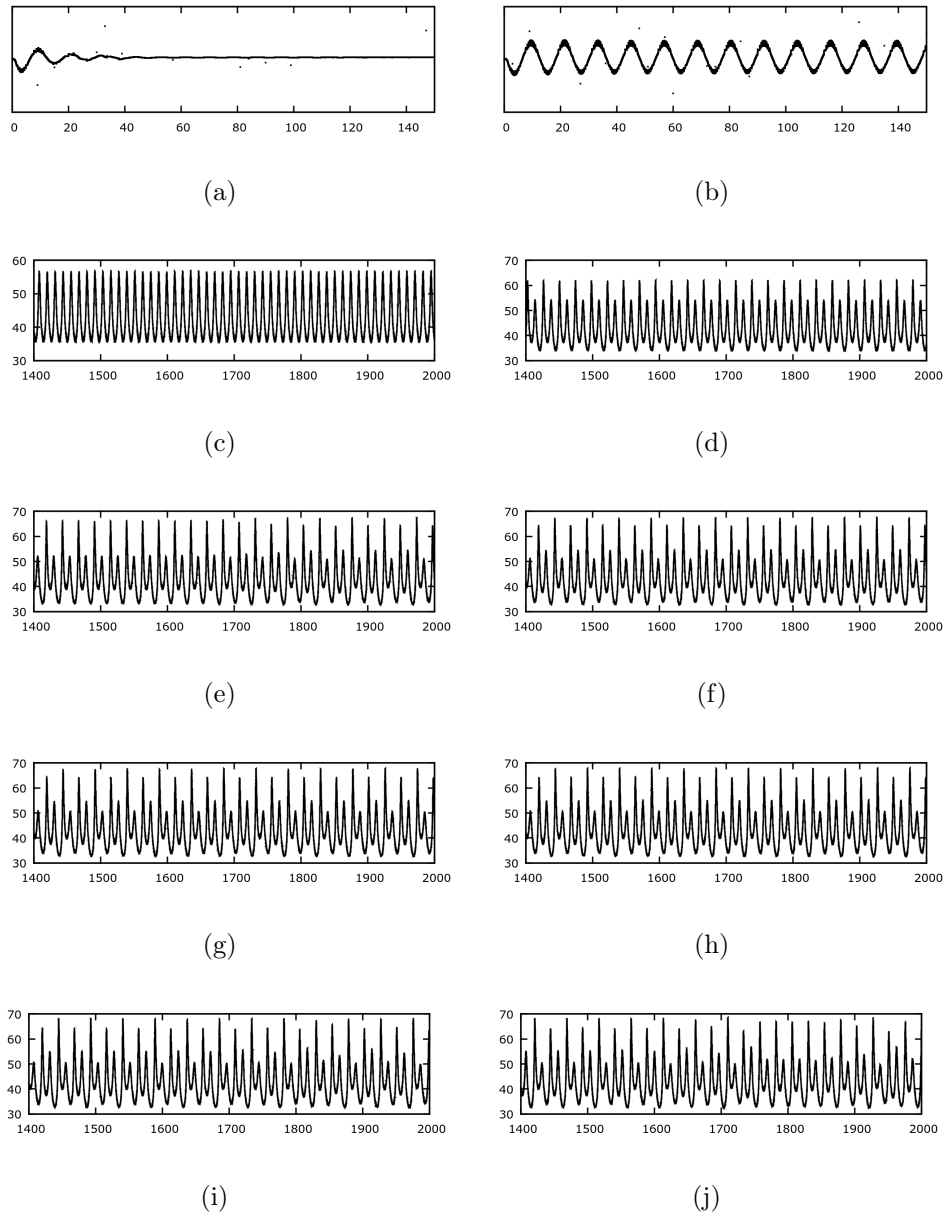

Figure 5.3. Von Neumann shock pressure histories for activation energy parameters $E_0^* = 24.00 - 27.90$, $CFL \approx 0.95$; (a) E=24.00 (b) E=25.26 (c) E=27.00 (d) E=27.40 (e) E=27.80 (f) E=27.82 (g) E=27.84 (h) E=27.86 (i) E=27.88 (j) E=27.90.

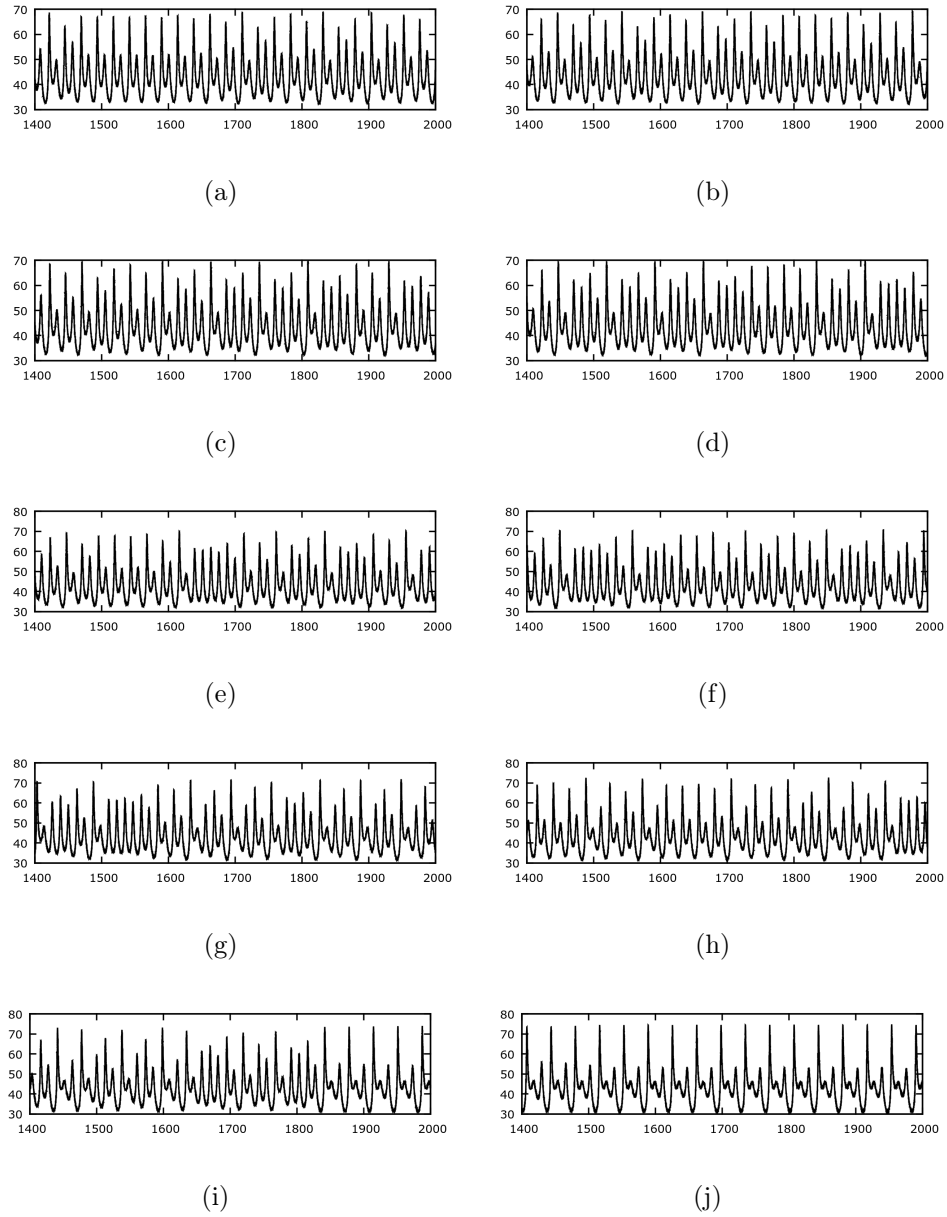

Figure 5.4. Von Neumann shock pressure histories for activation energy parameters $E_0^* = 27.92 - 28.25$, $CFL \approx 0.95$; (a) E=27.92 (b) E=27.94 (c) E=27.96 (d) E=27.98 (e) E=28.00 (f) E=28.05 (g) E=28.10 (h) E=28.15 (i) E=28.20 (j) E=28.25.

The use of very high grid resolutions pays off in an important aspect: the higher grid resolutions enabled peak resolutions of higher accuracies, which is vital to capture modes beyond $n = 3$. Even with the use of a second–order algorithm, the convergence for an increase of activation energy of the order of $E_0^* \approx 0.01$ is good and the discretization errors do not affect the accuracy of the solution. However, it becomes difficult to visually discern modes beyond $n = 3$ and a suitable numerical tool is required. The use of power spectral density (PSD) is an option, since it gives the variance of a time series with frequency. Sharpe provides other statistical techniques which could be used to isolate the peaks from time–varying data [99]. Since the development of a PSD method is beyond the scope of this work, it is suggested as a part of future work.

5.1.3 Formation Of Multiple Identical Peak Pressures

One of the phenomena which was observed in this study on period–doubling in both overdrive parameter f and activation energy E_0^*, was the formation of a cluster of identical peaks of von Neumann pressure histories preceding the destruction of periodic oscillations and introducing randomness. Figure 5.5 illustrates this point for two cases: one with overdrive parameter at $f = 1.10$ and the other with activation energy $E_0^* = 28.20$.

The highlighted peaks have appeared for all the simulations with activation energy $E_0^* > 28.20$ at some point in their pressure history, and it was observed that immediately after their formation, the period–doubling phenomenon halts. This is a peculiar phenomenon not reported before in literature and it is the author's belief that this would be first time this was noticed. More research in this particular topic is required, but it is possible that this represents the coalescence stage of the normal modes.

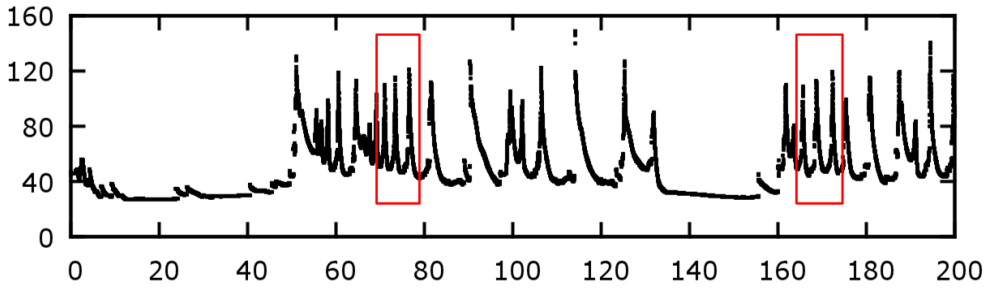

(a)

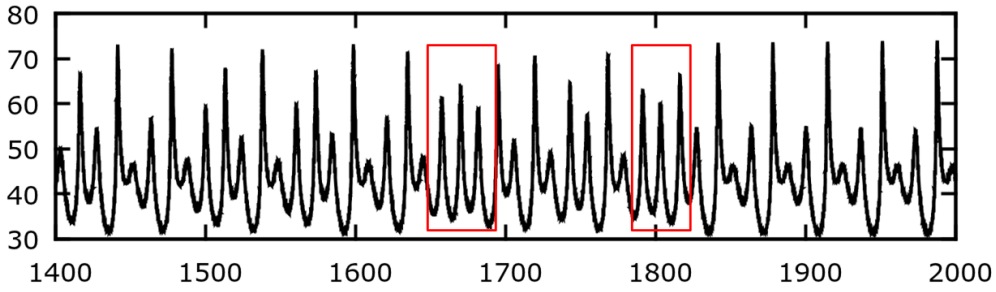

(b)

Figure 5.5. Formation of identical peaks preceding the destruction of the period–doubling process for a) $f = 1.10$ and b) $E_0^* = 28.20$. $CFL \approx 0.95$.

5.2 Two–Dimensional Simulations

In this section, the unstable 2D detonations with single–step chemistry are simulated. The goal is to determine the difference between one-dimensional and multi–dimensional bifurcations. The unstable detonations were simulated for conditions $\gamma = 1.2$, $E_0^* = 50.00$, $Q_0 = 50.00$ and $f = 1.58$, which is weakly unstable, and for $\gamma = 1.2$, $E_0^* = 50.00$, $Q_0 = 50.00$ and $f = 1.10$ which is strongly unstable. The same numerical techniques employed for the previous simulations were use for this study too.

5.2.1 Weakly Unstable Detonations

The weakly unstable case simulated in one–dimensional study was extended to two–dimensions. A rectangular domain of 20×10 half–reaction lengths and the velocities in X direction were shifted by the CJ detonation velocity. Regular inflow and outflow boundary conditions were initialized on the right and left sides and reflective conditions in the top and bottom sides of the domain. The initial state is a ZND wave held at $X = 12$ and a pressure increase of 15% was initiated at $[11.45, 11.95] \times [4.85, 5.25]$, a technique to induce perturbation proposed by Oran et al.[17]. Two refinement levels with refinement factors $r_f = [44]$ have been used, leading to a grid density of $160 Pts/L_{1/2}$. Figure 5.6 shows the evolution of the density gradient $\bar{\rho}$ for a weakly unstable detonation wave. The simulation plots are populated after the perturbation has set in, so the first 20 time units are not shown.

The simulation clearly shows the unstable nature of the detonation. While the longitudinal instability is barely visible (from $t = 30$ to $t = 120$, the forward motion of the wavefront is seen), the transverse instability is more predominant than the longitudinal instability for the given conditions. The formation of triple–points where the transverse waves come into contact with the shock front are also observed.

5.2.2 Strongly Unstable Detonations

A strongly unstable detonation is studied in this test. All the parameters and conditions were kept the same as for the weakly unstable case with the exception of the overdrive parameter, $f = 1.10$. Figure 5.7 shows the time evolution of the density gradient for this case.

From the figure, the most obvious difference between a strong and weak unstable detonation, is the density gradient: stronger density fluctuations are seen for strongly unstable waves. The second is that even thought the transverse waves are stronger

as evidenced by the faster pulsation in the vertical direction, the longitudinal waves quickly engulf the transverse instabilities, and the front 'gallops' ahead in space. For the same time–step in both cases, the front in the strongly unstable case has galloped out of the computational domain.

In an attempt to visualize the effect of the longitudinal instabilities on strongly unstable detonations, a few test cases with varying activation energies in the strongly unstable regime were conducted. Unfortunately, to capture the longitudinal pulsations after at least 800 time–steps, a domain size of at least 1000 half–reaction lengths in the X direction was required. To keep the computational budget low, the Y direction had to be restricted at 10 half–reaction lengths. Since the results are inconclusive due to poor visualization, the results are attached in the appendix and not thoroughly discussed here. It is evident to simulate detonations with fast gallop, an innovative AMR approach such as doubling the domain every few time–steps or calculating and negating the x velocities at each iteration is required. Such approaches are currently out of scope for this work and are reserved for the future work section.

5.3 Transverse Wave Instabilities For Weakly Unstable Detonations

One of the important questions is whether the transverse instabilities in multi–dimesional, longitudinally stable detonations undergo a period–doubling phenomenon similar to longitudinal oscillations in one–dimensional detonations. Section 5.4 discusses this question by performing a three–dimensional Floquet linear stability analysis on the flow where the changes in solution are represented by the eigenvalues of the Poincaré map [50] using the parameters $E = 20.0$, $Q = 38.6$, $f = 1.01$ and $\gamma = 1.2$.

In this section, using the same parameters, the one–dimensional von Neumann pressure history is provided and a two–dimensional simulation is conducted to capture the transverse wave pressures. Figure 5.3 illustrates the von Neumann pressure his-

tories for 1D and 2D simulations. The one–dimensional simulation gives longitudinal wave history, and the plot shows a longitudinally stable wave. The two–dimensional simulation on the other hand captures the transverse wave instability and from the plot, it is evident that the transverse wave is in the unstable regime with a single mode oscillation.

As the Floquet analysis in Sec. 5.4 would also prove, there is a strong possibility for the transverse waves to undergo period-doubling phenomena similar to the longitudinal waves. As it stands, the scope of this research was limited to two–dimensions but efforts are underway to expand the framework to three–dimensions to conduct a thorough transverse instability analysis.

5.4 Floquet Analysis Of Transverse Wave Instabilities

This section describes the analysis of the stability of limit cycles in three-dimensions. The analysis is restricted to transverse wave instability, thus activation energies below the longitudinal instability limit. The global kinetic parameters considered in this analysis are $E = 20.0$, $Q = 38.6$ and $\gamma = 1.2$.

The limit cycle stability is investigated by performing a three–dimensional Floquet stability analysis of the time-periodic flow. The Floquet analysis seeks eigenvalues of the linearized Poincaré map $\mathcal{E}'$ representing changes in the solution over a periodic cycle [100]. Romick et al.[101] found that the diffusive terms stabilize the limit cycle solutions in one dimensional waves, therefore the present unforced analysis uses the inviscid Euler equations.

5.4.1 Base flow

The time periodic base-flow is obtained by setting up a recursive procedure to determine not only the flow variables $U\left(x, y, z, t\right),\ U \equiv [\rho, \rho\vec{u}, E_t, \rho\lambda]^T$, but also the

detonation velocity D and the fundamental period T_f. The search for D is necessary in this context because free detonations are not anchored. A time periodic solution is evaluated at fixed locations by an observer moving with velocity D with respect to the pre–shock gas (i.e., in the laboratory frame). Therefore, D is defined as the pre–shock inflow speed such that the position of the lead shock is time-periodic in laboratory frame. The value of D is in general different from the ZND analogue D_0 because, although the detonations under investigation are longitudinally stable, the non-linear limit cycle oscillations change the mean shock velocity.

The symbol $\mathcal{E}(U, \Delta t, W)$ denotes the operator that yields the solution of the Euler equations starting with initial conditions at $t = t_1$ and integrated for a time interval Δt by an observer moving with velocity W in the laboratory frame. The condition of closed periodic orbits is imposed, thus searching for U, T_f, D such that

$$\mathcal{E}(U, T_f, D) = U. \tag{5.1a}$$

$$x_{1/2}(T_f) = x_{1/2}(0) = 1, \tag{5.1b}$$

where,

$$x_{1/2}(t) \equiv (x|\bar{\lambda}(x,t) = 0.5), \tag{5.2}$$

and

$$\bar{\lambda}(x,t) = \frac{\iint \lambda(x,y,z,t)\, \mathrm{d}y\, \mathrm{d}z}{L_y L_z}. \tag{5.3}$$

The system in 5.1 is solved with the fixed point iteration

$$U^{n+1,m} = \mathcal{E}\left(U^n, T_f^{n+1,m}, D^{n+1,m}\right), \tag{5.4}$$

where $T_f^{n+1,m}$ is evaluated by minimizing the norm of the error between consecutive iterations, i.e., requiring

$$\frac{\partial}{\partial T_f}\left\|U^{n+1,m} - \mathcal{E}\left(U^n, T_f, D^{n+1,m}\right)\right\| = 0. \tag{5.5}$$

The index m indicates a secant method sub-iteration (within the fixed point iteration) where the value of D is updated to satisfy equation (5.1b) within a tolerance of 1×10^{-5}. In fact, it is found that the computationally less expensive iteration

$$U^{n+1} = \mathcal{E}\left(U^n, T_f^{n+1}, D^n\right)$$

$$D^{n+1} = D^n + \frac{1 - x_{1/2}(T_f^{n+1})}{T_f^{n+1}}$$

does not converge for the case under study.

The non-linear mapping $\mathcal{E}$ is evaluated by using a WENO-Z flow solver to integrate the Euler equations between 0 and T_f. The use of the secant method requires multiple flow evaluations per each fixed point iteration leading to a significant increase in computer time.

Dou et al.[102] find that the solution to the three-dimensional Euler equations in square channels is non-periodic. It will be demonstrated by the present Floquet analysis that this is a consequence of the initial solution being out of the attraction manifold of the limit cycle, not of the instability of the same. It was found to be beneficial for converging towards a limit cycle, to start the base flow analysis with a Navier-Stokes simulation: a low Reynolds number leads to attraction to the limit cycle for any initial perturbations of the ZND solution. Therefore, the base flow solution procedure is initiated by integrating the Navier-Stokes equations for $40 \times T_f$ without updating T_f and D. Results of the fixed point analysis are shown in Fig. 5.9 and demonstrate a rather quick convergence of the Euler solution with the number of iterations, i.e., $n \equiv t/T_f$.

Figure 5.9(d) shows that a fundamental period corresponds to four almost identical sinusoidal variations in $x_{1/2}$. The rationale is that T_f includes four triple point

collisions and their motion within a period is illustrated in Fig. 5.10, where pressure iso–surfaces are drawn for $p = 0.8\ p_{\max}$ and for a set of time steps covering T_f. Note that different colors represent different times on the same figure. Four collisions are necessary to bring the system back to the initial state. The boomerang shaped profiles marked by arrows are the collision planes, the other iso–surfaces indicate the movement of the high pressure gas following the explosive collisions. Pressure traces evolve with time by moving in both counter and clock-wise directions starting from the dark-blue profiles and returning back to the original position in dark red. Two triple points travel away from each collision plane, thus orbiting in opposite directions. Going back to Fig. 5.9, part (d) shows that the four collisions in the fundamental period are similar but not identical: the second and third one appear to be slightly stronger than the first and fourth, leading to a marginally larger peak in $x_{1/2}$ in the second and third parts of the sequence.

5.4.1.1 Floquet stability

The stability of the limit cycles is analyzed by considering the evolution of the flow perturbation as:

$$U'^{n+1,m} = \mathcal{E}\left(U_{base} + U'^{n}, T_f, D^{n+1,m}\right) - U_{base}, \tag{5.6}$$

where T_f and U_{base} are fixed to the values found in §5.4.1, while D^{n+1} is found by imposing equation (5.1b). Secant method iterations (m) with tolerance 1×10^{-5} are performed to iterate the value of D^{n+1}. The DMD analysis of the snapshots series $v_n = Q'\left(U^n\right)$ leads to the approximation of the eigenvalues of linearized map $\mathcal{E}'$, which corresponds to the monodromy matrix (a first order recurrence linear mapping, see Iooss and Andelmeyer[103]). Note that equation (5.6) is shown using the conservative variables perturbations U' because the governing equations are solved in terms of U,

but the DMD reduction analysis is performed in terms of Q' defined in equation (5.7) as

$$Q' \equiv \left[\vec{u}', \frac{p'}{\sqrt{\gamma \bar{p} \bar{\rho}}}, \frac{s'}{R} \sqrt{\frac{(\gamma - 1)\, \bar{p}}{\bar{\rho} \gamma}}, \sqrt{Q} \lambda' \right], \tag{5.7}$$

This ensures that the coherence physically represents the energy of the modes.

The stability analysis is initialized by perturbing the base-flow with a uniform random distribution

$$U'^0 = \epsilon U_0 (r - 1/2), \tag{5.8}$$

where ϵ is a small parameter, U_0 is the uniform pre–shock state, and r is a random number between 0 and 1. The perturbation evolution for $\epsilon = 1 \times 10^{-1}$ is presented in Fig. 5.11 in terms of D^n and the deviation from the base solution U_{base}. Figure 5.11(b) shows that a reduction of four orders of magnitude in the norm of the perturbation is obtained within 30 Floquet cycles. This consideration leads to conjecturing a limit on the number of snapshots that can be included in the DMD analysis, because small perturbations are affected by round-off error in the finite difference WENO scheme. Past studies on Floquet stability of incompressible flows[100] have shown that dominant modes (i.e., the least stable ones) converge quickly, within ten iterations. A similar conclusion holds for the detonation limit cycles as shown below.

The eigenvalues of $\mathcal{E}'$ are the Floquet multipliers μ_k, and the limit cycles are stable for $|\mu_k| \leq 1$. Global wave-like perturbations can be expressed

$$U'_k = \tilde{U}_k \left(x, y, z, t \right) \exp \left(\lambda_k t \right), \tag{5.9}$$

where $\tilde{U}_k$ is T_f periodic and λ_k is called the Floquet exponent. Such a temporal eigenvalue is evaluated as $\lambda_k \equiv \log \left(\mu_k \right) / T_f$. In the present study, the Floquet exponents are scaled by the fundamental wave-frequency $\omega_f \equiv 2\pi / T_f \approx 1.82 \sqrt{p_0 / \rho_0} / L_{1/2}$, leading to

$$\lambda_k / \omega_f = \frac{\log \left(\mu_k \right)}{2\pi}. \tag{5.10}$$

The limit cycles are stable for $Re\,(\lambda_k) < 0$. Note that the global eigenfunctions found by decomposing the linearized Poincaré map into dynamic modes correspond only to an instantaneous value $\tilde{U}\,(x, y, z, t_1)$, where $t = t_1$ is the initial time of the period $[t_1, t_1 + T_f]$.

The scaled frequencies are presented in Fig. 5.12 for four cases identified by the initial perturbation to the base flow solution. All cases are obtained with different seeds in the uniform random number generator. Two cases are initialized with $\epsilon = 5 \times 10^{-2}$ and two with $\epsilon = 1 \times 10^{-1}$ to prove that the values λ_k are independent of the magnitude of the perturbation, thus represent eigenvalues of the linearized maps. Only eigenvalues with negative real parts are obtained, indicating stability of the limit cycles. Two dominant modes are converged, one with $Im\,(\lambda_k/\omega_f) \approx 0.135$, the other with $Im\,(\lambda_k/\omega_f) \approx 0.47$. The size of the symbols in Fig. 5.12 is proportional to the mode coherency. Coherency represents receptivity of the modes to random initial perturbations, thus Fig. 5.12 indicates that the low frequency mode is slightly more receptive than the high frequency analogue.

Convergence of the real and imaginary parts of the two dominant modes against the number of snapshots is shown in Fig. 5.13(a,c) (respectively) for the case marked in Fig. 5.12 with diamond symbols. The other three cases have a very similar history. Convergence of the real part within about 10% in relative error is obtained within 10 iterations; integration beyond 25 iterations yields a marginal increase in the accuracy of the results. The convergence of the imaginary part is significantly better than that of the real part.

The performance of DMD of the linearized recursion map can be improved by combining the snapshots of the four simulations. For a better explanation of the modified DMD, the notation is slightly changed from the original paper to denote the snapshots from the four simulations as v_n^m, where n is the snapshot number and

m is the simulation number. A combined snapshot matrix (cf. equation (5.11)) is obtained by alternating snapshots from the four simulations as

$$V_1^{4(N+1)} \equiv \left\{v_1^1, v_1^2, v_1^3, v_1^4, v_2^1, \ldots, v_{N+1}^4\right\}. \tag{5.11}$$

The singular value decomposition becomes $V_1^{4N} = USW^H$, and the similarity transformation leads to the reduced operator as $\tilde{S} \equiv U^H V_5^{4(N+1)} W S^{-1}$. Convergence of the combined procedure is shown in Fig. 5.13(b,d) for the real and imaginary parts of the eigenvalues, respectively. A comparison of Fig. 5.13(a) & (b) shows that the combined DMD improves significantly convergence for $n \leq 10$, but only marginally for $n \geq 25$. This outcome is explained by the reduction of the perturbation norm for $n > 25$ to a magnitude supporting large round-off cancellation error in the numerical scheme.

The combined DMD procedure is used to identify the global eigenfunctions corresponding to the two least stable eigenvalues. The eigenfunctions are shown in Figs. 5.14 and 5.15. Each panel represents an $x - z$ cut for a different y value as indicated in the caption.

Both eigenmodes are expected to be symmetric (or antisymmetric) with respect to $y = L_y/2$ and $z = L_z/2$. The slight deviation from symmetry is due to numerical error. The contours show the presence of two regions of high chemical energy fluctuations, one associated with the shock front, the second with the induction region located at $x/L_{1/2} \approx 4$.

The limit cycles of the detonations under consideration are found to be (absolutely) stable. The least stable Floquet mode is approximately subharmonic $\lambda_i \approx \omega_f/2$. This conclusion suggests that the bifurcation of limit cycles in three dimensions follows a period doubling process similar to that proven to occur in one dimension [104] and previously in this chapter. One-dimensional analyses consider waves that

are longitudinally unstable about the ZND profiles. Conversely, three dimensional analyses are usually applied to transversely unstable detonations. These waves have a lower activation energy than those analyzed in one-dimension, which justifies the stability of the limit cycles under investigation.

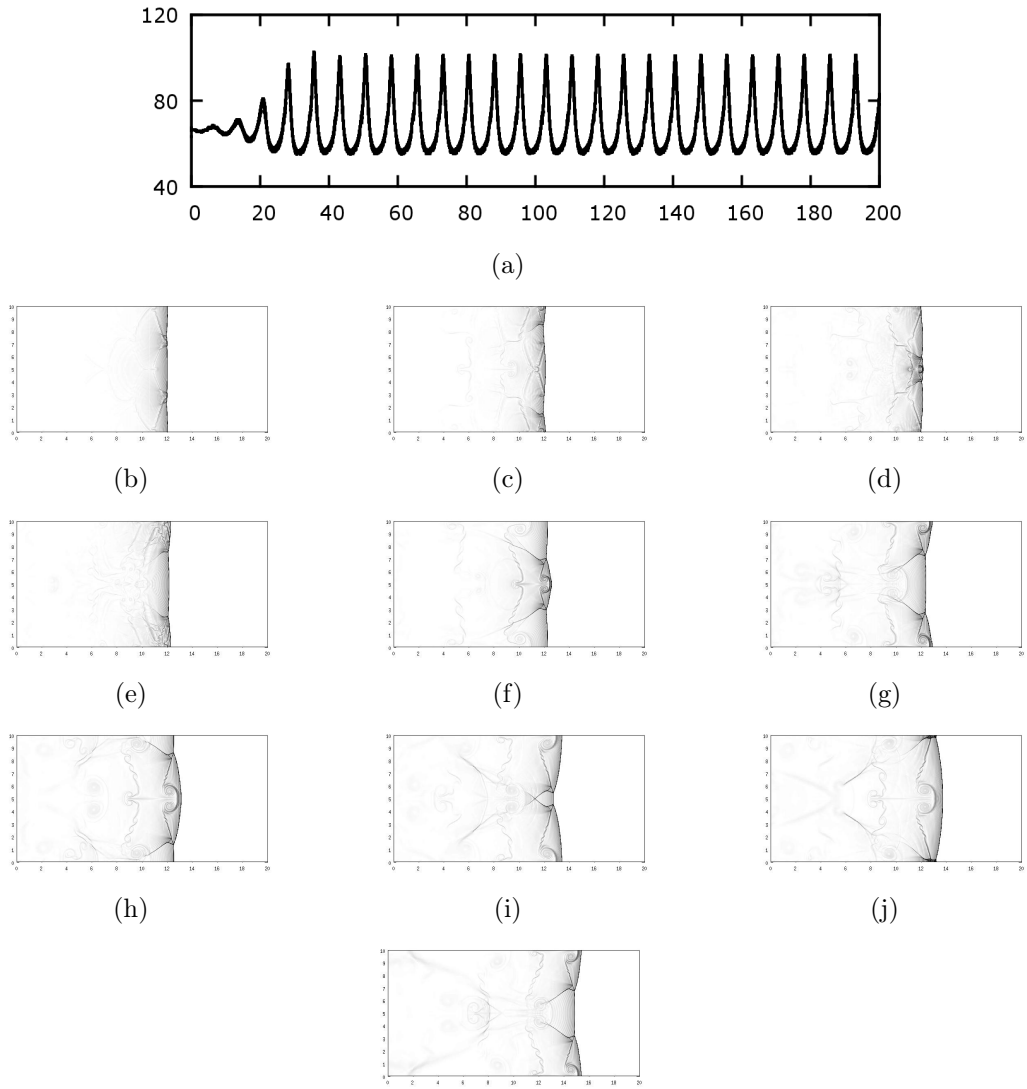

(a)

(b) (c) (d)

(e) (f) (g)

(h) (i) (j)

(k)

Figure 5.6. Density gradient plots for a weakly unstable detonation $\gamma = 1.2$, $E_0^* = 50.00$, $Q_0 = 50.00$ and $f = 1.58$, $CFL \approx 0.95$; (a) f = 1.58 (b) t = 30 (c) t = 40 (d) t = 50 (e) t = 60 (f) t = 70 (g) t = 80 (h) t = 90 (i) t = 100 (j) t = 110 (k) t = 120.

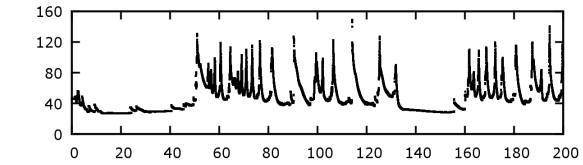

(a)

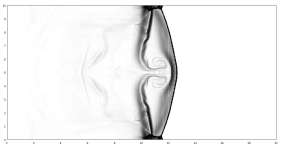

(b)

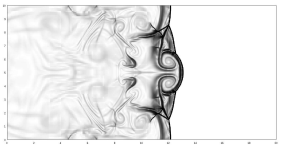

(c)

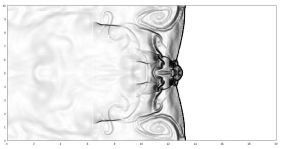

(d)

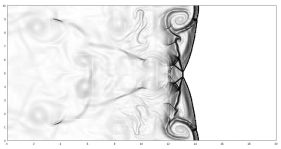

(e)

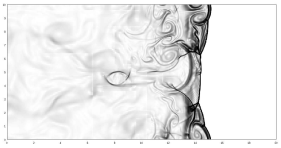

(f)

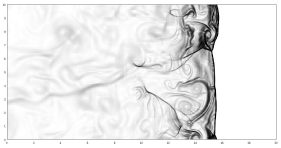

(g)

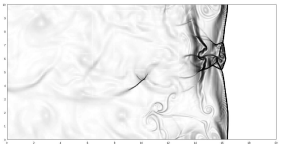

(h)

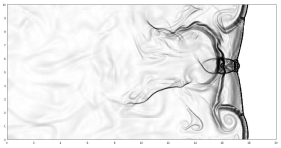

(i)

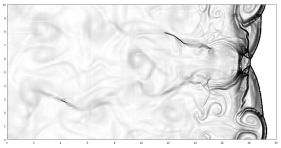

(j)

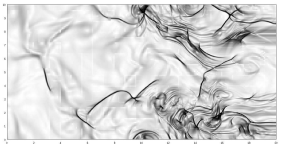

(k)

Figure 5.7. Density gradient plots for a strongly unstable detonation $\gamma = 1.2$, $E_0^* = 50.00$, $Q_0 = 50.00$ and $f = 1.10$, $CFL \approx 0.95$; (a) f = 1.10 (b) t = 30 (c) t = 40 (d) t = 50 (e) t = 60 (f) t = 70 (g) t = 80 (h) t = 90 (i) t = 100 (j) t = 110 (k) t = 120.

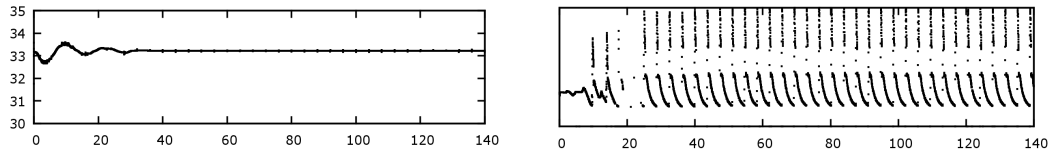

(a) (b)

Figure 5.8. Von Neumann pressure histories for longitudinally stable wave: a) 1D longitudinal and b) 2D transverse waves for $\gamma = 1.2$, $E_0^* = 20.00$, $Q_0 = 38.60$ and $f = 1.001$, $CFL \approx 0.95$.

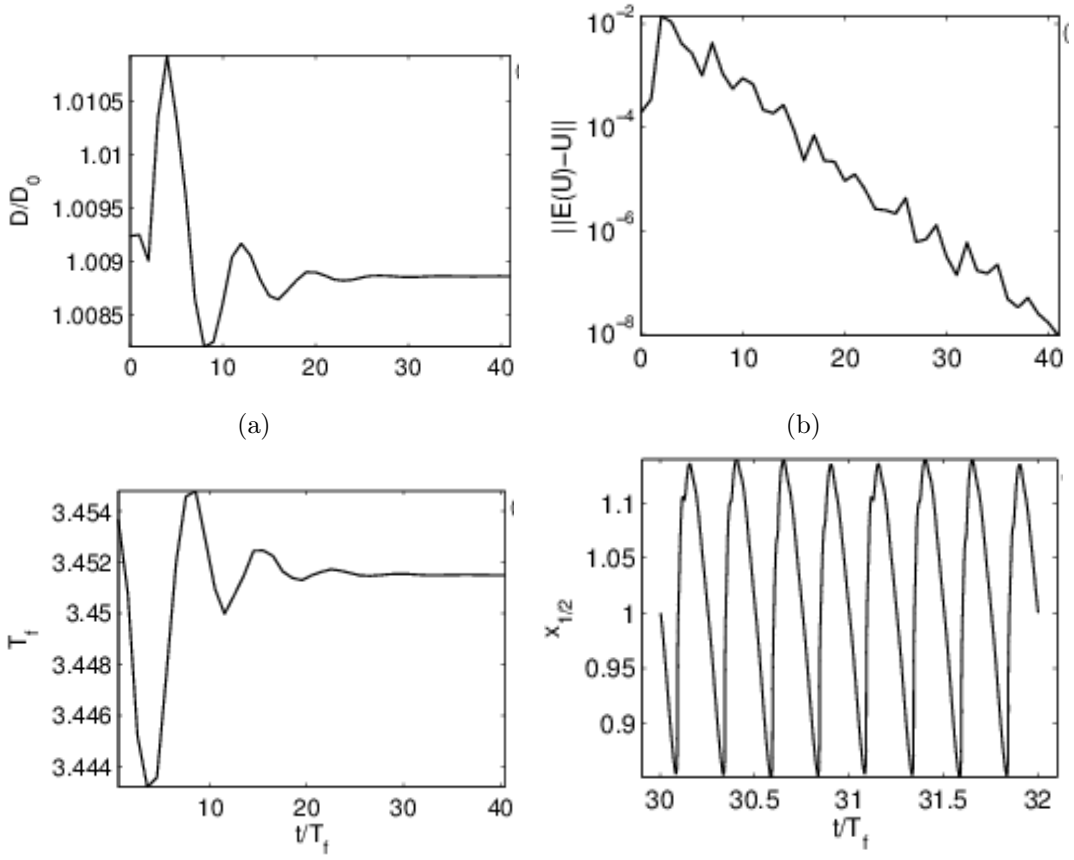

(a) (b)

(c) (d)

Figure 5.9. Convergence to the time-periodic base flow. (a) Ratio of detonation velocity to the ZND analogue; (b) convergence in norm of the U solution between consecutive iterations; (c) fundamental period T_f; (d) half reaction distance based on the space-mean progress of reaction, see equation (5.2), for two periods.

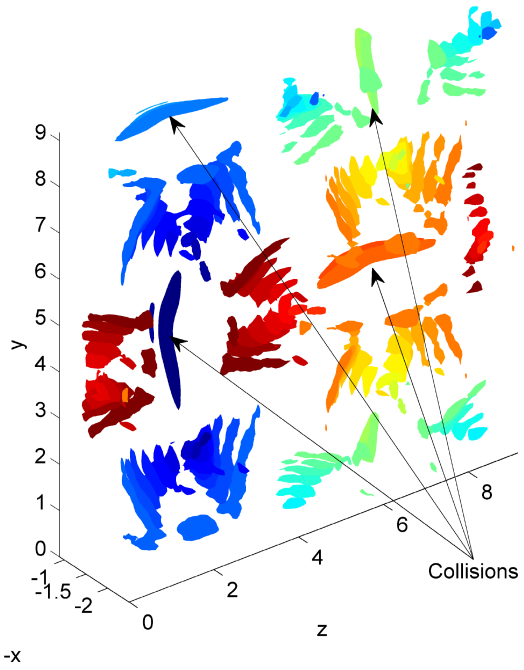

Figure 5.10. Pressure iso–surfaces drawn for $p = 0.8\ p_{\max}$ during a fundamental period T_f. The iso–surfaces are colored according to the time lag from the beginning of the period: dark blue denotes the zero lag contour while dark red denotes the solution after one period T_f. The arrows indicate the four collisions occurring in the $y - z$ periodic space. The aspect ratio in the x direction is stretched by $3/2$. The flow direction is from the back to the front of the figure.

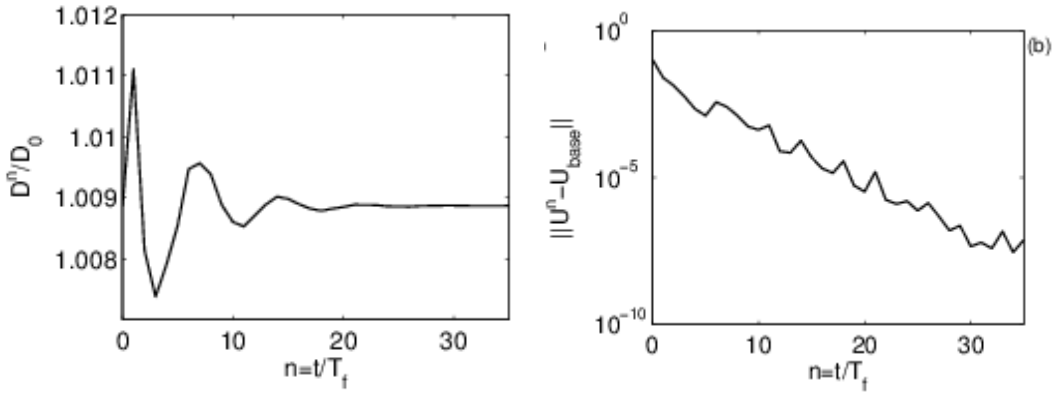

(a) (b)

Figure 5.11. Evolution of the perturbation over the number of Poincaré cycles n. (a) Ratio of detonation velocity to the ZND analogue; (b) L_2 norm of the difference between the perturbed flow solution and the base flow.

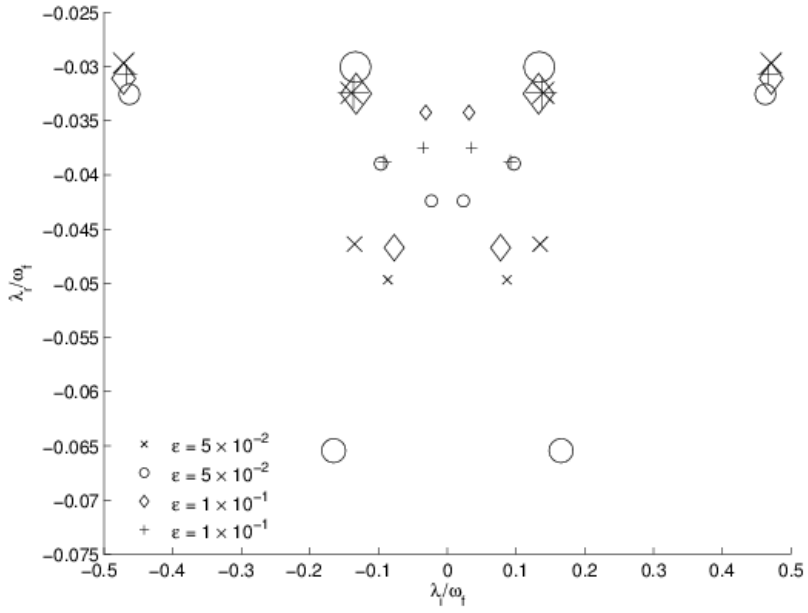

Figure 5.12. Scaled wave-frequencies from the DMD decomposition of the operator $\mathcal{E}$ in equation (5.6). The size of the symbols is proportional to the coherency of the modes. Different symbols refer to different random seeds in equation (5.8). The plot is symmetric about the y axis because global eigenvalues of real data are complex conjugate.

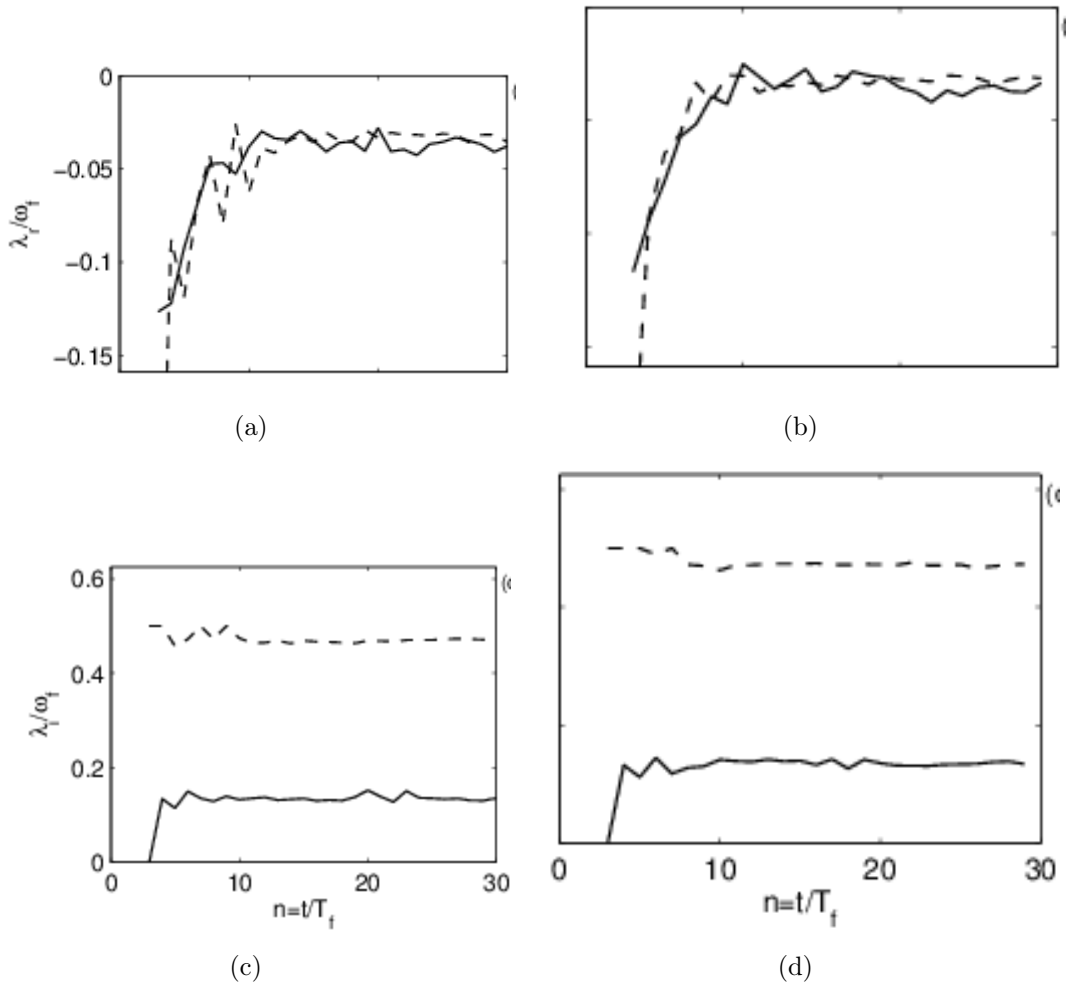

Figure 5.13. Convergence of the two dominant (least stable) eigenvalues against the number of snapshots n included in the DMD of the Poincaré map. (a) real part of the case marked with diamond symbols in Fig. 5.12; (b) imaginary part of the same case; (c) real part of the combined DMD of the four cases in Fig. 5.12; (d) imaginary part of the same combination.

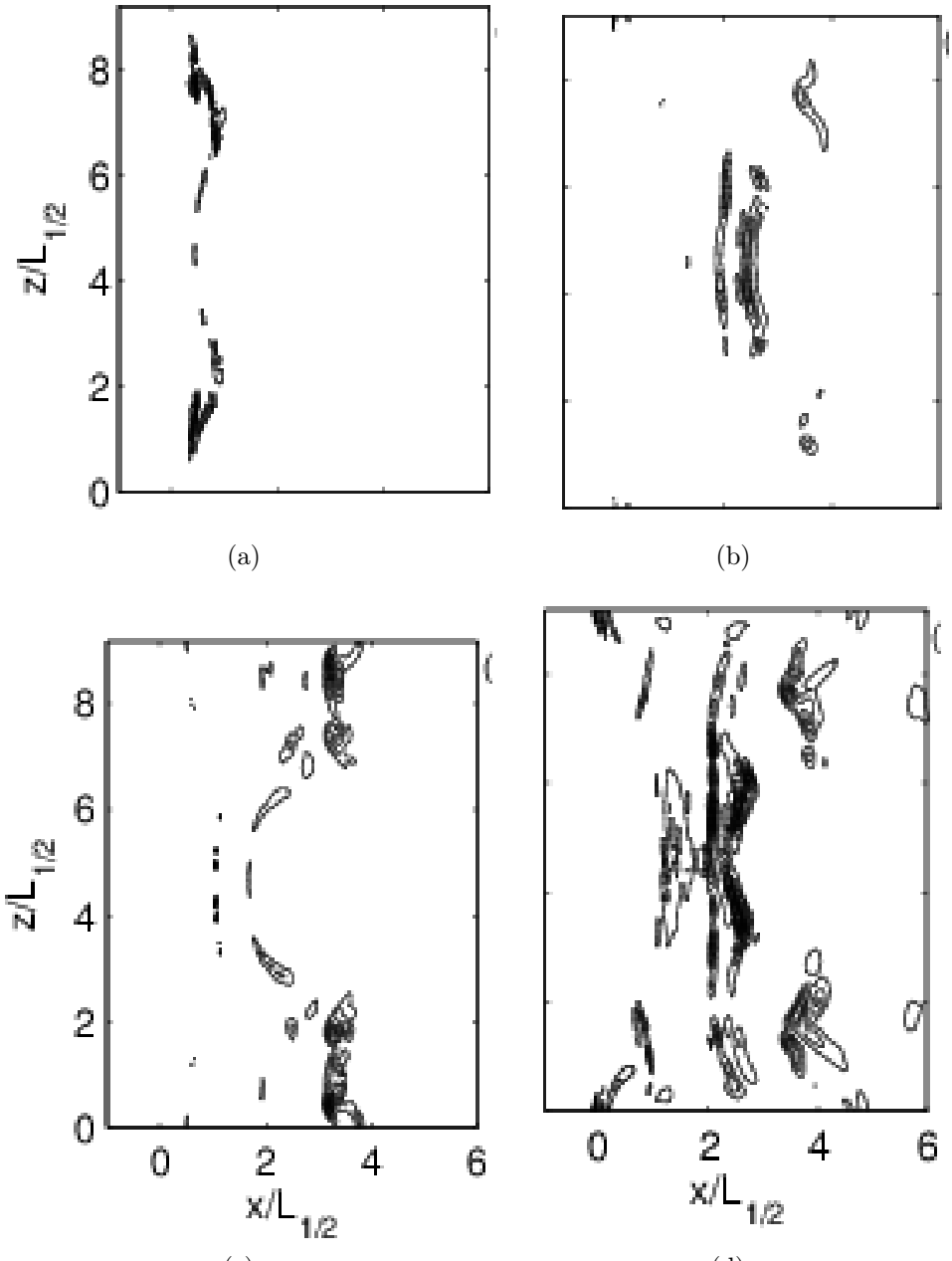

Figure 5.14. Contours of the eigenfunction for $\lambda_1 = -0.0325 + 0.135i$, showing 10 equally spaced contours of the chemical energy term Q'_5, see equation (5.7). Flow is from left to right. (a) $x - z$ cut at $y = 0$; (b) $x - z$ cut at $y = L_y/4$; (c) $x - z$ cut at $y = L_y/2$; (d) $x - z$ cut at $y = 3/4\ L_y$.

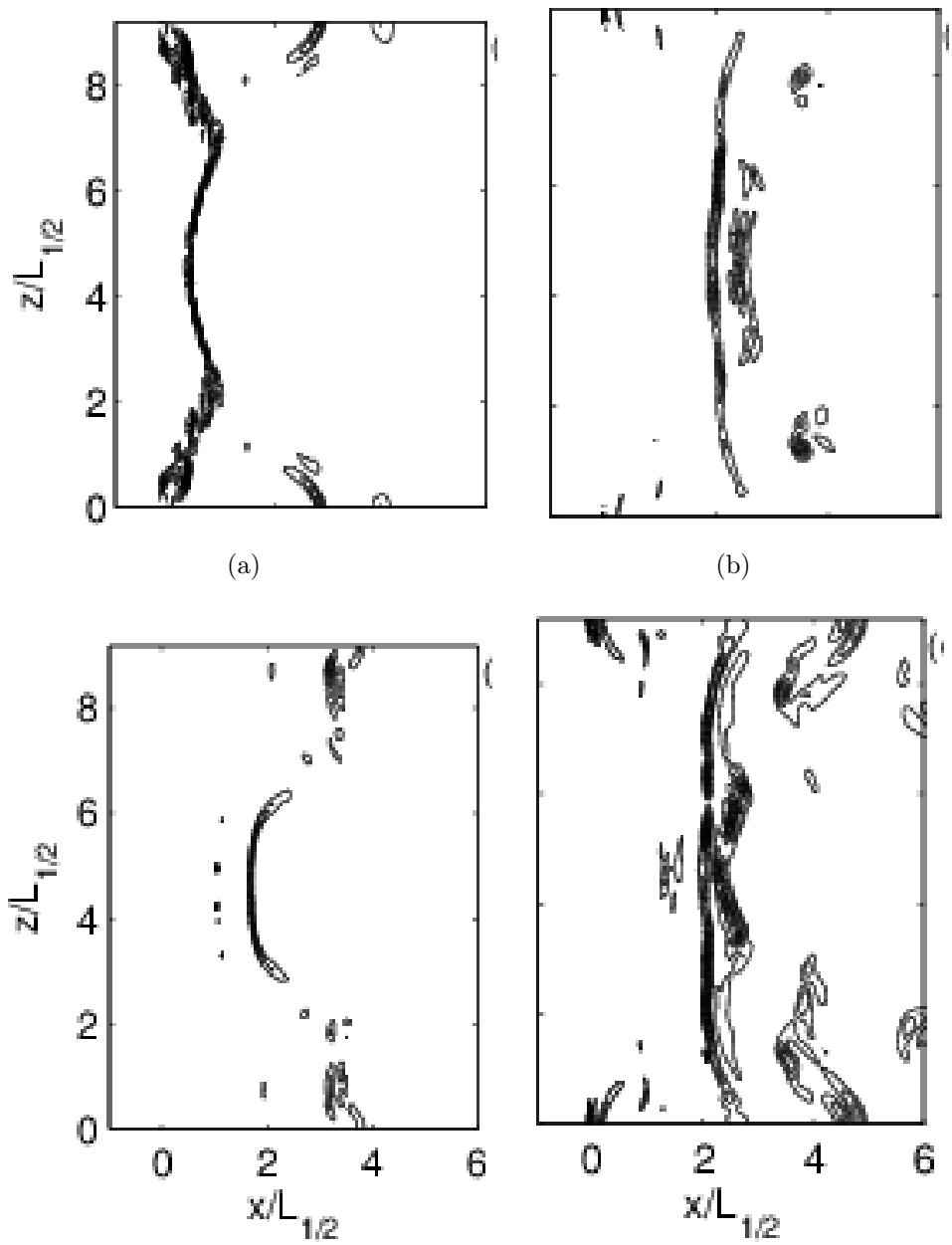

Figure 5.15. Contours of the eigenfunction for $\lambda_1 = -0.031 + 0.47i$, showing 10 equally spaced contours of the chemical energy term Q'_5, see equation (5.7). See Fig. 5.14 for more detail on the panels (a-d).

CHAPTER 6

DETONATIONS WITH DETAILED CHEMISTRY

In this chapter, the simulations using single–step chemistry in Chap. 5 are extended to detailed chemical kinetics. For one–dimensional simulations, 2 established cases are simulated. For two–dimensional simulation, the cellular structure is plotted by tracking the triple points through a complete run. The evolution of pressure, density and temperature are shown and the differences in the detonation structure between the single–step and detailed chemical kinetics are discussed.

6.1 One–dimensional Detonations With Detailed Chemical Kinetics

The 1D detonations with detailed chemistry are simulated in this section. The chemistry mechanism used was given by Westbrook with 9 species and 34 reactions. Two different hydrogen–oxygen mixtures are considered [105]. The first case is $[2:1:7]H_2 - O_2 - Ar$ and the second case is $[2:1]H_2 - O_2$. Both mixtures have initial conditions of pressure $p_0 = 0.0654atm$ and temperature of $289K$. The initial CJ detonation velocity was calculated using NASA–CEA code [43].

Figures 6.1 and 6.1 show the plots of pressure, density, temperature and velocity for the two mixtures. It is observed the the detonation shock intensity is higher for the $H_2 - -O_2$ mixture. This is expected as the argon dilution lowers the exothermicity of the hydrogen–oxygen detonations. Also, compared to the simplified chemistry solutions, the pressure fall–off behind the shock front is not so steep.

Figure 6.1 shows the temporal history of the von Neumann pressure peaks for both mixtures. Even with an unreacted gas perturbation as suggested by Oran [105],

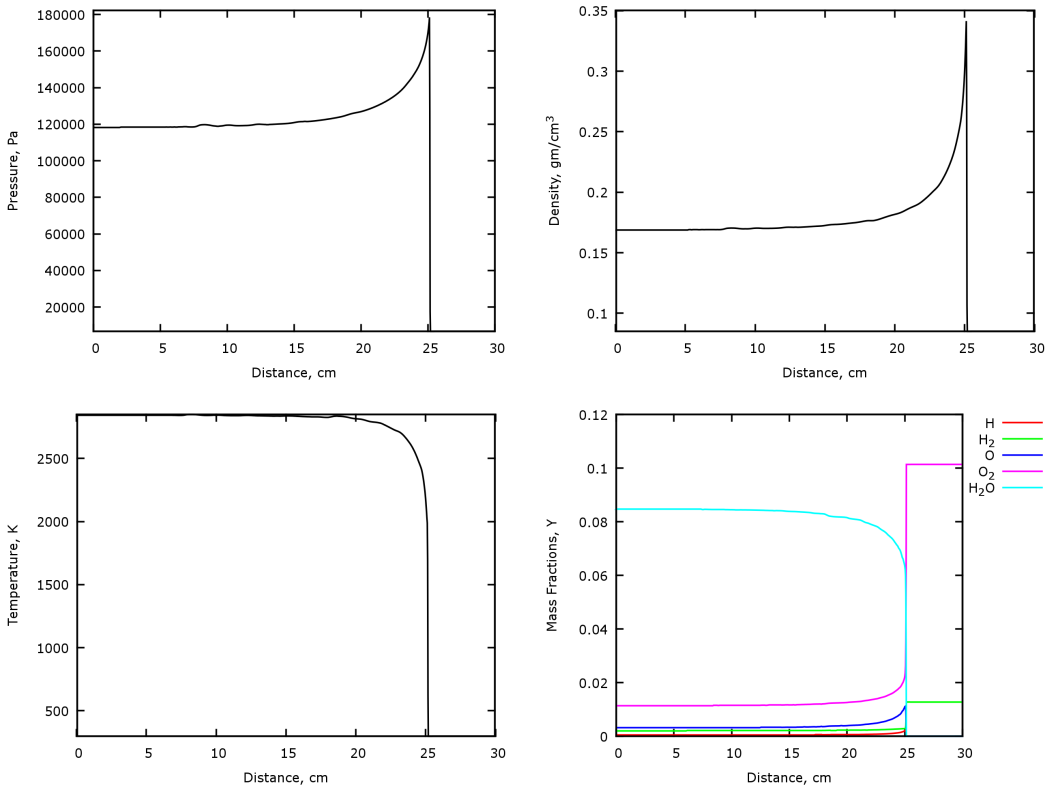

Figure 6.1. 1–D results for (a) Pressure, (b) Density, (c) Temperature and (d) Mass fraction of species for Hydrogen–Oxygen–Argon mixture.

both the mixtures were longitudinally stable. There are continuing efforts to find the stability limit for detailed chemical kinetics.

6.2 Two–dimensional Detonations With Detailed Chemical Kinetics

In this section, the 2D detonations displaying cellular structure are discussed. The test conditions for this case were borrowed from Oran et al.[17], who investigated the hydrogen–oxygen detonation with argon dilution. For this study, a $H_2 : O_2 : Ar$ mixture of concentrations $2 : 1 : 7$ is used at temperature of $298K$ and a pressure of $0.0654atm$.

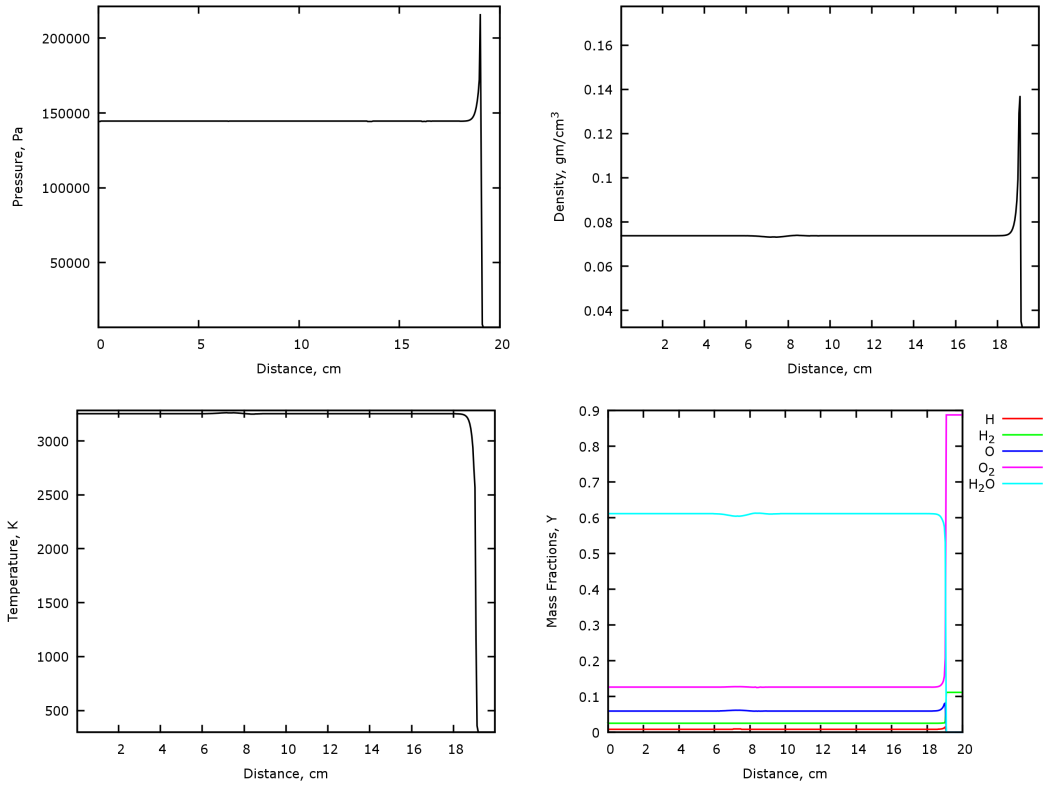

Figure 6.2. 1–D results for(a) Pressure, (b) Density, (c) Temperature and (d) Mass fraction of species for Hydrogen–Oxygen mixture.

Oran et al.used the technique of exploding an unreacted gas pocket behind a stable ZND wave to initiate the perturbation [17]. The same method is applied in this study. A stable ZND wave of the characteristics in Table is fixed at $X = 12.0$ similar to the 2D studies in Chap. 5. An unreacted gas pocket was positioned slightly downstream and center to the stable ZND wave, with dimensions of $1.4cm \times 1cm$. The reason for selecting the pocket size is to ensure that the unreacted pocket is at least $10Pts/l_{ig}$ in length, since from Table the induction length for $H_2 : O_2 : Ar$ mixture is $1.4mm$. The base grid is initialized to 800×200 with two levels of refinement resulting in a grid resolution of $114Pts/l_{ig}$. The simulation was solved till $t = 800\mu s$

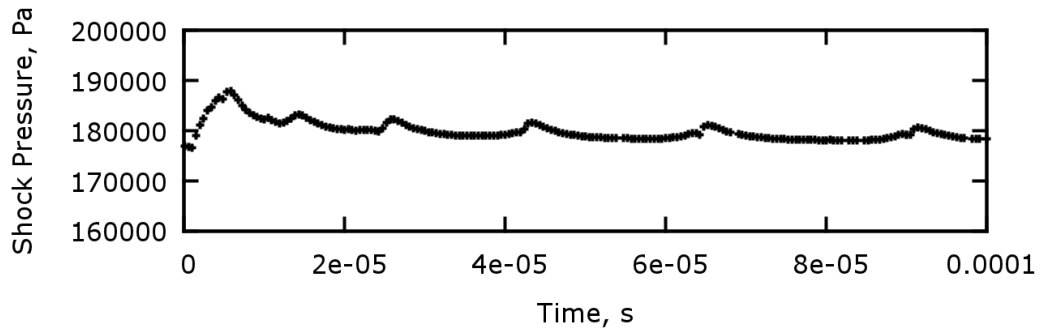

(a) E=28.30

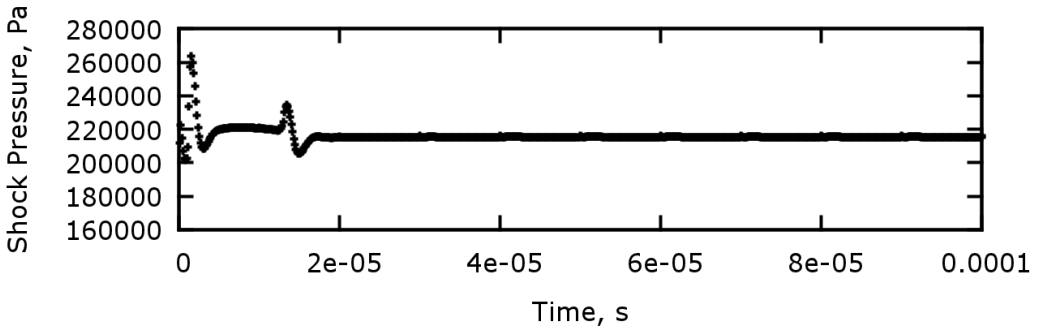

(b) E=28.35

Figure 6.3. Von Neumann shock re histories for (a) Hydrogen–Oxygen with Argon dilution and (b) stoichiometric Hydrogen–Oxygen mixtures.

at $CFL \approx 0.95$. Figure 6.2 shows the temporal evolution of the density gradient after the initial perturbation.

As seen previously in Chap. 5 in the case of weakly unstable detonations, the transverse oscillations dominate the longitudinal waves. After about $128\mu s$, oscillations become regular and periodic. Compared to the single–step chemistry solution, the disturbances are propagated much farther downstream for the weakly unstable case.

The simulations compare qualitatively to the simulations of Oran [105]. The grid–point resolution used in this study is much higher than those of previously published results [105, 86]. Deiterding also provided a comprehensive discussion of the flow features in the vicinity of the triple point structures [86]. The triple–point structures seem much more stronger than the simulation using simplified chemistry.

Figure 6.2 shows the front structure enlarged to study some of the details. In the detonation snapshot at $t = 326\mu s$, the induction zone behind the front is clearly visible, and the reaction zone is also immediately observable. The transverse waves are also sharply defined. The two snapshots give the differing motions of the triple point: at $t = 326\mu s$, the triple–points are moving away from the center and at $t = 438\mu s$, they are moving towards the center. In the detonation snapshot at $t = 438\mu s$, the there is an "empty" region behind the incident shock. This is an unreacted gas pocket and it occurs when the triple–points are pulling away from the center, the rate of reaction slows down to an extent to form these pockets of unreacted gas. Oran gave a detailed explanation regarding the formation of unreacted gas pockets and suggested that the mechanism behind the formation of cellular structure is due to the re–initiation of the triple–points when the shock structure comes into contact with the pocket [17].

6.2.1 Cellular Structure

Since the formation of cellular structures is the result of the triple point re–initiation and ultimately due to the instabilities in transverse waves, capturing and plotting the triple points over time should given the cellular structure of the detonation. Figure 6.6 shows the time–history of the triple point tracks showing regular cellular structure. The cellular structure is regular as expected from a hydrogen–oxygen detonation with high argon dilution.

6.3 Summary

In this chapter, detonations with detailed chemistry were simulated. For one–dimensional simulations, two cases $[2:1:7]H_2:O_2:Ar$ and $[2:1]H_2:O_2$ were simulated. The von Neumann pressures were compared to experimental studies to validate the model. For two–dimensional solutions, a single case of $[2:1:7]H_2:O_2:Ar$ was simulated. Some unique features were identified and the cellular structure was plotted using the triple–point tracks. The transverse instabilities were shown to affect the strength of the triple point. All the simulations had $T = 298K$ and $p_0 = 0.0654atm$.

The study to determine whether longitudinal oscillations exist was attempted, but without the knowledge of the stability limit, the study as not successful. Unlike simplified chemistry model, where the target parameters where reduced to activation energy or the overdrive parameter, such a simplification cannot be performed with detailed chemical kinetics. Some of the species might require to be frozen in equilibrium for this study to be successful. Nevertheless, efforts are underway to discover the longitudinal stability limit and extend the theory of bifurcations to detailed chemical kinetics.

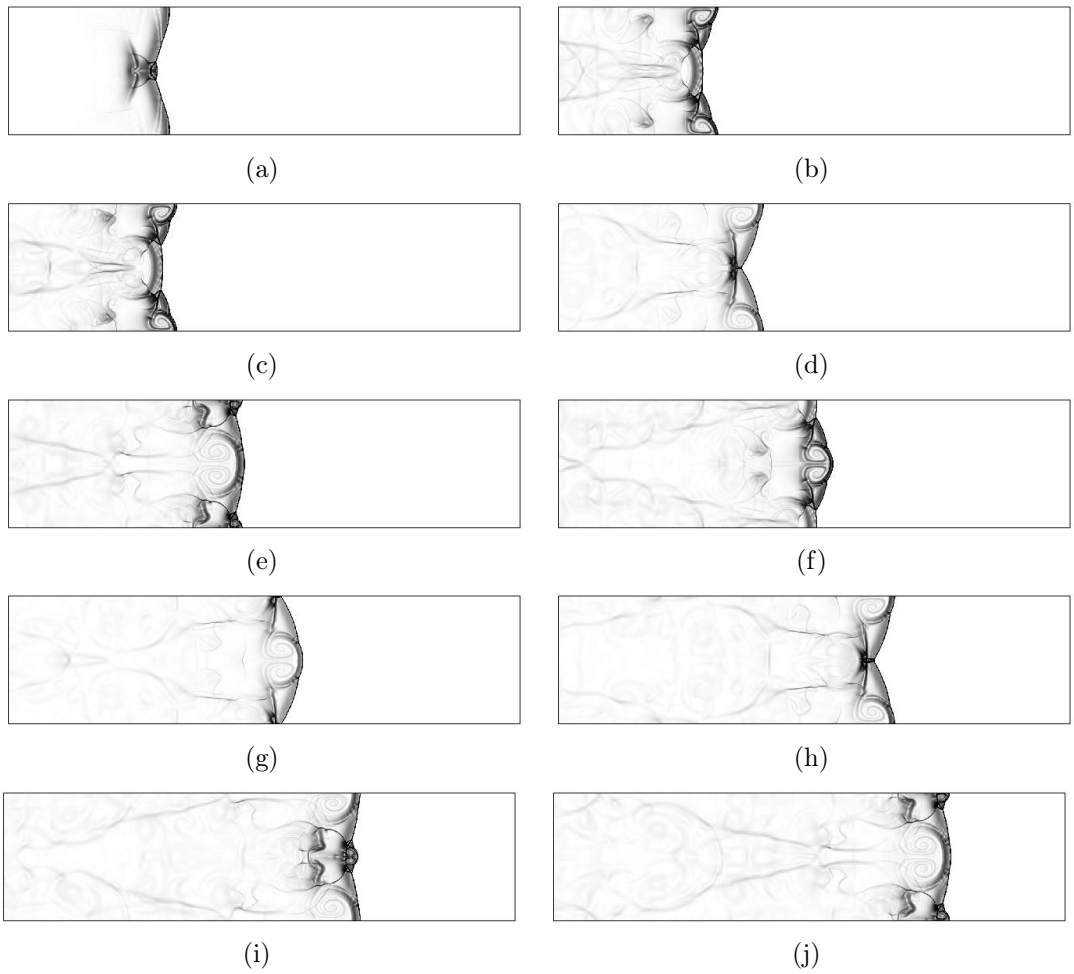

Figure 6.4. Schlieren visualization of the temporal evolution of density gradient $\bar{\rho}$ illustrating the transversal oscillations; (a) $t = 32\mu s$ (b) $t = 128\mu s$ (c) $t = 192\mu s$ (d) $t = 272\mu s$ (e) $t = 352\mu s$ (f) $t = 448\mu s$ (g) $t = 512\mu s$ (h) $t = 624\mu s$ (i) $t = 688\mu s$] (j) $t = 800\mu s$.

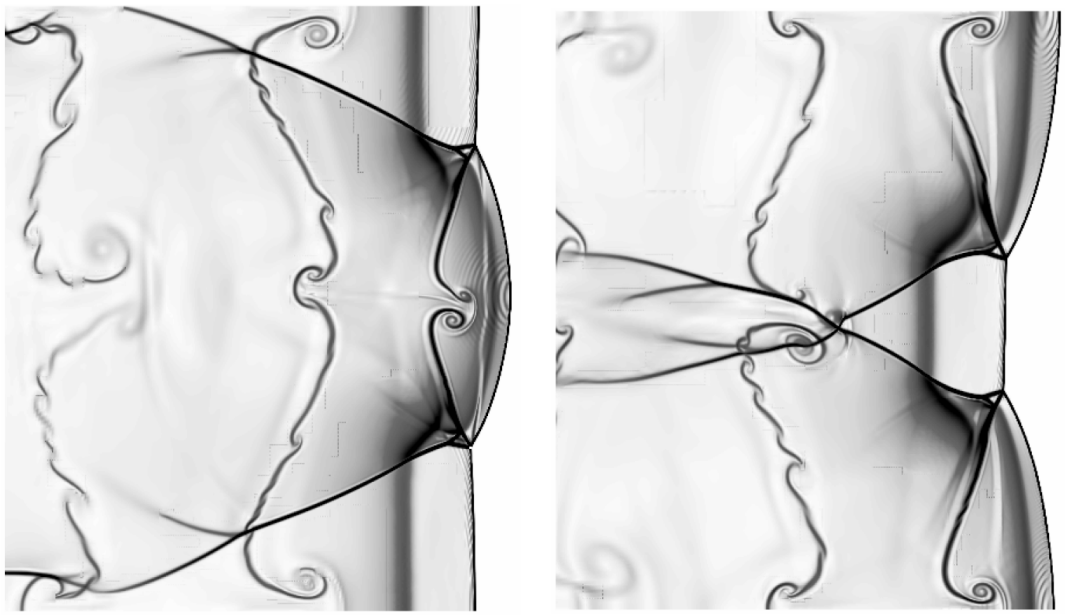

(a) (b)

Figure 6.5. Enlarged view of the front showing induction zone, the transverse wave, triple–points and Mach–stem at time (a) $t = 326\mu s$ (b) $t = 438\mu s$.

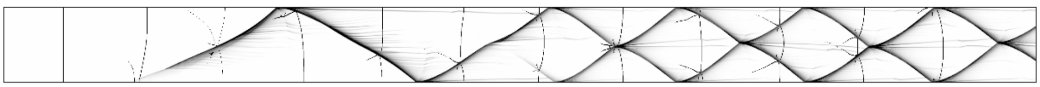

Figure 6.6. Temporal plot of the triple point tracks of a hydrogen–oxygen detonation simulation showing cellular structure.

CHAPTER 7

CONCLUSIONS

In the course of the research on detonations, the author discovered that the use of uniform meshes for solving reactive flow problems was prohibitively expensive if it was attempted to capture the entire spatio–temporal regime. Therefore, a robust mesh refinement strategy based on Berger–Colella block structured mesh refinement has been developed and integrated with a suitable numerical methods package to solve reactive flows with detailed chemical kinetics. The DAGH framework on which the current strategy is based, has been updated with a novel partitioning scheme based on the modified Peano–Hilbert space–filling curve. This upgraded technique ensures the capability for the framework to have high degree of scalability in modern supercomputers.

The reactive Euler equations are solved using the Roe–HLL(E) scheme, and the numerical scheme can switch from Roe to the more robust HLL scheme upon detecting rapid expansion to avoid non–physical negative densities. To attain higher order accuracies, a MUSCL extrapolation on the primitive variables is employed. The source terms are decoupled from the hydrodynamic terms by using a fractional step method. A linearly implicit Runge–Kutta method has been used to integrate the the source terms and to avoid numerical stiffness, a backward differentiation approach is used. The use of these techniques along with adaptive mesh refinement allows for highly accurate and computationally fast simulations of detonation phenomena.

In this research, detonations are simulated in two ways: using irreversible single–step Arrhenius chemical kinetics and detailed chemical kinetics. For simulations using

the single step chemistry, the longitudinal period–doubling phenomena is shown by varying both the activation energy and the overdrive parameter and a mechanism leading to the collapse of the period–doubling modes has been uncovered. Also, in the two–dimensional simulations, for a longitudinally stable case, the unstable transverse oscillation has been discovered. A linear stability Floquet analysis is conducted on three–dimensions and confirms the presence of transverse instabilities for a longitudinally stable case. One-dimensional analyses consider waves that are longitudinally unstable about the ZND profiles, whereas three dimensional analyses are usually applied to transversely unstable detonations.

Detonations using detailed chemical kinetics have also been simulated in this work. The chemical reaction rate terms are provided by CHEMKIN-III using a Westbrook reduced hydrogen–oxygen mechanism using 9 chemical species. Simulations have been carried out for hydrogen–oxygen detonations with and without argon dilution in one–dimensions and with argon in two dimensions. The solutions are longitudinally stable and transversely unstable. Closer inspection of the front reveals the re–initiation of the triple–point mechanism which leads to the formation of the cellular structure of detonation. The cellular structure has been plotted by tracking the triple points in the detonation front.

The simulations are comparable in accuracy to published literature. Capability to simulate two–dimensions have been explored in both single–step and detailed kinetics.

CHAPTER 8

POSSIBLE FUTURE WORK

The work that has been accomplished in this dissertation can be carried forward towards several directions, hence the need for a separate chapter. The AMR framework has been developed only for Cartesian meshes and simple geometries. So far, there are no mesh refinement toolkits available to solve reactive flow in complex geometries. The challenges associated with the design of AMR for complex geometries are very steep indeed but efforts are underway. The latest release of Chombo, an AMR framework, provides the ability to solve embedded boundary problems, a step closer to developing meshes for complicated geometries [90].

If there could be some drawbacks with the design of the AMR framework in this research, it would be the following: the partition strategy used here was very novel at the time of its inception, but currently it has become obsolete. Modern processors are developed with a large amount of cache memory and programs have evolved to use them to the fullest extent. Metis and ParMetis are toolkits which work at runtime to effectively load–balance between processors. There could be an effort to upgrade to one of the more recent load–balancers to take advantage of the latest processors and computer clusters.

Since this work was performed using inviscid Euler equations due to difficulties associated with designing AMR for viscous compressible flows, the next logical step would be to extend the framework to solve Navier–Stokes equations. There are some difficulties resolving and capturing a viscous shock while simultaneously decreasing or increasing refinements, but one possibility is investigating the use of dual schemes ie.

the shock can be captured using an inviscid scheme and the reaction could be solved with a viscous technique. Regarding the numerical techniques, the Godunov schemes used in this work could use an upgrade: the low–dissipative, high–order and well–balanced filter schemes could be used. Godunov schemes are very robust till a sharp discontinuity is encountered; then some novel techniques will have to be employed to counter the oscillatory nature of Riemann solvers. This adds to the computational expense. The detailed chemical kinetics part in this research is capable of handling detailed hydrocarbon mechanisms but the source term integration can be sped up by using the newer *TR-BDF* which is a two–stage Runge–Kutta that combines one step of the trapezoidal method or an implicit Crank–Nicholson update. These methods have proven, especially when diffusion terms are included, to be faster and more reliable than the approach employed in this research work. The use of bisection method in source term integration, by experience from this research, is fraught with problems and should be avoided. A Newton–Raphson iteration is more robust, even though it might be slower.

On the simulation side, detonations with single–step kinetics may not be of focus recently, but their importance has not diminished. Extending the current research to attempting to find transverse period–doubling criteria could be the short–term goal. But before that, the numerical framework needs to be extended to three–dimensions. Transverse waves are not just a Y direction phenomena, but also a Z direction phenomena. For single–step chemistry, the extension to three–dimensions is almost complete and will be completed by this author for the purpose of finding the bifurcation parameters of transverse waves. But with the existing volume of data, one of the major needs would be the development of a power spectral density method to accurately capture the von–Neumann peaks during the period–doubling phases.

For solving detonations with detailed chemistry, the next step would be to move to mechanisms involving complex hydrocarbons such as the Konnov mechanism. Also, an attempt should be made to identify the stability limits for detonations with detailed chemical kinetics.

APPENDIX A

1D LONGITUDINAL INSTABILITIES: EFFECT OF ACTIVATION ENERGY VARIATION

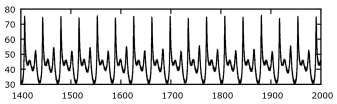

(a) E=28.30

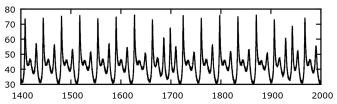

(b) E=28.35

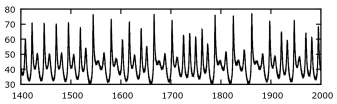

(c) E=28.40

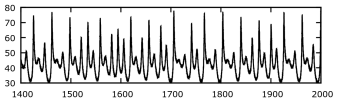

(d) E=28.45

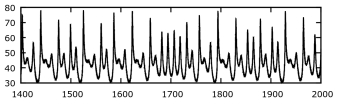

(e) E=28.50

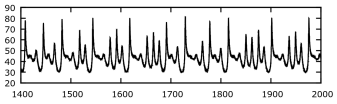

(f) E=28.60

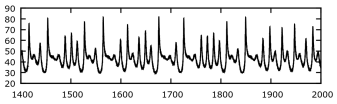

(g) E=28.70

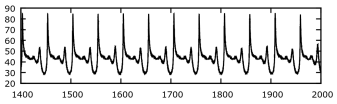

(h) E=28.80

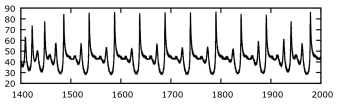

(i) E=28.90

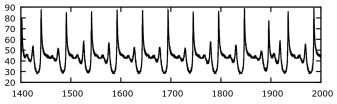

(j) E=29.00

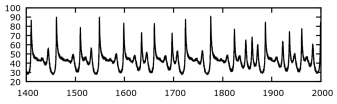

(k) E=29.10

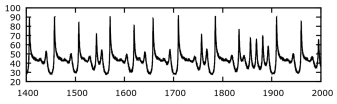

(l) E=29.20

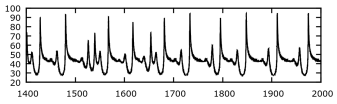

(m) E=29.30

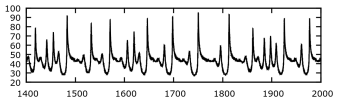

(n) E=29.40

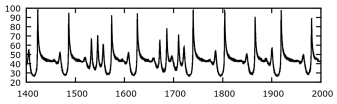

(o) E=29.50

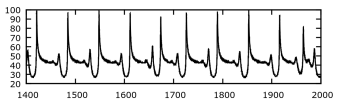

(p) E=29.60

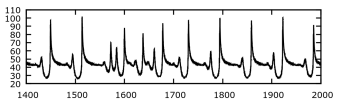

(q) E=29.70

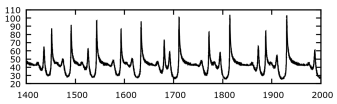

(r) E=29.80

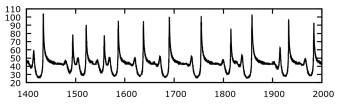

(s) E=29.90

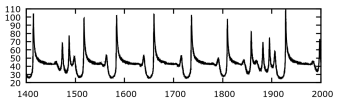

(t) E=30.00

Figure A.1. Von Neumann shock pressure histories for overdrive parameters $E_0^* = 28.30 - 30.00$, $CFL \approx 0.95$.

REFERENCES

[1] J. M. Austin, "The role of instability in gaseous detonation," Ph.D. dissertation, California Institute of Technology, 2003.

[2] M. Short and D. S. Stewart, "Cellular detonation stability. Part 1. A normal-mode linear analysis," *Journal of Fluid Mechanics*, vol. 368, pp. 229–262, Aug. 1998.

[3] J. Dennis, "Partitioning with space-filling curves on the cubed-sphere," in *Proceedings International Parallel and Distributed Processing Symposium*. IEEE Comput. Soc, 2003, p. 6.

[4] D. L. Chapman, "On the rate of explosion in gases," *Philosophical Magazine*, vol. 47, pp. 90–104, 1899.

[5] E. Jouguet, "On the propagation of chemical reactions in gases," *J de Mathematiques Pures et Appliquees*, vol. 1, pp. 347–425, 1905.

[6] Y. B. Zel'dovich, "On the theory of the propagation of detonation in gaseous systems," NASA TM-1261, Tech. Rep., 1940.

[7] R. A. Strehlow, "Transverse wave structure in detonations," *Symposium (International) on Combustion*, vol. 11, no. 1, pp. 683–692, 1967.

[8] J. J. Erpenbeck, "Stability of Idealized One-Reaction Detonations," *Physics of Fluids*, vol. 7, no. 5, p. 684, 1964.

[9] H. O. Barthel, "Predicted spacings in hydrogen-oxygen-argon detonations," *Physics of Fluids*, vol. 17, no. 8, p. 1547, 1974.

[10] J. Shepherd, "Chemical kinetics of hydrogen-air-diluent detonations," in *International Colloquium on Dynamics of Explosions and Reactive Systems, 10 th,*.

Berkeley, CA: New York, American Institute of Aeronautics and Astronautics, Inc., 1985, pp. 263–293.

[11] Z. Liang and L. Bauwens, "Detonation structure with pressure-dependent chain-branching kinetics," *Proceedings of the Combustion Institute*, vol. 30, no. 2, pp. 1879–1887, Jan. 2005.

[12] J. Buckmaster, "The effect of structure on the stability of detonations I. Role of the induction zone," *Symposium (International) on Combustion*, vol. 21, no. 1, pp. 1669–1676, 1988.

[13] A. Bourlioux, A. Majda, and V. Roytburd, "Theoretical and numerical structure for unstable one-dimensional detonations," *SIAM Journal on Applied Mathematics*, vol. 51, no. 2, pp. 303–343, 1991.

[14] a. Bourlioux and a. J. Majda, "Theoretical and numerical structure of unstable detonations," *Philosophical Transactions of the Royal Society A: Mathematical, Physical and Engineering Sciences*, vol. 350, no. 1692, pp. 29–68, Jan. 1995.

[15] M. Short, "Multidimensional linear stability of a detonation wave at high activation energy," *SIAM Journal on Applied Mathematics*, vol. 57, no. 2, pp. 307–326, 1997.

[16] D. Williams, L. Bauwens, and E. S. Oran, "Detailed structure and propagation of three-dimensional detonations," *Symposium (International) on Combustion*, vol. 26, no. 2, pp. 2991–2998, 1996.

[17] V. N. Gamezo, D. Desbordes, and E. S. Oran, "Formation and evolution of two-dimensional cellular detonations," *Combustion and Flame*, vol. 116, no. 1-2, pp. 154–165, Jan. 1999.

[18] N. Tsuboi, S. Katoh, and a. K. Hayashi, "Three-dimensional numerical simulation for hydrogen/air detonation: Rectangular and diagonal structures," *Proceedings of the Combustion Institute*, vol. 29, no. 2, pp. 2783–2788, Jan. 2002.

[19] L. Massa, J. M. Austin, and T. L. Jackson, "Triple-point shear layers in gaseous detonation waves," *Journal of Fluid Mechanics*, vol. 586, p. 205, Aug. 2007.

[20] A. Majda, "The existence and stability of multi-dimensional shock fronts," *AMERICAN MATHEMATICAL SOCIETY*, vol. 4, no. 3, pp. 342–344, 1981.

[21] G. Lyng and K. Zumbrun, "A stability index for detonation waves in Majda's model for reacting flow," *Physica D: Nonlinear Phenomena*, vol. 194, no. 1-2, pp. 1–29, July 2004.

[22] B. Texier and K. Zumbrun, "Relative Poincaré-Hopf bifurcation and galloping instability of traveling waves," *Methods and Applications of Analysis*, vol. 12, no. 4, p. 349, 2005.

[23] ——, "Transition to longitudinal instability of detonation waves is generically associated with Hopf bifurcation to time-periodic galloping solutions," *Arxiv*, pp. 1–59, 2010.

[24] H. Ng, A. Higgins, C. Kiyanda, M. Radulescu, J. Lee, K. Bates, and N. Nikiforakis, "Nonlinear dynamics and chaos analysis of one-dimensional pulsating detonations," *Combustion Theory and Modelling*, vol. 9, no. 1, pp. 159–170, Feb. 2005.

[25] A. K. Henrick, T. D. Aslam, and J. M. Powers, "Simulations of pulsating one-dimensional detonations with true fifth order accuracy," *Journal of Computational Physics*, vol. 213, no. 1, pp. 311–329, Mar. 2006.

[26] G. Sharpe, "Transverse waves in numerical simulations of cellular detonations," *Journal of Fluid Mechanics*, vol. 447, pp. 31–52, 2001.

[27] F. Pintgen, C. Eckett, J. Austin, and J. Shepherd, "Direct observations of reaction zone structure in propagating detonations," *Combustion and Flame*, vol. 133, no. 3, pp. 211–229, May 2003.

[28] J. Von Neumann, *On the theory of stationary detonation waves.* Princeton N.J.: [s.n.], 1942.

[29] F. Wildon and W. C. Davis, *Detonation: Theory and Experiment.* Berkeley, CA: University of California Press, 1979.

[30] R. J. Leveque, *Numerical methods for conservation laws*, 2nd ed. Basel, Switzerland: Birkhauser, 1992.

[31] R. Sanders, E. Morano, and M.-C. Druguet, "Multidimensional Dissipation for Upwind Schemes: Stability and Applications to Gas Dynamics," *Journal of Computational Physics*, vol. 145, no. 2, pp. 511–537, 1998.

[32] M. Berger and R. Leveque, "Adaptive mesh refinement using wave-propagation algorithms for hyperbolic systems," *SIAM Journal on Numerical Analysis*, vol. 35, no. 6, pp. 2298–2316, 1998.

[33] H. Sagan, *Space-filling curves.* New York, NY: Springer-Verlag, 1994.

[34] H. D. Gruschka and F. Wecken, *Gasdynamic theory of detonation.* New York, NY: Gordon & Breach Science Publishers Ltd, 1972.

[35] A. N. Dremin, *Toward Detonation Theory.* New York, NY: Springer-Verlag, 1999.

[36] J. H. S. Lee, "Dynamic Parameters of Gaseous Detonations," *Annual Review of Fluid Mechanics*, vol. 16, pp. 311–336, 1984.

[37] P. A. Urtiew and A. K. Oppenheim, "Experimental Observations of the Transition to Detonation in an Explosive Gas," *Proceedings of the Royal Society of London. Series A, Mathematical and Physical Sciences*, vol. 295, no. 1440, pp. 13–28, 1966.

[38] J. von Neumann, *On the Theory of Stationary Detonation Waves*, 1942.

[39] W. Döring, "On detonation processes in gases," *Annals of Physics*, vol. 43, pp. 421—-436, 1943.

[40] J. Shepherd, "Detonation waves and propulsion," in *Combustion in High Speed Flows: Proceedings of a workshop on Combustion*, J. Buckmaster, Ed. Hampton, VA: Kluwer Academic Publishing, 1992, pp. 373–420.

[41] P. Kaps and S. Poon, "Rosenbrock methods for stiff ODEs: A comparison of Richardson extrapolation and embedding technique," *Computing*, vol. 40, pp. 17–40, 1985.

[42] T. J. Dekker, "Finding a zero by means of successive linear interpolation," in *Symposium of Constructive Aspects of Fundamental Theoretical Algebra*, Zurich, 1967, pp. 37—-48.

[43] B. J. McBride and S. Gordon, "NASA Chemical Equilibrium Analysis (CEA): Computer Program for Calculating and Fitting Thermodynamic Functions," 1992.

[44] R. A. Strehlow, *Fundamentals Of Combustion*. Scranton: International Press, 1968.

[45] ——, "Gas Phase Detonations: Recent Developments," *Combustion and Flame*, vol. 12, pp. 81–101, 1968.

[46] ——, "The Nature Of Transverse Waves In Detonations," *Astronautica Acta*, vol. 14, pp. 539–548, 1969.

[47] ——, "Multi-dimensional Detonation Wave Structure," *Astronautica Acta*, vol. 15, no. 345-357, 1970.

[48] J. P. Saint-Cloud, C. Gerraud, C. Brochet, and N. Manson, "Some Properties of Very Unstable Detonations In Gaseous Mixtures," *Astronautica Acta*, vol. 17, pp. 487–498, 1972.

[49] P. Clavin and L. He, "Acoustic effects in the nonlinear oscillations of planar detonations," *Physics Review E*, vol. 53, no. 5, pp. 4778–4784, 1996.

[50] L. Massa, R. Kumar, and P. Ravindran, "Dynamic mode decomposition analysis of detonation waves," *Physics of Fluids*, vol. under revi, 2012.

[51] L. Massa and P. Ravindran, "On the effects of finite rate carbon/oxygen chemistry on supersonic jet instability," *Journal of Fluid Mechanics*, vol. under revi, 2012.

[52] V. E. Gordeev, "The Cause Of Multiplication Of Discontinuities In A Detonation Front," *Soviet Physics Doklady*, vol. 226, pp. 228–291, 1976.

[53] R. J. Kee, F. M. Rupley, E. Meeks, and J. A. Miller, "CHEMKIN-III: A FORTRAN Chemical Kinetics Package For The Analysis Of Gasphase Chemical And Plasma Kinetics," 1996.

[54] C. K. Westbrook, "Chemical Kinetics of Hydrocarbon Oxidation in Gaseous Detonations," *Combustion and Flame1*, vol. 46, pp. 191–210, 1982.

[55] J. C. Tannehill, D. A. Anderson, and R. H. Pletcher, *Computational Fluid Mechanics and Heat Transfer*, 2nd ed. Taylor & Francis, 1997.

[56] B. Einfeldt, C. D. Munz, P. L. Roe, and B. Sjogreen, "On Godunov-type methods near low densities," *Journal of Computational Physics*, vol. 92, pp. 273–295, 1991.

[57] E. F. Toro, *Riemann Solvers and Numerical Methods for Fluid Dynamics: A Practical Introduction*, 3rd ed. Springer-Verlag, 2009.

[58] R. Courant, K. Friedrichs, and H. Lewy, "Über die partiellen Differenzengleichungen der mathematischen Physik," *Mathematische Annalen*, vol. 100, no. 1, pp. 32–74, 1928.

[59] S. K. Godunov, "A difference method for numerical calculation of discontinuous solutions of the equations of hydrodynamics," *Matematicheskii Sbornik*, vol. 47(89), no. 3, pp. 271–306, 1959.

[60] E. Godlewski and P. A. Raviart, *Numerical approximation of hyperbolic systemsof Conservation laws.* New York, NY: Springer-Verlag, 1996.

[61] D. Kroner, *Numerical schemes for Conservation laws.* Wiley-Teubner Series, 1997.

[62] P. L. Roe, "Approximate Riemann solvers, parameter vectors and difference schemes," *Journal of Computational Physics1*, vol. 43, pp. 357–372, 1981.

[63] A. Harten and J. M. Hyman, "Self-adjusting grid methods for one-dimensional hyperbolic conservation laws," *Journal of Computational Physics*, vol. 50, pp. 289–315, 1983.

[64] A. Harten, P. D. Lax, and B. van Leer, "On upstream differencing and Godunov-type schemes for Conservation laws," *SIAM Review*, vol. 25, pp. 35–61, 1983.

[65] B. Einfeldt, "On Godunov-type methods for gas dynamics," *2SIAM Journal on Numerical Analysis*, vol. 25, pp. 294–318, 1988.

[66] B. van Leer, "Towards the ultimate conservative difference scheme I. The quest of monotonicity," *Springer Lecture Notes for Physics*, vol. 18, pp. 163–168, 1973.

[67] ——, "Towards the ultimate conservative difference scheme II. Monotonicity and conservation combined in a second order scheme," *Journal of Computational Physics1*, vol. 14, pp. 361–370, 1974.

[68] ——, "Towards the ultimate conservative difference scheme III. Upstream-centered finite difference schemes for ideal compressible flow," *Journal of Computational Physics*, vol. 23, pp. 263–275, 1977.

[69] R. J. Leveque, *Finite volume methods for hyperbolic problems.* Cambridge Univ Press, 2002.

[70] G. Strang, "On the construction and comparison of difference schemes," *SIAM Journal on Numerical Analysis*, vol. 5, no. 3, pp. 506–517, 1968.

[71] E. Hairer, S. P. Norsett, and G. Wanner, *Solving ordinary differential equations II. stiff and differential-algebraic problems.* New York, NY: Springer-Verlag, 1993.

[72] R. J. Leveque, "CLAWPACK software," 2006.

[73] ——, "Wave propagation algorithms for multidimensional hyperbolic problems," *Journal of Computational Physics*, vol. 131, no. 2, pp. 327–353, 1997.

[74] M. Berger, "Local adaptive mesh refinement for shock hydrodynamics," *Journal of Computational Physics*, vol. 82, pp. 64–84, 1989.

[75] M. Parashar, "On partitioning dynamic adaptive grid hierarchies," in *Hawaii International Conference on,*, 1996.

[76] N. Uchiyama and O. Inoue, "On the performance of adaptive mesh refinement computation," *Shock Waves*, vol. 2, no. 2, pp. 117–120, June 1992.

[77] J. H. J. Niederhaus, J. a. Greenough, J. G. Oakley, D. Ranjan, M. H. Anderson, and R. Bonazza, "A computational parameter study for the three-dimensional shock–bubble interaction," *Journal of Fluid Mechanics*, vol. 594, pp. 85–124, Dec. 2007.

[78] J. Powers, "Review of Multiscale Modeling of Detonation," *Journal of Propulsion and Power*, vol. 22, no. 6, pp. 1217–1229, Nov. 2006.

[79] R. Lohner, "An adaptive finite element scheme for transient problems in CFD," *Computer Methods in Applied Mechanics and Engineering*, vol. 61, no. 3, pp. 323–338, 1987.

[80] R. Das, D. Mavriplis, J. Saltz, and S. Gupta, "The design and implementation of a parallel unstructured Euler solver using software primitives," *ICASE REPORT NO. 92-12/189625*, no. 92, 1992.

[81] a.M Khokhlov, "Fully Threaded Tree Algorithms for Adaptive Refinement Fluid Dynamics Simulations," *Journal of Computational Physics*, vol. 143, no. 2, pp. 519–543, July 1998.

[82] M. Berger and J. Oliger, "Adaptive mesh refinement for hyperbolic partial differential equations," *Journal of Computational Physics*, vol. 53, no. 3, pp. 484–512, 1984.

[83] S. F. McCormick, *Multilevel Adaptive Methods for Partial Differential Equations*. Society of Industrial and Applied Mathematics, 1989.

[84] J. Quirk, "A parallel adaptive grid algorithm for computational shock hydrodynamics," *Applied Numerical Mathematics*, vol. 20, no. 4, pp. 427–453, Apr. 1996.

[85] D. De Zeeuw and K. Powell, "An adaptively refined Cartesian mesh solver for the Euler equations," *Journal of Computational Physics*, vol. 104, pp. 56–68, 1993.

[86] R. Deiterding, "Parallel adaptive simulation of multi-dimensional detonation structures," Ph.D. dissertation, Brandenburgische Technische Universität Cottbus, 2003.

[87] P. MacNeice, "PARAMESH: A parallel adaptive mesh refinement community toolkit," *Computer Physics Communications*, vol. 126, no. 3, pp. 330–354, Apr. 2000.

[88] B. Fryxell, K. Olson, and P. Ricker, "FLASH: An adaptive mesh hydrodynamics code for modeling astrophysical thermonuclear flashes," *The Astrophysical Journal Supplement Series*, vol. 131, pp. 273–334, 2000.

[89] A. M. Wissink, R. D. Hornung, S. R. Kohn, S. S. Smith, and N. Elliott, "Large scale parallel structured AMR calculations using the SAMRAI framework," *Pro-*

ceedings of the 2001 ACM/IEEE conference on Supercomputing (CDROM) - Supercomputing '01, no. November, pp. 6–6, 2001.

[90] P. Colella, D. Graves, T. Ligocki, D. Martin, D. Modiano, D. Serafini, and B. Van Straalen, "Chombo Software Package for AMR Applications-Design Document," Applied Numerical Algorithms Group, Computational Research Division, Lawrence Berkeley National Laboratory, Berkeley, CA, Tech. Rep., 2000.

[91] W. Henshaw, "Overture: An object-oriented framework for overlapping grid applications," in *AIAA conference on Applied Aerodynamics*, 2002.

[92] W. Y. Crutchfield and M. L. Welcome, "Object-Oriented Implementation of Adaptive Mesh Refinement Algorithms," *Scientific Programming*, vol. 2, no. 4, pp. 145–156, Dec. 1993.

[93] J. Bell, M. J. Berger, J. Saltzman, and M. Welcome, "Three-dimensional adaptive mesh refinement for hyperbolic conservation laws," *SIAM Journal on Scientific Computing*, vol. 15, no. 1, pp. 127–138, 1994.

[94] M. Griebel, "Parallel multigrid in an adaptive PDE solver based on hashing and space-filling curves," *Parallel Computing*, vol. 25, no. 7, pp. 827–843, 1999.

[95] R. J. Leveque, "CLAWPACK - a software for solving multidimensional conservation laws," in *Proceedings of the 5th International Conference on Hyperbolic Problems*, Stony Brook, NY, 1994.

[96] P. Woodward and P. Colella, "The numerical simulation of two-dimensional fluid flow with strong shocks," *Journal of Computational Physics*, vol. 54, pp. 115–173, Oct. 1984.

[97] P. Hwang, R. P. Fedkiw, B. Merriman, T. D. Aslam, A. R. Karagozian, and S. J. Osher, "Numerical resolution of pulsating detonation waves," *Combustion Theory and Modelling*, vol. 4, no. 3, pp. 217–240, 2000.

[98] G. J. Sharpe, "Linear stability of pathological detonations," *Journal of Fluid Mechanics*, vol. 401, pp. 311–338, Dec. 1999.

[99] G. J. Sharpe and M. I. Radulescu, "Statistical analysis of cellular detonation dynamics from numerical simulations: one-step chemistry," *Combustion Theory and Modelling*, vol. 15, no. 5, pp. 691–723, 2011.

[100] D. Barkley and R. D. Henderson, "Three-dimensional Floquet stability analysis of the wake of a circular cylinder," *Journal of Fluid Mechanics*, vol. 322, pp. 215–241, 1996.

[101] C. M. Romick, T. D. Aslam, and J. M. Powers, "Dynamics of Unsteady Inviscid and Viscous Detonations in Hydrogen-Air," in *AIAA 2012-0981*, 2012.

[102] H. S. Dou, H. M. Tsai, B. C. Khoo, and J. Qiu, "Simulations of detonation wave propagation in rectangular ducts using a three-dimensional WENO scheme," *Combustion and Flame*, vol. 154, no. 4, pp. 644–659, 2008.

[103] G. Iooss and M. Adelmeyer, *Topics in bifurcation theory and applications*. World Scientific Pub Co Inc, 1998, vol. 3.

[104] A. K. Henrick, T. D. Aslam, and J. M. Powers, "Simulations of pulsating one-dimensional detonations with true fifth order accuracy," *Journal of Computational Physics*, vol. 213, no. 1, pp. 311–329, 2006.

[105] E. Oran, J. W. Jr, and E. Stefaniw, "A numerical study of a two-dimensional H2-O2-Ar detonation using a detailed chemical reaction model," *Combustion and Flame*, vol. 2180, no. 97, 1998.

BIOGRAPHICAL STATEMENT

Prashaanth Ravindran was born in Chennai, South India in 1981. He received his B.E. degree in Aeronautical Engineering from University Of Madras, India, in 2002, his M.S. and Ph.D. degrees from The University of Texas at Arlington in 2005 and 2012, respectively, in Aerospace Engineering. His interest in Computational Fluid Dynamics stemmed from a short work stint at the Indian Institute of Science, Bangalore, India, where he worked on grid generation for complex geometries. His Master's thesis was on the topic of simulating detonations in parallel environments. His research interests are combustion, numerical modeling and programming.